STRONGLY CORRELATED PHASES IN THE ANISOTROPIC HONEYCOMB LATTICE

WANG GUANGQUAN

NATIONAL UNIVERSITY OF SINGAPORE

2012

STRONGLY CORRELATED PHASES IN THE ANISOTROPIC HONEYCOMB LATTICE

WANG GUANGQUAN
(B.Sc. (Hons.), NUS)

A THESIS SUBMITTED FOR

THE DEGREE OF DOCTOR OF PHILOSOPHY

CENTRE FOR QUANTUM TECHNOLOGIES
NATIONAL UNIVERSITY OF SINGAPORE

2012

Declaration

I hereby declare that this thesis is my original work and it has been written by me in its entirety. I have duly acknowledged all the sources of information which have been used in the thesis.

This thesis has also not been submitted for any degree in any university previously.

Wang Guangquan

March 12, 2013

Acknowledgements

I would like to thank my supervisors, Berthold-G. Englert, Benoît Grémaud, Christian Miniatura and Mark O. Goerbig, without whose supervision this work would not have existed. Thanks for all the opportunities that you have given me. All the help throughout these years are sincerely appreciated. I would like to acknowledge the financial and other forms of support from both Centre for Quantum Technologies and French Merlion PhD program (CNOUS 200960). My appreciation also goes to Laboratoire de Physique des Solides, for all the support in terms of resources during my stay there. I acknowledge useful discussions with Gilles Abramovici, Jean-Noel Fuchs, Marc Gabay, Raphaël de Gail, Lih-King Lim, Luca De Medici, Gilles Montambaux and Pascal Simon. I am grateful for the support from my girlfriend Yunfang and my parents during all these years. Thanks for being there for me.

Abstract

In this thesis I present my results concerning various phases and phase transitions in the honeycomb optical lattice with in-plane anisotropic hopping amplitudes. The anti-ferromagnetic transition is studied as the first step. Using the mean-field self-consistent method as well as a calculation based on Stoner's criterion, the transition line is found to consist of two approximately linear parts meeting at the point of the topological phase transition, which is triggered by the in-plane anisotropic hopping amplitudes. The linearity of the transition lines is explained using simple scaling arguments. The effective Hamiltonian that we derived for the limit of large anisotropy and strong correlation, which is the quantum Ising model on an effective square lattice, shows the microscopic detail of the phase space in the vicinity of the transition line in the proper limits. The second transition studied is that from the metallic state to the spin-liquid phase, which is indicated by the opening of a charge gap while the spin channel remains paramagnetic. Within the slave-rotor method, a gapped spin-liquid phase described by effectively decoupled dimers is found to be dominating in the limit of large anisotropy. The fate of the spin-liquid phase in the limit of isotropic doping, i.e. in the symmetric honeycomb lattice, however, is not clear in our calculation. Further investigation, with the help of theoretical techniques beyond the mean-field slave-rotor treatment, is needed to settle this issue. The effective Hamiltonian mentioned above for the anti-ferromagnetic transition in the limits of large anisotropy and strong correlation shows that the quantum state of this spin-liquid phase is that of spin singlets on decoupled dimers, which can be considered as a special case of the short-range RVB state.

By the same effective Hamiltonian, the transition between the antiferromagnetic and the spin-liquid phase is that of the quantum Ising model on the square lattice. We then turned to AA-stacked bilayer honeycomb lattice with attractive onsite interaction. The subject of study is the pairing transition, which is intimately related to the antiferromagnetic transition in the repulsive case. We first studied the system doped to the Dirac points, which are no longer situated at zero energy as in the case of monolayer honeycomb lattice, due to the inter-layer nearest-neighbor hopping. In the limit of large interlayer hopping, the critical interaction strength for the pairing transition is doubled as compared to the limit of decoupled layers, a result that can be explained in the dimer picture. We then studied two typical cases representing two situations before and after the topological phase transition. The correlation between the existence of a finite interaction strength and that of a finite-sized Fermi surface, and, in the case of a finite-sized Fermi surface, the correlation between the magnitude of the order parameter and the size of the Fermi surface are found.

Contents

List of Figures

LIST OF FIGURES

LIST OF FIGURES

1

Introduction

1.1 Graphene and Honeycomb Optical Lattice

1.1.1 Graphene

Graphene is the first experimentally-realized two-dimensional (2D) crystal. Ever since its isolation and electronic contacting in 2004 [1], tremendous amount of research interest in this material has been triggered, presumably by its potential to revolutionize the field of condensed matter research, the electronics industry and, ultimately, our daily life. The reasons for the interest can, of course, be traced down to the unusual properties of graphene [1–4], which will be briefly discussed in this chapter. The Nobel prize in physics in 2010 was awarded to Andre Geim and Konstantin Novoselov, who were responsible for the "groundbreaking experiments regarding the two-dimensional material graphene" [5].

However, graphene is not new to us. Graphite, a 3D material made out of sheets of graphene glued together by the van der Waals force, has been used by mankind as a tool for drawing and writing ever since the 4th millennium BC [6]. In the 1940s, graphite drew the attention of the physics community, because of its crucial role in nuclear power plants controlling the rate of chain reactions. As a preliminary study for graphite, graphene was then investigated in detail for the first time, albeit as a mere theoretical concept, presumably being unstable towards the formation of curved structures (such as fullerenes, carbon nanotubes, etc.).

Because of its atomic thickness, an isolated sheet of graphene was not experimentally accessible for electronic transport measurement until 2004 [1], when

the group in Manchester, led by Andre Geim and Konstantin Novoselov, successfully fabricated and observed, with the help of an optical microscope, sheets of graphene on specially prepared SiO_2 substrates. In subsequent experiments [2], the electronic properties of graphene were probed. It was found that graphene is an excellent metal, with virtually all charge carriers mobile. In more recent experiments on suspended graphene samples [7, 8], the mobility was found to be beyond $\sim$100,000 $cm^2V^{-1}s^{-1}$, which can be pushed further with the aid of a hexagonal Boron-Nitride substrate [9]. With the application of a gate voltage V_g, which tuned the carrier density, the observed behavior of graphene resembles the field effect in semi-conductors, the only difference being the absence of a band gap. This opened the potential application of graphene in micro-electronics as transistors [10], which are the basic elements of integrated electric circuits, though means of gap-opening are still needed. Estimations at IBM show that metallic transistors based on graphene could improve the miniaturization of electronic chips by one order of magnitude. Apart from its potential application as field effect transistors, for which its electronic properties are chiefly responsible, the mechanical properties and structural and chemical stability of graphene render it an exceptionally useful material in many other areas of application, ranging from quantum information storage device [11] to membrane sensors for detecting pressure changes in small volumes [12]. A summary of such applications can be found in the review by Abergel et al. [13]. The technological potential of graphene is one of the major motivations underlying the current intense research on this material.

The investigation of Shubnikov-de Haas oscillations and the discovery of the integer quantum Hall effect in graphene revealed characteristic behaviors of relativistic Dirac fermions in magnetic fields [2, 14]. This confirmed the theoretical predictions of a tight-binding band structure calculation published in 1946 [15], where Wallace showed that the energy dispersion of graphene features the conical intersections at the corners of the first Brillouin zone (FBZ) (the K and K′ points in Figure 1.1(b)). The effective band structure around these points is that of the 2D Dirac equation without a mass term, hence these points are termed Dirac points. The low energy electronic excitations in graphene are a realization of this model in relativistic quantum mechanics, which formerly was of interest

to high-energy physicists only. In the experiment, the effective speed of light (the Fermi velocity) is fitted to be

$$v_{\mathrm{F}} \approx \frac{c}{300}, \tag{1.1}$$

where c is the speed of light in vacuum. Dirac fermions were directly observed in graphene in 2006 using angle-resolved photo-emission spectroscopy [4]. Thus graphene serves as a bridge between condensed matter and relativistic physics [16]. Other unusual behaviors of the electrons in graphene that are characteristic of relativistic particles include the Klein paradox [17], which is the phenomenon of the absence of backscattering when transmitted through an external electrostatic potential, and the anomalous integer quantum Hall effect in a strong magnetic field [18–20]. The fundamental research interest in a 2D relativistic condensed matter system is another major motivation.

Because graphene sheets can be considered as the building blocks of a number of other carbon based materials, the study of graphene benefits the understanding of a class of these materials. Examples are fullerenes, which are zero-dimensional objects obtained from graphene by introducing pentagons into the lattice structure, carbon nanotubes, which are under intense research, can be obtained from graphene by rolling it in a particular direction and connecting the carbon bonds: these are quasi-1D objects, and in 3D, graphite, as already mentioned, is a stack of graphene glued together by the van der Waals force. Graphene is the natural starting point for the study of these materials.

On the technical level, graphene is a sheet of carbon atoms arranged in a stack of hexagons (see Figure 1.1(a)). The electronic configuration of an isolated carbon atom is $1s^2 2s^2 2p^2$. The electrons in the $1s$ orbital are deep in the inner shell, and are irrelevant when considering chemical bonding. The $2s$ orbital is lower in energy than the $2p$ orbitals, and is thus fully populated by two electrons in an isolated carbon atom. However, in the presence of other atoms, such as in graphene or in benzene, it turns out to be energetically favorable to promote one of the two electrons in the $2s$ orbital to the $2p$ orbitals, in order to form covalent bonds. The resulting sp^2 hybridization between an s-orbital and two p-orbitals (p_x and p_y) leads to the formation of a trigonal planar orbital structure, which is responsible for the formation of σ-bonds between carbon atoms as well as

the 2D structure of graphene. While these hybridized orbitals are inert from the electronic transport point of view, the remaining p_z orbital, which is perpendicular to the lattice plane, overlaps with neighboring sites to form a π-band, and is thus responsible for the electronic transport properties of graphene. Since there is one electron per carbon atom in the p_z-orbital, the low-lying π-bands in graphene are half-filled.

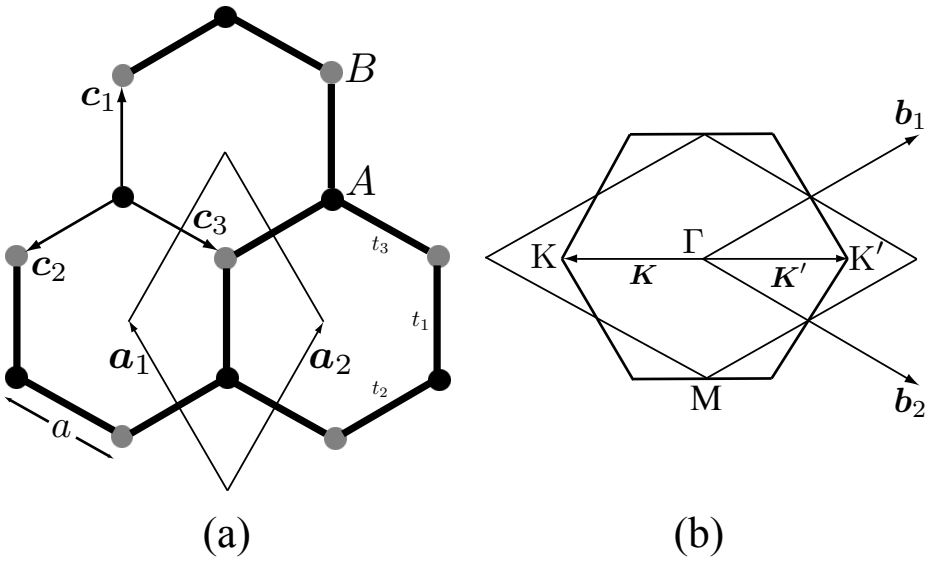

Figure 1.1: (a): The honeycomb lattice and its diamond-shaped unit cell delineated by the triangular Bravais lattice vectors $\boldsymbol{a}_1$ and $\boldsymbol{a}_2$. Black and gray sites belong to sub-lattices A and B, respectively. A nearest-neighbor-hopping event along directions $\boldsymbol{c}_{1,2,3}$ causes hopping amplitudes $t_{1,2,3}$, respectively. a is the lattice constant. (b): The reciprocal lattice of the honeycomb lattice is spanned by the primitive vectors $\boldsymbol{b}_{1,2}$. The first Brillouin Zone (FBZ) is also hexagon-shaped. The calculations in this thesis are performed in the diamond-shaped primitive unit cell, which is equivalent to the FBZ. Γ, M, K and K′ are points of symmetry that will be important to our discussion. The other four corners of the hexagonal FBZ are connected to either K or K′ by the elementary reciprocal lattice vectors $\boldsymbol{b}_1$, $\boldsymbol{b}_2$ or their combinations. There are three inequivalent centers of the sides of the hexagonal FBZ, one of them (the M point) being illustrated in the figure. The vectors $\boldsymbol{K}$ and $\boldsymbol{K}'$ point from the Γ point to the K and K′ points, respectively.

1.1.2 Honeycomb Optical Lattice

The physical properties of graphene are in large attributable to the underlying lattice structure, namely the honeycomb lattice, which hosts a bunch of rich phenomena [13, 35]. For example, in its naturally occurring form, graphene is a semi-metal. By changing the lattice geometry, relative energy scales or filling, many other interesting phases are attainable, examples being band-insulating and antiferromagnetic phases [21, 22] .

However, physical limitations render graphene not a very suitable system for the study of the full phase space of the honeycomb lattice. For example, deformation through the application of uniaxial strain [21, 23] changes the spatial separation between neighboring sites in graphene, hence changes the corresponding electronic wave function overlap, upon which the electron hopping amplitudes depend. In the honeycomb lattice, sufficient anisotropy in hopping amplitudes leads to the opening of a band gap [24–26]. However, the amount of anisotropy required to achieve this band-gap-opening is likely to be beyond the sustainable limit of a graphene sheet [21, 23, 24, 27].

A system much better suited for the manipulation of the hopping amplitudes, and thus for the study of the full phase space, is the system of an optical lattice loaded with ultra-cold atoms [28–30]. As a simulation of condensed matter systems, the optical lattice plays the role of the atomic potential, while the ultra-cold atoms play the role of the electrons.

Optical lattices in general are formed using a set of counter propagating laser beams, which interfere with each other and form a spatially periodic optical potential. A variety of lattice structures can be generated by different configurations of laser beams [31]. Because of its optical nature, this system is free from impurities, defects and effects such as electron-phonon interaction, which can destroy quantum coherence in condensed matter systems. Thus this system allows us to concentrate on the intrinsic properties of the lattice structure. Moreover, the lattice parameters can be varied by varying the laser as well as geometric parameters [24–26, 31–34]. Thus over naturally occurring crystal systems, the optical lattice system has major advantages in configurability and controllability [31]. When loaded with ultra-cold atoms, this system offers possibilities of simulating

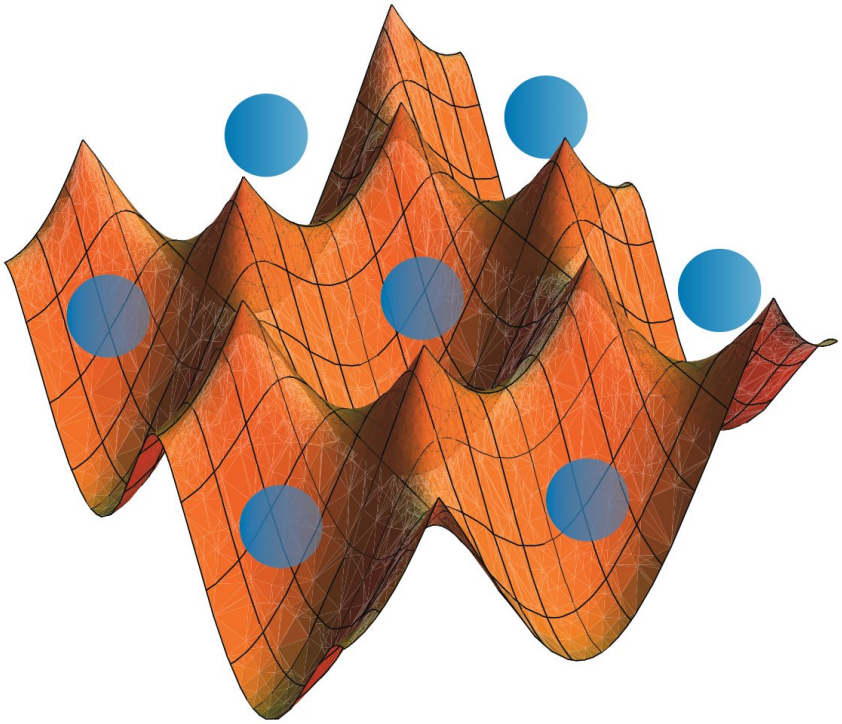

Figure 1.2: An illustration of the optical lattice system (orange potential) loaded with ultra-cold atoms (blue spheres). This particular example is a triangular lattice, formed by the setup as shown in Figure 1.3(a), but with a red-detuned laser system. See the caption of Figure 1.3 for detail.

situations difficult to achieve in condensed matter systems [32, 33, 44]. This has been made possible by the recent experimental advances in the cooling and manipulation of atoms [30,36,37], landmarked by the realization of the Bose-Einstein condensation [29, 38–40] as well as Fermi degeneracy [41–43], and more recently by the study of pairing and superfluidity in fermions [45–47] as well as the studies on the imbalanced fermionic mixtures [48–52]. An additional advantage of this system over conventional condensed matter systems is the possibility of engineering the sign and strength of the particle-particle interactions using Feshbach resonance [53, 54].

The mechanism by which the atoms are trapped in the optical potential is provided by the interaction between the dipole moment of the ultra-cold atoms and the optical potential. The frequencies of the laser beams are detuned in order to avoid spontaneous emission that can destroy the coherence of the system.

For blue- and red-detuned laser beams, the minima of the potential energy of the atoms coincide with the minima and maxima of the dipole potential, respectively. Figure 1.2 illustrates a simple two-dimensional triangular optical lattice system loaded with ultra-cold atoms, which can be formed by three counter-propagating red-detuned laser configuration as schematically sketched in Figure 1.3(a). The honeycomb optical lattice, on the other hand, is obtained with the same geometrically configured, but blue-detuned system [31, 55], the optical potential landscape of which is shown in Figure 1.3(b). Another equivalent setup is obtained by changing the three $\frac{2\pi}{3}$-angles in Figure 1.3(a) to $(\frac{\pi}{3}, \frac{\pi}{3}, \frac{4\pi}{3})$ [31]. Yet another way of constructing the honeycomb lattice, among many other possible lattice structures, is provided in Reference [32]. Successes in loading ultra-cold atoms in the honeycomb optical lattice have been reported in References [32, 55].

In contrast to the electrons in condensed matter systems, cold atoms are neutral. The interaction among them is mainly in the form of s-wave scattering. This is an advantage of the optical lattice when it comes to simulating the Hubbard onsite interaction, which will be introduced in a later section. On the other hand, because of the neutrality of atoms, electric and magnetic fields do not act on them the way they do on electrons, which poses difficulties on experimental efforts on gauge-field-related effects in the optical lattice system, a prominent example being the quantum Hall effect. There have been various proposals for simulating such effects, a recent example being the use of laser assisted tunneling to create an effective gauge potential [56–60]. A recent review on this subject is found in Reference [61].

In this thesis, we always have the optical lattice system in mind, unless otherwise specified.

1.1.3 Crystallographic specifications and the continuum limit

For later convenience, in this section we specify the honeycomb lattice structure. As shown in Figure 1.1(a), it is a bipartite lattice, made out of two interpenetrating triangular sub-lattices, which are labeled A (black dots) and B (gray

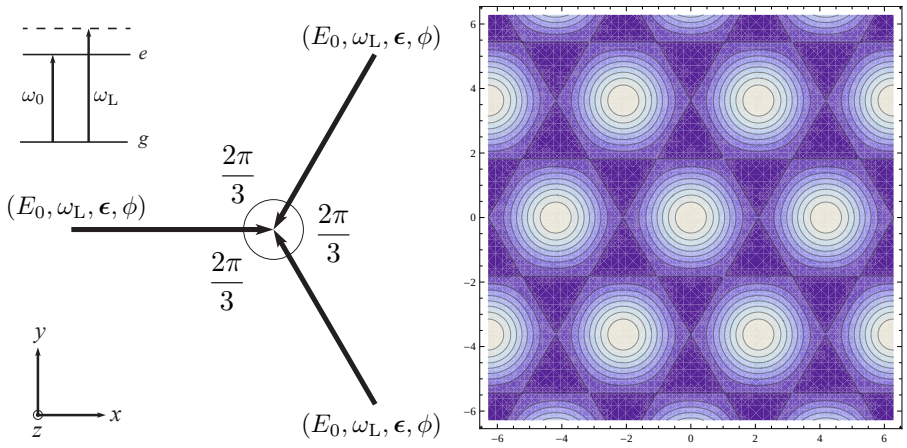

(a) (b)

Figure 1.3: (a): The arrangement of laser beams in order to make a honeycomb optical lattice. $(E_0, \omega_L, \boldsymbol{\epsilon}, \phi)$ are, respectively, the electric field amplitude, the angular frequency, the polarization and the phase of the laser beams. These parameters are the same for all the laser beams in this configuration. A schematic illustration of the atomic energy levels and the laser frequency is shown the inset in the up-left corner, where g and e are the ground ant excited atomic states, while ω_0 and ω_L are the atomic excitation and laser frequencies, respectively. The lasers are blue-detuned in this case, because $\omega_L > \omega_0$. (b): The corresponding potential landscape formed by the laser beams in (a) is shown here. Dark and white areas are potential valleys and heights, respectively. Due to the blue-detuning of the laser beams, atoms are to be attracted to the valleys of the potential landscape, which collectively form a honeycomb lattice. For red-detuned laser configuration, i.e. $\omega_L < \omega_0$, this system is to be regarded as a triangular lattice, which is illustrated in Figure 1.2. See Reference [31] for more detail.

dots). The Bravais lattice vectors of the triangular lattice are

$$\boldsymbol{a}_{1,2} = \sqrt{3}a\left(\mp\frac{1}{2}, \frac{\sqrt{3}}{2}\right). \tag{1.2}$$

The lattice constant of graphene is $a = 1.42$Å. Each lattice site in sublattice-A has three nearest neighbors (nn) in sublattice-B, connected by the vectors

$$\boldsymbol{c}_1 = a(0,1),\ \boldsymbol{c}_{2,3} = a\left(\mp\frac{\sqrt{3}}{2}, -\frac{1}{2}\right). \tag{1.3}$$

The hopping amplitudes along these directions are respectively $t_{1,2,3}$, as shown in Figure 1.1(a).

The primitive vectors of the reciprocal lattice, as shown in Figure 1.1(b), are

$$\boldsymbol{b}_{1,2} = \frac{2\pi}{\sqrt{3}a}\left(1, \pm\frac{1}{\sqrt{3}}\right). \tag{1.4}$$

The crystal momentum can be expressed as

$$\boldsymbol{k}_{n,m} = \frac{n}{N}\boldsymbol{b}_1 + \frac{m}{M}\boldsymbol{b}_2 = \frac{2\pi}{\sqrt{3}a}\left(\left(\frac{n}{N} + \frac{m}{M}\right), \frac{1}{\sqrt{3}}\left(\frac{n}{N} - \frac{m}{M}\right)\right), \tag{1.5}$$

where $N \times M = N_\mathrm{c}$ equals the number of unit cell in the system and, assuming even N and M,

$$\begin{aligned} n &\in \left\{-\frac{N}{2}, \cdots, \frac{N}{2} - 1\right\}, \\ m &\in \left\{-\frac{M}{2}, \cdots, \frac{M}{2} - 1\right\}. \end{aligned} \tag{1.6}$$

The $\boldsymbol{K}$ and $\boldsymbol{K}'$ vectors, which point from the origin to the Dirac points, are given

by

$$\boldsymbol{K} = \frac{4\pi}{3\sqrt{3}a}(-1,0),\ \boldsymbol{K'} = \frac{4\pi}{3\sqrt{3}a}(1,0). \tag{1.7}$$

The area of a single $\boldsymbol{k}$-state in the reciprocal space is given by that of the small parallelogram formed by $\boldsymbol{b}_1/N$ and $\boldsymbol{b}_2/M$, which is

$$|\delta^2\boldsymbol{k}| = \frac{1}{N_\mathrm{c}}\frac{8\pi^2}{3\sqrt{3}a^2}. \tag{1.8}$$

In this thesis we consider the theoretical limit of an infinite size crystal. With this in mind, we take $N \to \infty,\ M \to \infty$, so that the crystal momentum $\boldsymbol{k}$ in Equation (1.5) becomes continuous:

$$\begin{aligned} -\frac{2\pi}{\sqrt{3}a} < k_x \leq \frac{2\pi}{\sqrt{3}a}, \\ -\frac{2\pi}{3a} + \frac{|k_x|}{\sqrt{3}} < k_y \leq \frac{2\pi}{3a} - \frac{|k_x|}{\sqrt{3}}, \end{aligned} \tag{1.9}$$

corresponding to the diamond shaped unit cell in the reciprocal space, as shown in Figure 1.1(b). Using the unit area in the reciprocal space, namely Equation (1.8), the summation of the discrete crystal momentum over the First Brillouin Zone (FBZ), which we frequently need to perform, in the continuum limit can be approximated as

$$\frac{1}{N_\mathrm{c}}\sum_{\boldsymbol{k}} \cdots = \frac{3\sqrt{3}a^2}{8\pi^2}\sum_{\boldsymbol{k}} \delta^2\boldsymbol{k} \cdots \approx \frac{3\sqrt{3}a^2}{8\pi^2}\int d^2\boldsymbol{k} \cdots . \tag{1.10}$$

The integration limits are the inequalities (1.9). To further simplify the formality, we make the rescaling

$$\frac{\sqrt{3}ak_x}{2} \to x,\ \frac{3ak_y}{2} \to y, \tag{1.11}$$

so that

$$\frac{1}{N_{\mathrm{c}}}\sum_{\boldsymbol{k}}\cdots\approx\frac{1}{2\pi^2}\int dxdy\cdots. \tag{1.12}$$

Correspondingly, the integration limits become

$$-\pi<x<\pi,\ -\pi+|x|<y<\pi-|x|. \tag{1.13}$$

1.2 Dirac Fermions and the topological phase transition

1.2.1 Tight-binding band structure and Dirac fermions

The physical properties of the honeycomb lattice are well captured by the kinetic tight-binding model

$$\mathcal{H}_0=-\sum_{\langle ij\rangle\sigma}t_{ij}a^{\dagger}_{i\sigma}b_{j\sigma}+\mathrm{H.c.}-\mu\sum_{i\alpha\sigma}n^{\alpha}_{i\sigma}. \tag{1.14}$$

Here $a^{\dagger}_{i\sigma}$ ($b_{j\sigma}$) creates (annihilates) an electron with spin $\sigma=\uparrow,\downarrow$ on lattice site $i\in A$ ($j\in B$); $\langle ij\rangle$ are the nearest-neighboring sites; t_{ij} is the hopping amplitude between nearest-neighboring sites i and j; μ is the chemical potential determining the total number of particles, with half-filling corresponding to $\mu=0$ due to the particle-hole symmetry.

The Hamiltonian can be diagonalized in momentum space with the help of the Fourier transform

$$\alpha_{i\sigma}=\frac{1}{\sqrt{N_{\mathrm{c}}}}\sum_{\boldsymbol{k}}\exp\left(i\boldsymbol{k}\cdot\boldsymbol{R}_i\right)\alpha_{\boldsymbol{k}\sigma}, \tag{1.15}$$

where $\alpha=a,b$ denotes the annihilation operators, the vectors $\boldsymbol{R}_i$ form a triangu-

lar Bravais lattice, and N_c is the number of unit cells. In momentum space, the kinetic Hamiltonian becomes

$$\mathcal{H}_0 = -\sum_{\boldsymbol{k}} (a_{\boldsymbol{k}}^\dagger \; b_{\boldsymbol{k}}^\dagger) \begin{pmatrix} 0 & \gamma^{\boldsymbol{k}} \\ \gamma^{\boldsymbol{k}*} & 0 \end{pmatrix} \begin{pmatrix} a_{\boldsymbol{k}} \\ b_{\boldsymbol{k}} \end{pmatrix}, \text{with } \gamma^{\boldsymbol{k}} = \sum_j t_j e^{i\boldsymbol{c}_j \cdot \boldsymbol{k}}, \tag{1.16}$$

from which we obtain the tight-binding energy bands

$$\epsilon^{\boldsymbol{k}}_{\lambda=\pm} = \lambda |\gamma^{\boldsymbol{k}}| \tag{1.17}$$

and the corresponding eigenstates

$$\phi^{\boldsymbol{k}}_{\lambda=\pm} = \frac{1}{\sqrt{2}} \begin{pmatrix} 1 \\ \lambda e^{-i\theta^{\boldsymbol{k}}_\gamma} \end{pmatrix}, \text{ with } e^{i\theta^{\boldsymbol{k}}_\gamma} = \frac{\gamma^{\boldsymbol{k}}}{|\gamma^{\boldsymbol{k}}|}. \tag{1.18}$$

Natural graphene has $t_1 = t_2 = t_3 \equiv t$ due to its point symmetry that includes invariance under 120° rotation, so that we have in this case

$$|\gamma^{\boldsymbol{k}}| = t\sqrt{1 + 4\cos^2 x + 4\cos x \cos y}. \tag{1.19}$$

The corresponding band structure is plotted in Figure 1.4. The points at which the two bands touch are solutions of the equation

$$|\gamma^{\boldsymbol{k}}| = 0, \tag{1.20}$$

which yields the vectors (1.7). These so-called Dirac points are labeled K and K′ in Figure 1.1(b). When the structure factor $\gamma^{\boldsymbol{k}}$ is expanded around these points to leading order in $\boldsymbol{q} = \boldsymbol{k} - \boldsymbol{K}$ and $\boldsymbol{q}' = \boldsymbol{k} - \boldsymbol{K}'$, where $\boldsymbol{k}$ is the crystal momentum,

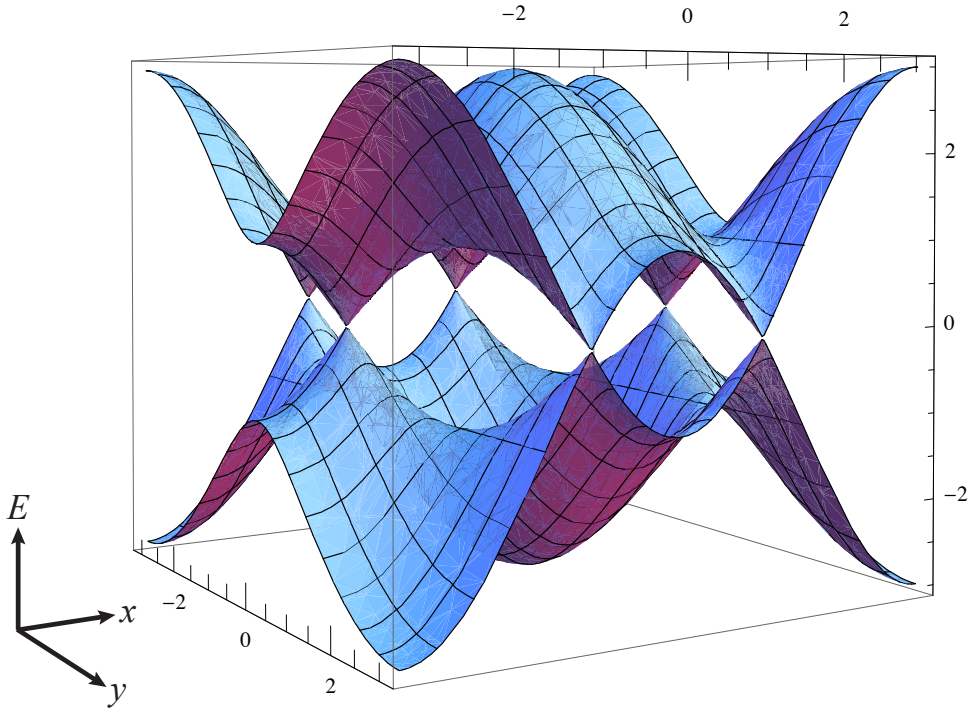

Figure 1.4: The tight-binding band structure of the honeycomb lattice (1.17). Notice that this figure is plotted in the rescaled coordinates (1.11), namely $x = \frac{\sqrt{3}ak_x}{2}$ and $y = \frac{3ak_y}{2}$.

one obtains

$$\gamma^{\boldsymbol{K}+\boldsymbol{q}} \approx v_{\mathrm{F}}(q_x + iq_y), \tag{1.21a}$$

$$\gamma^{\boldsymbol{K}'+\boldsymbol{q}'} \approx -v_{\mathrm{F}}(q'_x - iq'_y), \tag{1.21b}$$

with

$$v_{\mathrm{F}} = 3at/2 \tag{1.22}$$

being the Fermi velocity in Equation (1.1). Notice that in graphene we have

$$t \simeq 3\mathrm{eV}, \tag{1.23}$$

which implied the value of the effective speed of light in Equation (1.1), and that we have taken $\hbar$ to be unity here, which convention will be followed in this thesis. We thus have the effective Hamiltonians

$$\mathcal{H}_{\mathrm{K}}(\boldsymbol{q}) = -v_{\mathrm{F}}(q_x\sigma_x - q_y\sigma_y), \tag{1.24a}$$

$$\mathcal{H}_{\mathrm{K}'}(\boldsymbol{q}') = v_{\mathrm{F}}(q'_x\sigma_x + q'_y\sigma_y), \tag{1.24b}$$

both of which resemble the 2D massless Dirac Hamiltonian, hence the name Dirac points for the band-contact points. The dispersion relation of the two Hamiltonians is given by

$$E^{\lambda=\pm}_{\mathrm{K},\mathrm{K}'}(\boldsymbol{q}) = \lambda v_{\mathrm{F}} q \tag{1.25}$$

with $q = |\boldsymbol{q}|$, independent of the subscripts K and K$'$. In the low energy limit of $E \ll t$, one is therefore confronted with a two-fold valley degeneracy, in addition to the original spin degeneracy.

1.2.2 Anisotropic honeycomb lattice and the topological phase transition

As implied by Equation (1.20), the locations of Dirac points are functions of real space geometry as well as hopping amplitudes. Naturally occurring graphene has perfect honeycomb lattice with isotropic nearest-neighbor hopping amplitudes, implying highly symmetric locations of Dirac points at K and K′. Relocation of the Dirac points can be achieved by, for example, changing the relative strength of the nearest-neighbor hopping amplitudes [25, 26, 34]. The resulting locations are $\boldsymbol{k} = \pm\boldsymbol{k}_{\mathrm{D}}$, where [26]

$$\boldsymbol{k}_{\mathrm{D}} = \begin{pmatrix} \frac{2}{a}\arccos\left(-\sqrt{\frac{t_1^2-(t_2-t_3)^2}{4t_2t_3}}\right) \\ \frac{2}{a\sqrt{3}}\mathrm{sgn}(t_3-t_2)\arccos\left(\frac{t_2+t_3}{t_1}\sqrt{\frac{t_1^2-(t_2-t_3)^2}{4t_2t_3}}\right) \end{pmatrix}, \tag{1.26}$$

where $\mathrm{sgn}(x)=x/|x|$. The above expression implies that the hopping amplitudes must satisfy the triangle inequality

$$|t_2 - t_3| < t_1 < t_2 + t_3 \tag{1.27}$$

in order for Dirac points to exist [25]. The region in parameter space in which the above inequality is satisfied is illustrated in Figure 1.5.

In the case where $t_1 > t_2 + t_3$, as illustrated in Figure 1.6, the Dirac points merge, and a band gap opens: instead of a semi-metal, the system becomes a band-insulator, in which phase the band gap is given by

$$\Delta_{\mathrm{BI}} = |t_1 - t_2 - t_3|\,. \tag{1.28}$$

This phase transition is an example of a topological Lifshitz transition, which is essentially a transformation of the topological property of the band structure. In particular, before the transition, the two inequivalent Dirac points have Berry phases π and $-\pi$, respectively, while after the merging, the band has a combined

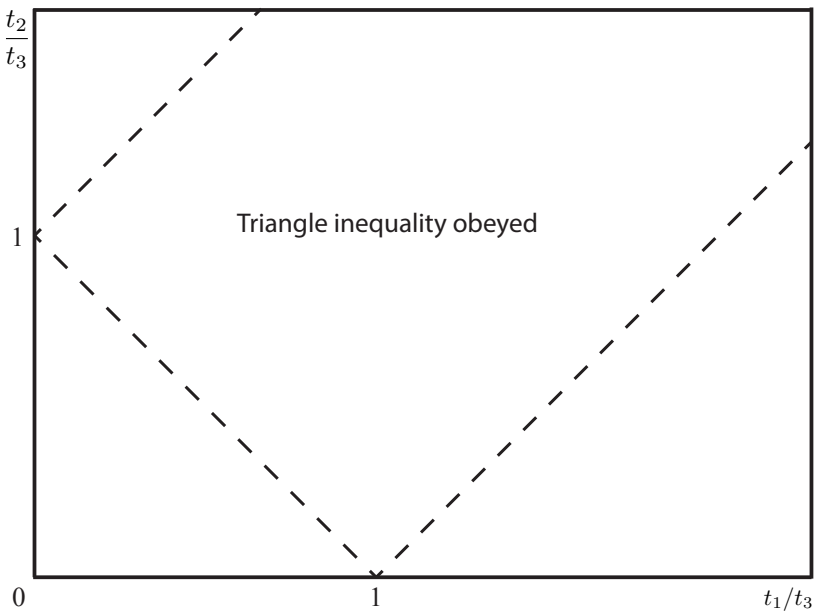

Figure 1.5: The triangle inequality is satisfied by the set of values of t_1, t_2 as measured in units of t_3 within the tilted dashed rectangle with corners at $(1, 0)$ and $(0, 1)$, which extends infinitely in the right-upward direction, and is not satisfied elsewhere.

Berry phase of 0 [24]. The experimental realization of the merging of the Dirac points in the honeycomb optical lattice has been reported in Reference [32].

In the particular case where, while the hopping amplitudes along $\boldsymbol{c}_2$ and $\boldsymbol{c}_3$ (t_2 and t_3 in Figure 1.1) are equal, the hopping along $\boldsymbol{c}_1$ can be different, we denote the hopping amplitudes as

$$t_1 \equiv t', \; t_2 = t_3 \equiv t. \tag{1.29}$$

In this case we have

$$|\gamma_{t'}^{\boldsymbol{k}}| = \sqrt{t'^2 + 4t^2 \cos^2 x + 4tt' \cos x \cos y}. \tag{1.30}$$

The resulting movement of Dirac points is illustrated in Figure 1.6. The merging

of Dirac points, according to the triangular inequality (1.27), takes place at

$$t' = 2t, \tag{1.31}$$

and the band gap for $t' > 2t$ is given by

$$\Delta_{\mathrm{BI}} = t' - 2t, \tag{1.32}$$

where we have used Equation (1.28). This is the simplest scenario in which the topological phase transition can take place, and is the case studied in this thesis.

1.3 Electron-electron interaction

In the following, we will briefly compare the nature of interactions in graphene to those in the optical honeycomb lattice system. In discussing the latter, which is the main subject of this thesis, we will also summarize the main findings reported in this thesis.

1.3.1 Coulomb interaction in graphene

While the model of free massless Dirac fermions accounts for the semi-metallic and band-insulating behavior of graphene very well, the electron-electron Coulomb interaction plays a subtle role [20]. The characteristic Coulomb interaction energy is given by

$$E_{\mathrm{int}} = \frac{e^2}{\epsilon l}, \tag{1.33}$$

where e is the electronic charge, l is the characteristic distance between charges, and ϵ is the dielectric constant of the environment. One may use the ratio between the Coulomb interaction energy and the kinetic energy $E_{\mathrm{kin}}(k_{\mathrm{F}})$ at the same length scale, i.e. $k_{\mathrm{F}} \sim l^{-1}$, to quantify the importance of the interaction effects. If this ratio is much larger than 1, the electron-electron correlation is important, in

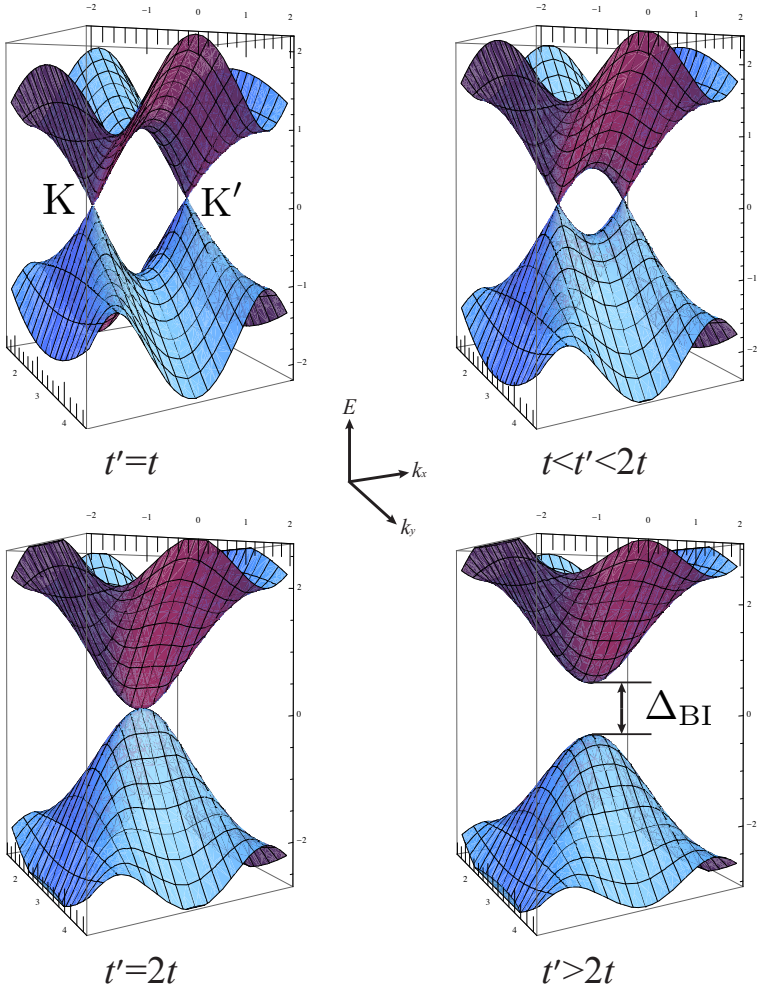

Figure 1.6: The band structure of the honeycomb lattice as a function of the hopping amplitudes: One of the three nearest-neighbor hopping amplitudes is labeled t', which is varied with respect to the other two (labeled t). At $t' = t$, the Dirac points are at points K and K′; for $t < t' < 2t$, the Dirac points shift toward each other, at $t' = 2t$ they coincide, forming the so called semi-Dirac point, at which the dispersion is linear in one direction and parabolic in the other; beyond this point, i.e. when $t' > 2t$, the Dirac points disappear and a band gap (Δ_{BI}) opens.

which case the quantum state of the system cannot be correctly described by one-particle models such as the Hamiltonian (1.14). In the case of graphene, one obtains

$$\alpha_G = \frac{E_{\text{int}}}{E_{\text{kin}}} = \frac{e^2}{\epsilon v_{\text{F}}} = \alpha_{\text{QED}} \frac{c}{v_{\text{F}}} \frac{1}{\epsilon} \simeq \frac{2.2}{\epsilon}, \tag{1.34}$$

where

$$\alpha_{\text{QED}} = \frac{e^2}{c} \approx \frac{1}{137} \tag{1.35}$$

is the fine structure constant in quantum electrodynamics, $c \approx 300 v_{\text{F}}$ is the vacuum speed of light. Equation (1.34) indicates that the interaction effects in graphene are in the intermediate region, and could be decreased further if embedded in an environment with a large ϵ.

The simple two-body Coulomb interaction potential (1.33) is long-range. However, in a many-body system on the macroscopic scale, the screening properties of the interacting electrons become important. An important quantity in this consideration is the characteristic screening length, which is the length beyond which the Coulomb interaction is irrelevant due to screening. It is given by

$$\lambda_{\text{TF}} \sim \frac{1}{k_{\text{TF}}} \tag{1.36}$$

within the Thomas-Fermi treatment, with

$$k_{\text{TF}} \simeq \alpha_G k_{\text{F}} \tag{1.37}$$

being the Thomas-Fermi wave vector in the two spatial dimensions [1], in terms of the graphene fine structure constant α_G discussed previously and the Fermi wave vector k_{F}. In undoped graphene, the Fermi wave vector is zero at the Dirac points. Thus the screening length (1.36) diverges, implying an essentially unscreened Coulomb interaction.

Experiments so far have shown that the physics of graphene is well captured by the one-particle tight-binding model (1.14), while the interaction effects remain

[1] In a three-dimensional space, this relation would be $k_{\text{TF}}^2 \simeq \alpha_G k_{\text{F}}^2$

subordinate. The above discussed interaction strength as indicated by α_G is one possible reason for this. Another possible reason would be the density of states of the honeycomb lattice at half-filling, given by [35]

$$\rho(E) = \frac{3\sqrt{3}a^2}{\pi}\frac{|E|}{v_{\mathrm{F}}^2}, \tag{1.38}$$

which linearly vanishes with $|E|$. This suppresses the interaction effects at the Dirac points further. Thus in order to study the possible effects of interaction, it is necessary to consider the optical version of the honeycomb lattice, which offers the tunability of the interaction strength, a feature that is largely absent in graphene.

There are however some indications for weak Coulomb interactions, such as the renormalization of the Fermi velocity [62] or quasi-particle features in photoemission spectra [63]. These effects are thoroughly discussed in a recent review [64], to which we refer the interested readers.

1.3.2 Interaction in the honeycomb optical lattice

The above considerations make it clear that in graphene, the Coulomb interaction is weak to intermediate in strength, and is long-range. However, the story is completely different in the case of the optical honeycomb lattice loaded with ultracold atoms, which, first of all, offers the possibility of engineering the interaction strength with the Feshbach resonance. Furthermore, as already mentioned before, the interaction between the neutral atoms mainly takes the form of two-body s-wave scattering. It is then natural to write down the Hubbard onsite interaction term

$$\mathcal{V} = U\sum_{i\alpha}(n_{i\uparrow}^{\alpha} - \frac{1}{2})(n_{i\downarrow}^{\alpha} - \frac{1}{2}), \tag{1.39}$$

where U is the interaction strength, and $n_{i\sigma}^{\alpha} = \alpha_{i\sigma}^{\dagger}\alpha_{i\sigma}$, where α are the sub-lattice indices as well as the corresponding annihilation operators, is the number operator for lattice site i in sublattice α and spin-σ. Notice that the spin here is in fact the

"pseudo-spin" associated with two hyperfine levels of the fermionic atoms that we consider in this thesis. This interaction term combines the extremely short interaction range of the s-wave scattering and the tight-binding picture of the kinetic Hamiltonian (1.14). This is the interaction term that will be considered in this thesis.

1.3.3 Promoting the interaction effects

As discussed previously in Section (1.3.1), the interaction effects are not vital to the description of graphene. The possible reasons include the weakness of the interaction strength and the vanishing density of states at half-filling. In order to study the possible consequences of the interaction, one must then promote the interaction effects, which can be achieved by either increasing the interaction strength, or by changing the density of states at the Fermi level.

1.3.3.1 Increasing the interaction strength

We in this thesis mainly consider the increase of the interaction strength as the means to promote the interaction effects. Two transitions are expected as the interaction strength is increased: the metal-Mott-insulator and the antiferromagnetic transitions.

The metal-Mott-insulator transition The metal-Mott-insulator transition takes place at the point where the interaction is just strong enough to freeze particles onto lattice sites. In this case spin order is not present if the charge (particle number) fluctuation is strong, and all lattice symmetries (spatial, rotational, parity and time reversal) will be preserved. This Mott insulator without spin order is termed a symmetric spin-liquid phase [65].

Because of the lack of geometric frustration in the honeycomb lattice, there have been debates about whether the spin-liquid is a feasible phase in this particular lattice structure [22, 66–68]. Nevertheless, theoretical studies such as References [69–71] have been performed, suggesting that, while geometric frustration

is absent, the strong charge fluctuation in the honeycomb lattice can still destroy the spin-ordering in the Mott phase. As there is no symmetry breaking in this transition, the conventional mean-field self-consistent method, which is derived from Landau's theory of order and phase transition, cannot be used for theoretical studies on the mean-field level. Thus a more sophisticated mean-field slave particle method is necessary. The slave rotor method [69, 70, 72] was used in References [69–71], yielding a critical interaction strength of $U_c = 1.68t$ for the metal-Mott-insulator transition in the honeycomb lattice with isotropic hoppings. This is the method employed in our calculation in this thesis.

The existence of the spin-liquid phase in the honeycomb lattice is confirmed in a recent large scale quantum Monte Carlo simulation [73]. Performing numerical simulations on a scale up to 648 sites with periodic boundary conditions, they found a region of spin-liquid in the phase diagram, lying in-between the semi-metallic and antiferromagnetic phases. Their results indicate that the critical interaction strength for this transition is $U_c/t \approx 3.5$, which is larger than the slave-rotor mean-field result. The main reason for the larger critical U in the former case is presumably quantum fluctuations, which are taken into account in the quantum Monte Carlo simulation, while being largely ignored in the mean-field treatment. The case is not closed yet, however, because a more recent quantum Monte Carlo simulation casts doubts on the stability of a gapped spin-liquid phase. The simulation in Reference [68] is performed on a scale of up to 2592 sites, much larger than the lattice size used in Reference [73]. Their results suggest that in the thermodynamic limit, the spin-liquid phase found in Reference [73] vanishes, and the usual antiferromagnetic long range order takes its stead.

Although decisive experimental evidence is still pending, in this thesis we assume the applicability of the slave-rotor method to the honeycomb lattice, and use it to investigate possible spin-liquid phases in the honeycomb lattice, as well as the evolution of this phase caused by the anisotropy of the hopping amplitudes. Within the mean-field slave-rotor treatment, we found a region of spin-liquid in between the metallic and antiferromagnetic phases. This spin-liquid phase becomes dominant in the limit of large anisotropy, i.e. the limit in which the bonds in one direction are much stronger than those in other directions. According to the

effective Hamiltonian that we derived for this particular limit, the microscopic state of the system can be shown to be that of singlet states on the stronger bonds (dimers), which is an example of the short range resonating valence-bonds state [74–76]. This state is perturbed by weak inter-dimer hopping events. On the other hand, in the isotropic limit, i.e. the symmetric honeycomb lattice, because of the singling-out of bonds in a particular direction in our treatment, our calculation is not adequate enough to settle the fate of the spin-liquid phase, for which further investigation is needed, which is out of scope of the current thesis. Furthermore, in the limit in which the bonds in a particular direction are much weaker than those in other directions, the system is composed of weakly coupled zig-zag chains. The physical properties of the system in this limit are dominated by the 1D structure of the chains. This is not discussed in the current thesis either. The detail of the slave-rotor calculation is presented in Chapter 4, and the derivation of the effective Hamiltonian is presented in Section 3.3.

The antiferromagnetic transition The second transition is the antiferromagnetic transition, which is generally expected to take place at a larger interaction strength than the previous transition. At this point, charge fluctuations are sufficiently suppressed, and spins are antiferromagnetically ordered due to virtual super-exchange interaction in the form $\frac{4t^2}{U}$. In the symmetric honeycomb lattice, this transition takes place at $U/t \approx 2.23$ in a mean-field calculation, while at $U/t \approx 4.5$ in the framework of the quantum Monte Carlo method [22].

Notice that in a system such as the square lattice at half-filling, due to the finite size of the Fermi surface, the antiferromagnetic order exists at any nonzero interaction strength, so that the antiferromagnetic transition coincides with the previously-discussed metal-insulator-transition at infinitesimal U. This is not the case in the honeycomb lattice at half-filling, however, since in this case the Fermi surface is composed of two points, in which case finite critical U can be calculated on the mean-field level. The honeycomb lattice structure also has the smallest coordination number in two-dimension and the above-mentioned vanishing density of states at the Fermi level, thus allowing for the strongest quantum fluctuations, while, because of its bipartite-ness, antiferromagnetism is imminent

at sufficiently strong interactions due to the lack of geometric frustration. Thus the competition between quantum fluctuations and repulsive interaction makes the honeycomb lattice an interesting theme of study.

In this thesis, we use the mean-field self-consistent method as well as Stoner's criterion to calculate the antiferromagnetic transition line. The results of the two methods turned out to be exactly the same, and is presented in Figure (3.1). This transition line is composed of two parts, which meet at the point of the topological phase transition with $t' = 2t$. Each part can be approximated by a linear function, which can be explained using simple scaling arguments as presented in Section (3.1.3).

In order to better understand the microscopic nature of the system in the large-U limit, we then derive effective Hamiltonians for the $U \to \infty$ limit. The derivation is performed in the spirit of the t-J model, and resulted in super-exchange interaction $\frac{4t^2}{U}$ as the characteristic energy scale. The effective Hamiltonian favors the anti-alignment of the spins. Re-writing the effective Hamiltonian by treating the dimers as entities, which is the correct picture in the limit of large-t', we obtain the quantum Ising model on an effective square lattice, from which we see that the two super-exchange interactions $\frac{4t^2}{U}$ and $\frac{4t'^2}{U}$ favor the Néel ordered states and the singlet state, respectively. The former state corresponds to the antiferromagnetic phase, while the latter state can be identified with the spin-liquid phase as previously discussed. The transition between these two phases, according to this effective model, is second order in nature, agreeing with our previous mean-field calculation of the same transition line.

1.3.3.2 Other means of promoting the interaction effects

Another way of promoting the interaction effects is, according to the discussion at the beginning of this section, to change the density of states at the Fermi level. This can be achieved via either stacking or doping. For example, in bilayer honeycomb lattice under AB-stacking at half-filling, the additional hopping between the inter-layer nearest neighbor changes the band structure at the Fermi surface, from Dirac-like linear to parabolic, and the density of states from vanishing to

constant [35]. These are studied usually in the interest of phenomena such as superconductivity, which is out of the scope of this thesis.

1.4 Motivations

The transitions that have been mentioned so far are sketched in Figure 1.7. In the

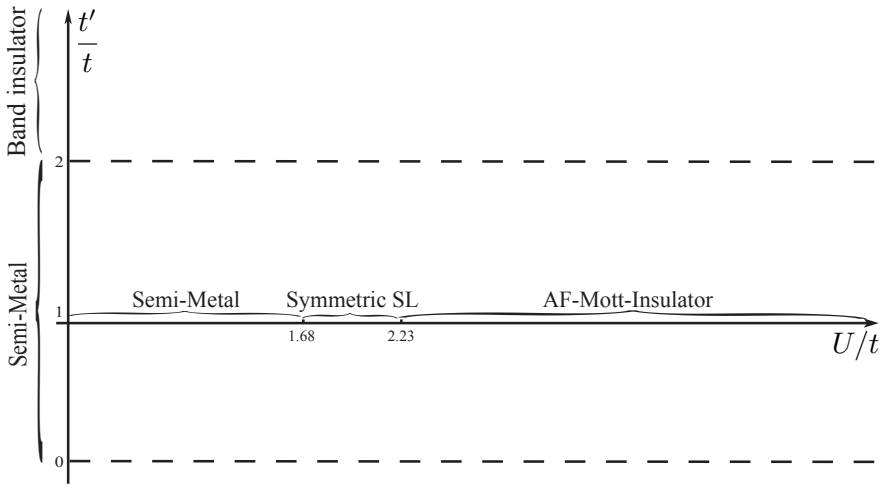

Figure 1.7: The incomplete phase diagram delineating the noninteracting limit on the vertical axis and the isotropic limit on the horizontal axis. The aim of this thesis is to complete the blank part of this phase diagram.

absence of the interaction term, which is delineated by the vertical axis, the topological phase transition between the semi-metallic and the band-insulating phases occurs at $t' = 2t$; while in the isotropic limit of $t' = t$, which is delineated by the horizontal axis, and within mean-field treatments, the metal-Mott-insulator and the antiferromagnetic transitions occur at $U = 1.68t$ and $U = 2.23t$, respectively. The aim of the current study is to investigate the fate of the various phases in the blank portions of the above phase diagram.

A second motivation comes from experimental consideration. In setting up the honeycomb optical lattice, practical experimental errors in the form of anisotropies in the laser beams are unavoidable. Thus studying the fate of various phases under these anisotropies is of experimental interest.

1.5 Plan

The discussion in this thesis is organized as follows. For a more detailed look at the realization of the topological transition in the honeycomb optical lattice from the experimental point of view, we calculate the explicit expression for the anisotropic hopping amplitudes (Chapter 2). Next, in Chapter 3, we investigate the antiferromagnetic transition using the self-consistent mean-field method. As a complement to the mean-field calculation, we also calculate the transition into the spin-ordered state using Stoner's criterion. In order to better understand the antiferromagnetic phase, we then derive effective Hamiltonians for the large-U limit, which enables us to make connection between the antiferromagnetic and the spin-liquid phases, the latter of which is studied in Chapter 4. Finally, as an attempt to separate the Mott transition from the antiferromagnetic transition, we use the slave-rotor method to study the possible spin-liquid phase in the honeycomb lattice (Chapter 4). After completing the study of the phase diagram concerning the monolayer case, we study in Chapter 5 the pairing transition in the AA-stacked bilayer honeycomb lattice with attractive interaction, which is related to the repulsive model that we previously studied, via partial particle-hole-transformation. The last chapter (Chapter 6) summarizes our results, and also includes comments on possible further investigations. Parts of this thesis, namely the mean-field self-consistent treatment of the antiferromagnetic transition and the slave-rotor calculation of the spin-liquid transition, both of which concern the monolayer case, have been published in *Emergent Spin Liquids in the Hubbard Model on the Anisotropic Honeycomb Lattice*, Euro. Phys. Lett. 95, 47013 (2011).

2

The hopping amplitudes

The nearest-neighbor hopping amplitudes, which were denoted as $t_{1,2,3}$ in Figure 1.1(a) in the previous chapter, are essential parameters in the tight-binding description of the honeycomb lattice. For example, the topological properties of the band structure depend on the hopping amplitudes, the variation of which can ultimately lead to the topological phase transition discussed in the previous chapter. As another example, the effective description of the lattice system can be reduced to that of coupled dimers, or to that of coupled chains, by varying the hopping amplitudes, as will be discussed in subsequent chapters. In an optical lattice, the hopping amplitudes can be varied by changing the parameters of the laser beams, most notably their amplitudes and/or respective angles.

In this chapter we calculate the hopping amplitude for an optical lattice explicitly using the harmonic approximation. We begin with the calculation for the symmetric honeycomb lattice, implement the anisotropy as the next step, and end this chapter with a discussion of the topological phase transition in the optical lattice in the light of the explicit expressions for the hopping amplitudes.

2.1 The case of the symmetric honeycomb lattice

In a bipartite lattice, the nearest-neighbor hopping amplitudes are the off-diagonal components of the matrix form of the Hamiltonian. To be explicit, we consider an arbitrarily chosen lattice site 0, on which the wave function is denoted by ψ_0. The hopping amplitude to a neighboring site j may then be calculated as [15]

$$t_j = \int \psi_0 \mathcal{H}_{\text{pert}} \psi_j \mathrm{d}^2\boldsymbol{r}, \tag{2.1}$$

where ψ_j is the wave function on site j. $\mathcal{H}_{\text{pert}}$ is the perturbative Hamiltonian, which is given by the difference between the total Hamiltonian $\mathcal{H}$ and the local Hamiltonian $\mathcal{H}_0$: [1]

$$\begin{aligned} \mathcal{H}_{\text{pert}} &= \mathcal{H} - \mathcal{H}_0, \\ \mathcal{H} &= \frac{\boldsymbol{p}^2}{2M} + V, \\ \mathcal{H}_0 &= \frac{\boldsymbol{p}^2}{2M} + V_{\text{local}}, \end{aligned} \tag{2.2}$$

where M is the particle mass, V is the electromagnetic dipole potential formed by the laser beams, and V_{local} is the local potential, which, as we will show later, can be approximated by the 2D harmonic potential. Note that the wave functions ψ_j are the atomic orbital wave functions of the local Hamiltonian $\mathcal{H}_0$ on each lattice site.

As an example, we consider the setup sketched in Figure 1.3(a), namely that of three counter propagating coplanar laser beams with equal intensities, equal wave lengths and identical polarization arranged with equal angular separation between any two wave vectors. The wave vectors can be taken as

$$\boldsymbol{k}_1 = k(1,0),\ \boldsymbol{k}_2 = k(-\frac{1}{2}, \frac{\sqrt{3}}{2}),\ \boldsymbol{k}_3 = k(-\frac{1}{2}, -\frac{\sqrt{3}}{2}) \tag{2.3}$$

with $k = |\boldsymbol{k}_{1,2,3}|$. The dipole potential of such a setup is given by [31]

$$V = V_0 \left\{ 1 + 4\cos^2\left(\frac{\sqrt{3}}{2}ky\right) + 4\cos\left(\frac{\sqrt{3}}{2}ky\right)\cos\left(\frac{3}{2}kx\right) \right\}, \tag{2.4}$$

where x and y are the spatial Cartesian coordinates. We have $V_0 > 0$ and $V_0 \propto E_0^2$, where E_0 is the amplitude of the electric field component of the laser beams. The proportionality constant between V_0 and E_0^2 is the real part of the polarizability of the atoms, which is positive for red-detuned laser systems and

[1] Notice that $\mathcal{H}$ and $\mathcal{H}_0$ in this chapter are not the Hubbard Hamiltonians.

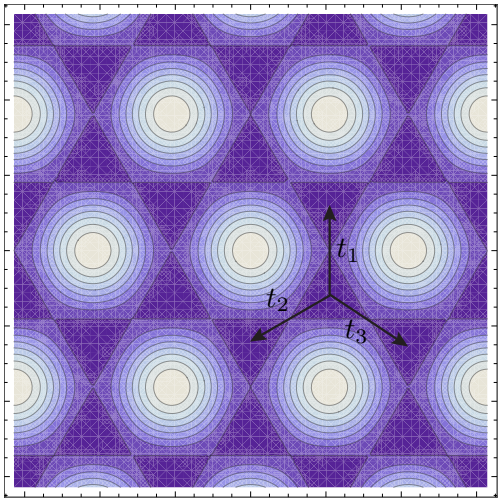

Figure 2.1: The potential landscape of a perfect honeycomb optical lattice. Dark color corresponds to low potential, which are the locations of lattice sites, while light color corresponds to high potential. The hopping amplitudes $t_{1,2,3}$ between nearest-neighboring sites are indicated.

negative for blue-detuned ones [31]. This is the reason for the dependence of the optical lattice structure on the detuning, as mentioned in the caption of Figure 1.3(a). Notice the formal resemblance between Equation (2.4) and $|\gamma^{\boldsymbol{k}}|^2$, where $|\gamma^{\boldsymbol{k}}|$ is shown in Equation (1.19). A contour plot of the above potential is shown in Figure 2.1. The minima of this potential closest to the origin are the corners of a hexagon:

$$a\,(0,\pm 1)\,,\ a\left(\pm\frac{\sqrt{3}}{2},\pm\frac{1}{2}\right), \tag{2.5}$$

where $a = \frac{4\pi}{3\sqrt{3}k}$ is lattice constant of the honeycomb optical lattice. Clearly the minima of this potential form a honeycomb lattice, which is dual to the triangular lattice formed by the maxima of the potential. The honeycomb lattice is formed with a positive (blue) detuning, which is the case that interests us.

The potential function (2.4) has a maximum at the origin. To simplify the calculation of the hopping parameter, we shift the origin to a minimum (a lattice site). In particular, we replace y by $y + a$ in the potential function, so that the origin is shifted to $a(0, 1)$ in the original coordinate system, and we consider hopping from this site to its nearest neighbors. The vectors connecting this site

to its nearest neighbors are

$$\boldsymbol{c}_1 = a\,(0,1)\,,\ \boldsymbol{c}_2 = a\left(-\frac{\sqrt{3}}{2},-\frac{1}{2}\right),\ \boldsymbol{c}_3 = a\left(\frac{\sqrt{3}}{2},-\frac{1}{2}\right), \tag{2.6}$$

similar to the vectors (1.3). The transformed potential function is

$$V = 2V_0\left[1+\sin^2\left(\frac{\sqrt{3}}{2}ky\right)+\frac{\sqrt{3}}{2}\sin\left(\sqrt{3}ky\right)\right.$$
$$\left.-\sqrt{3}\cos\left(\frac{3}{2}kx\right)\sin\left(\frac{\sqrt{3}}{2}ky\right)-\cos\left(\frac{3}{2}kx\right)\cos\left(\frac{\sqrt{3}}{2}ky\right)\right]. \tag{2.7}$$

Expanding the above function up to second order in x and y around the origin, we obtain

$$V_{\text{local}} = \frac{9}{4}V_0k^2r^2 = \frac{1}{2}M\omega_0^2r^2, \tag{2.8}$$

with $r^2 = x^2+y^2$. V_{local} is a 2D rotationally invariant harmonic potential, the angular frequency of which is $\omega_0 = 3\sqrt{V_0E_{\text{R}}}$, where

$$E_{\text{R}} = \frac{k^2}{2M} \tag{2.9}$$

is the recoil energy, which is the energy transferred to the atom in an photon-absorption event. The recoil energy is a measure of how much the particles are heated up in the laser field. Thus the local Hamiltonian is that of an isotropic 2D harmonic oscillator

$$\mathcal{H}_0 = \omega_0\,(1+\hat{n}_x+\hat{n}_y)\,, \tag{2.10}$$

with equal frequency in the x- and y-directions. Assuming that all particles occupy the lowest vibrational energy level, the wave functions at the origin and

its neighboring sites are

$$\psi_0 = \frac{1}{a_0\sqrt{\pi}}\exp\left(-\frac{r^2}{2a_0^2}\right),\ \psi_j = \frac{1}{a_0\sqrt{\pi}}\exp\left(-\frac{(\boldsymbol{r}-\boldsymbol{d}_j)^2}{2a_0^2}\right), \tag{2.11}$$

where a_0 is the length scale of the harmonic oscillator, given by $a_0 = \sqrt{\frac{1}{M\omega_0}}$.

Now that we have everything that is needed for the evaluation of t_j, we substitute the relevant expressions into equation (2.1), carry out the integration, and express everything in terms of V_0 and

$$\rho = \frac{V_0}{E_\mathrm{R}}, \tag{2.12}$$

we find that for the ground state, for which $n_x = n_y = 0$,

$$\int \psi_0 \frac{\boldsymbol{p}^{\,2}}{2M}\psi_j \mathrm{d}^2\boldsymbol{r} = V_0\exp\left(-\frac{2\pi^2}{9}\sqrt{\rho}\right)\times\frac{3}{2\sqrt{\rho}}\left(1-\frac{2\pi^2}{9}\sqrt{\rho}\right), \tag{2.13}$$

$$-\int \psi_0 \mathcal{H}_0 \psi_j \mathrm{d}^2\boldsymbol{r} = -V_0\exp\left(-\frac{2\pi^2}{9}\sqrt{\rho}\right)\times\frac{3}{\sqrt{\rho}}, \tag{2.14}$$

$$\int \psi_0 V \psi_j \mathrm{d}^2\boldsymbol{r} = V_0\exp\left(-\frac{2\pi^2}{9}\sqrt{\rho}\right)\times\left[3-2\exp\left(-\frac{1}{2\sqrt{\rho}}\right)\right]. \tag{2.15}$$

The hopping parameter is given by the sum of these three terms:

$$t = V_0\times\left\{3-\frac{\pi^2}{3}-\frac{3}{2\sqrt{\rho}}-2\exp\left(-\frac{1}{2\sqrt{\rho}}\right)\right\}\exp\left(-\frac{2\pi^2}{9}\sqrt{\rho}\right). \tag{2.16}$$

We consider the case of $\rho \gg 1$, which is appropriate for our tight-binding calculation. To a first approximation, we have

$$t \approx -V_0\times\left(\frac{\pi^2}{3}-1\right)\exp\left(-\frac{2\pi^2}{9}\sqrt{\rho}\right), \tag{2.17}$$

which is negative. Note that in the Hubbard Hamiltonians in the previous chapter as well as in subsequent ones, we use instead the convention that $t > 0$, and denote the hopping amplitude as $-t$.

The semi-classical method introduced in Reference [77] offers a more accurate way of calculating the hopping amplitude. It proposes to evaluate t using the semi-classical instanton method, in which a nearest-neighbor-hopping event is interpreted as an intanton tunneling event along the trajectory connecting the nearest-neighboring sites, going through the classically forbidden region, which corresponds to an optical potential hill in an optical lattice. The hopping amplitude is then related to the propagator of such a tunneling event, which is evaluated with the help of the Feynman path-integration formulation. Employing this method, the hopping amplitude is [25]

$$|t| \approx V_0^{\frac{3}{4}} E_{\mathrm{R}}^{\frac{1}{4}} \times 1.861 \exp\left[-1.582\sqrt{\rho}\right]. \tag{2.18}$$

As we can see, the functional dependence on $\sqrt{\rho}$ in the right-hand sides of Equations (2.17) and (2.18) are the same, albeit with different factors.

In this chapter, we aim at a rough estimation of the achievability of the topological phase transition in the optical lattice by attempting to calculate the anisotropic hopping amplitudes in the honeycomb lattice. Thus we stick to the harmonic approximation, which makes our goals much more attainable, as presented next.

2.2 The case of the asymmetric honeycomb lattice

As discussed in the previous chapter, an interesting physical situation arises when the nearest-neighbor-hopping amplitudes are anisotropic, i.e. when one breaks the $\frac{2\pi}{3}$-rotational invariance of the setup in Figure 1.3(a). In particular, the topological phase transition occurs when the hopping amplitudes do not satisfy the triangle inequality (1.27). In an optical lattice, this anisotropy can be achieved by imbalancing the parameters of the laser beams. In this section, we consider

the simple variation of the setup sketched in Figure 1.3(a), namely that with the intensity of one laser beam being different from that of the other two:

$$E_{2,3} = E_0, \text{ and } E_1 = \alpha E_0 \text{ with } 0 < \alpha \leq 2, \tag{2.19}$$

while maintaining wavelength, polarization and phase fixed. We choose the laser beam with the horizontal wave vector as E_1. Notice that α here must be less than 2, otherwise the nearest neighboring potential minima, which correspond to lattice sites, in the vertical direction of the honeycomb lattice merge, and instead of distorted honeycomb lattice, a triangular one is formed. This is analogous to the topological phase transition in reciprocal space.

The dipole potential in this case is given by

$$V' = V_0 \left\{ \alpha^2 + 4\cos\left(\frac{\sqrt{3}}{2}ky\right)\left[\cos\left(\frac{\sqrt{3}}{2}ky\right) + \alpha\cos\left(\frac{3}{2}kx\right)\right]\right\}, \tag{2.20}$$

where V_0 is defined in the same way as in the symmetric case before. We denote relevant quantities in this section by primed expressions. The contour plots for the above potential for the two cases of $E_1 < E_0$ ($\alpha < 1$) and $E_1 > E_0$ ($\alpha > 1$) are plotted in Figure 2.2.

As we can see qualitatively by comparing the figures 2.2 and 2.1, the effect of imbalanced intensities is that the two sub-lattices move with respect to each other, in the direction perpendicular to the wave vector of the laser beam whose intensity is different, which is one with the horizontal wave vector in the current case. Defining ζ such that

$$\cos(\zeta\pi) = \frac{\alpha}{2}, \tag{2.21}$$

the minima of the distorted potential are located at

$$a\left(0, \pm\frac{3}{2}(1-\zeta)\right),\ a\left(\pm\frac{\sqrt{3}}{2}, \pm\frac{3}{2}\zeta\right), \tag{2.22}$$

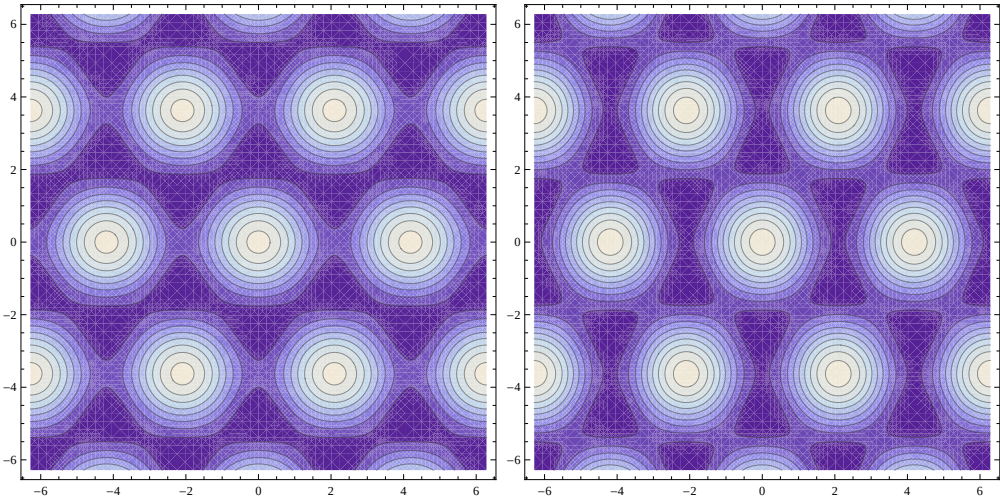

Figure 2.2: The potential landscape of a distorted honeycomb optical lattice. The left figure is for $E_1 = 0.9E_0$, while the right is for $E_1 = 1.1E_0$. As before, dark color corresponds to low potential (lattice sites), while light color corresponds to high potential.

in the coordinate in which the potential (2.20) is defined. Here $a = \frac{4\pi}{3\sqrt{3}k}$ is the same value as in the case of the symmetric honeycomb lattice. The requirement $0 < \alpha \leq 2$ implies $0 \leq \zeta < \frac{1}{2}$. If we set $\zeta = \frac{1}{3}$, the perfect honeycomb lattice is recovered. The exact amount of spatial shift of the two sub-lattices, relative to the lattice sites of the perfect honeycomb lattice, is $\pm\frac{1}{2}(1 - 3\zeta)$. However, the internal structure of each sub-lattice remains unchanged, and so do the structures of the background Bravais lattice and that of the reciprocal lattice.

Apart from these geometric changes, as we can see from Figure 2.2, the potential barriers through which the atoms have to tunnel have also been changed. In particular, for the case $E_1 > E_0$, the barrier between vertical neighbors has become lower, while that between the other neighbors has become higher. Both the geometric changes and the potential changes indicate a larger hopping amplitude between vertical pairs of nearest neighbors than between the other pairs for $E_1 > E_0$. Thus one may hope to achieve the situation described in Equation (1.29) by increasing E_1 with respect to E_0.

To proceed with the calculation, we again shift the origin of the potential

function to one of its minima, $d(0, \frac{3}{2}(1-\zeta))$ in this case. Define β such that

$$\sqrt{\frac{1}{3}(4-\alpha^2)} = \frac{2}{\sqrt{3}}\sin(\zeta\pi) = \beta. \tag{2.23}$$

The resulting potential function is

$$V' = V_0 \times 2\left[\alpha^2 + \left(2-\alpha^2\right)\sin^2\left(\frac{\sqrt{3}}{2}ky\right) + \frac{\sqrt{3}}{2}\alpha\beta\sin\left(\sqrt{3}ky\right)\right.$$
$$\left.-\sqrt{3}\alpha\beta\cos\left(\frac{3}{2}kx\right)\sin\left(\frac{\sqrt{3}}{2}ky\right) - \alpha^2\cos\left(\frac{3}{2}kx\right)\cos\left(\frac{\sqrt{3}}{2}ky\right)\right]. \tag{2.24}$$

The vectors connecting the site at the origin to its nearest neighbors are

$$\boldsymbol{c}'_1 = a\left(0, 3\zeta\right), \ \boldsymbol{c}'_{2,3} = a\left(\mp\frac{\sqrt{3}}{2}, -\frac{3}{2}\left(1-2\zeta\right)\right). \tag{2.25}$$

The changes in the locations of the minima and the vectors connecting nearest neighbors are part of the geometric changes.

To obtain the local approximation, we expand the above function around the origin, and obtain

$$V'_{\text{local}} = \frac{9}{4}V_0k^2\left(\alpha^2x^2 + \beta^2y^2\right) = \frac{1}{2}M\left(\omega_x^2x^2 + \omega_y^2y^2\right), \tag{2.26}$$

with $\omega_x = \alpha\omega_0$, $\omega_y = \beta\omega_0$, and $\omega_0 = 3\sqrt{V_0E_{\text{R}}}$ is the local angular frequency of the perfect honeycomb optical lattice. The local Hamiltonian in this case is still harmonic, but with different angular frequencies for the x and y directions:

$$\mathcal{H}'_0 = \omega_x\left(\frac{1}{2} + \hat{n}_x\right) + \omega_y\left(\frac{1}{2} + \hat{n}_y\right). \tag{2.27}$$

The same result is obtained if the expansion is done at any other minimum.

The change of the form of the local potential therefore has two effects: the energy level spacings are altered, and the length scales of both directions are changed to

$$a_{0x} = \frac{a_0}{\sqrt{\alpha}}, a_{0y} = \frac{a_0}{\sqrt{\beta}}. \tag{2.28}$$

Correspondingly, the wave functions at the origin and at its nearest neighbors are

$$\psi'_0 = \psi'_{0x}\psi'_{0y} = \frac{1}{\sqrt{a_{0x}a_{0y}\pi}}\exp\left(-\frac{x^2}{2a_{0x}^2} - \frac{y^2}{2a_{0y}^2}\right) \tag{2.29}$$

$$\text{and} \quad \psi'_j = \psi'_{jx}\psi'_{jy} = \frac{1}{\sqrt{a_{0x}a_{0y}\pi}}\exp\left(-\frac{\left(x-c'_{jx}\right)^2}{2a_{0x}^2} - \frac{\left(y-c'_{jy}\right)^2}{2a_{0y}^2}\right), \tag{2.30}$$

respectively. These changes are classified as local potential form changes. It is easy to see that these functions can be obtained by first replacing, in the wave functions of the perfect honeycomb lattice, x by $\sqrt{\alpha}x$, y by $\sqrt{\beta}y$, c'_{jx} by $\sqrt{\alpha}c'_{jx}$ and c'_{jy} by $\sqrt{\beta}c'_{jy}$: these are changes in length scale; and second, multiply ψ_x and ψ_y by $\alpha^{\frac{1}{4}}$ and $\beta^{\frac{1}{4}}$, respectively.

Given the geometric and local potential form changes and our previous result for the symmetric honeycomb lattice, we can obtain the expression of the hopping parameter for this case by inspection. In the following equations, primed coordinates are the original coordinates, unprimed ones are rescaled such that $x = \sqrt{\alpha}x'$ etc.. Primed and unprimed wave functions and operators are those for the asymmetric and symmetric honeycomb lattices, respectively.

First, the kinetic energy term reads

$$\begin{aligned}
\int \psi'_0 \frac{\boldsymbol{p'}^{\,2}}{2M}\psi'_j \mathrm{d}^2\boldsymbol{r'} &= -\frac{\hbar^2}{2M}\left(\int \psi'_0\frac{\partial^2}{\partial x'^2}\psi'_j\mathrm{d}^2\boldsymbol{r'} + \int \psi'_0\frac{\partial^2}{\partial y'^2}\psi'_j\mathrm{d}^2\boldsymbol{r'}\right) \\
&= -\frac{\hbar^2}{2M}\left(\alpha\int \psi_0\frac{\partial^2}{\partial x^2}\psi_j\mathrm{d}^2\boldsymbol{r} + \beta\int \psi_0\frac{\partial^2}{\partial y^2}\psi_j\mathrm{d}^2\boldsymbol{r}\right) \\
&= \frac{\hbar^2}{2Ma_0^2}\exp\left(-\frac{\tilde{c}'^2_j}{4a_0^2}\right)\left[\frac{\alpha+\beta}{2} - \frac{1}{4a_0^2}\left(\alpha^2 c'^2_{jx} + \beta^2 c'^2_{jy}\right)\right]
\end{aligned} \tag{2.31}$$

where $\tilde{c}_j'^2 = \alpha c_{jx}'^2 + \beta c_{jy}'^2$.

Second, for the local harmonic approximation term, with $n_x = n_y = 0$ for the ground state, we have

$$\begin{aligned} -\int \psi_0' \mathcal{H}_0' \psi_j' \mathrm{d}^2\boldsymbol{r'} &= -\int \psi_0' \left[\hbar\omega_x(\frac{1}{2} + \hat{n}_x) + \hbar\omega_y\left(\frac{1}{2} + \hat{n}_y\right)\right] \psi_j' \mathrm{d}^2\boldsymbol{r'} \\ &= -\frac{\alpha+\beta}{2}\hbar\omega_0 \int \psi_0 \psi_j \mathrm{d}^2\boldsymbol{r} \\ &= -\hbar\omega_0 \exp\left(-\frac{\tilde{c}_j'^2}{4a_0^2}\right)\frac{\alpha+\beta}{2} \\ &= -\frac{\hbar^2}{Ma_0^2}\exp\left(-\frac{\tilde{c}_j'^2}{4a_0^2}\right)\frac{\alpha+\beta}{2} \end{aligned} \tag{2.32}$$

In words, we started from the corresponding terms for the perfect honeycomb lattice, separated them into x and y parts; replaced $\left(c_j^2,\ c_{jx}^2,\ c_{jy}^2\right)$ respectively by $\left(\tilde{c}_j'^2,\ \alpha c_{jx}'^2,\ \beta c_{jy}'^2\right)$, multiplied the x and y parts respectively by α and β, the results of which are then added up. The steps above reflect only local potential form changes, because geometric changes do not affect the functional forms of these two terms. However, because of the geometric changes, the values of c_{jx} and c_{jy} are replaced by c_{jx}' and c_{jy}'.

The dipole potential term reads

$$\int \psi_0' V' \psi_j' \mathrm{d}^2\boldsymbol{r'} \tag{2.33}$$

where V' is given by equation (2.24). The coefficients of the sinusoidal functions are different from those in the potential function for the symmetric case, i.e. Equation (2.7). Now consider the integrations involving a sinusoidal function. For example, we have

$$\int \psi_0' \sin\left(\frac{\sqrt{3}}{2}ky'\right)\psi_j' \mathrm{d}^2\boldsymbol{r'} = \int \psi_0 \sin\left(\frac{\sqrt{3}}{2}\frac{k}{\sqrt{\beta}}y\right)\psi_j \mathrm{d}^2\boldsymbol{r}. \tag{2.34}$$

Because x', y' and k always appear, in the arguments of the sinusoidal functions, as the products $\frac{3}{2}kx'$ and $\frac{\sqrt{3}}{2}ky'$, they appear as $\frac{3}{2}\frac{k}{\sqrt{\alpha}}x$ and $\frac{\sqrt{3}}{2}\frac{k}{\sqrt{\beta}}y$ after rescaling. In other words, from the corresponding terms for the perfect honeycomb case, replace $\left(c_j^2,\ c_{jx}^2,\ c_{jy}^2,\ \frac{3}{2}k,\ \frac{\sqrt{3}}{2}k\right)$ by $\left(\tilde{c}_j'^2,\ \alpha c_{jx}'^2,\ \beta c_{jy}'^2,\ \frac{3}{2}\frac{k}{\sqrt{\alpha}},\ \frac{\sqrt{3}}{2}\frac{k}{\sqrt{\beta}}\right)$, respectively. Again, these are consequences of local potential form changes.

Multiplying these integration results with the corresponding coefficients in equation (2.24), summing up all relevant terms, and recasting everything in terms of V_0 and ρ as before, we obtain

$$\begin{aligned} t_j &= V_0 \times \exp\left(-\frac{2\pi^2}{9}\sqrt{\rho}\frac{\tilde{c}_j'^2}{a^2}\right)\left\{\left(2+\alpha^2\right)+f'\left(\boldsymbol{c}_j'\right)\times\exp\left(-\frac{1}{2\beta\sqrt{\rho}}\right)\right. \\ &\left. -\frac{3}{4\sqrt{\rho}}\left(\alpha+\beta\right)-\frac{\pi^2}{3}\frac{\alpha^2 c_{jx}'^2+\beta^2 c_{jy}'^2}{a^2}\right\}, \end{aligned} \tag{2.35}$$

where

$$\begin{aligned} f'(\boldsymbol{c}_j') &= -(2-\alpha^2)\cos\left(\frac{\sqrt{3}}{2}kc_{jy}'\right)-2\sqrt{3}\alpha\beta\cos\left(\frac{3}{4}kc_{jx}'\right)\sin\left(\frac{\sqrt{3}}{4}kc_{jy}'\right) \\ &\quad +\sqrt{3}\alpha\beta\sin\left(\frac{\sqrt{3}}{2}kc_{jy}'\right)-2\alpha^2\cos\left(\frac{3}{4}kc_{jx}'\right)\cos\left(\frac{\sqrt{3}}{4}kc_{jy}'\right). \end{aligned} \tag{2.36}$$

In the case $\rho \gg 1$, and to a first approximation, we have

$$t_j = V_0 \times \exp\left(-\frac{2\pi^2}{9}\sqrt{\rho}\frac{\tilde{c}_j'^2}{a^2}\right)\left\{2+\alpha^2+f'(\boldsymbol{c}_j')-\frac{\pi^2}{3}\frac{\alpha^2 c_{jx}'^2+\beta^2 c_{jy}'^2}{a^2}\right\}. \tag{2.37}$$

Straightforward calculation gives

$$f'(\boldsymbol{c}_{1,3}') = -2,\ \ f'(\boldsymbol{c}_2') = 2(1-2\alpha). \tag{2.38}$$

So we have, after evaluating $\tilde{c}_j'^2$ and $(\alpha^2 c_{jx}'^2 + \beta^2 c_{jy}'^2)$,

$$t_1 = V_0 \times \exp\left(-2\pi^2\sqrt{\rho}\beta\zeta^2\right)\left[(\alpha-2)^2 - 3\pi^2\beta^2\zeta^2\right], \tag{2.39a}$$

$$t_{2,3} = V_0 \times \exp\left(-\frac{\pi^2}{6}\sqrt{\rho}\left[\alpha + 3\beta(1-2\zeta)^2\right]\right)\left\{\alpha^2 - \pi^2\left[1 + 3\zeta(\zeta-1)\beta^2\right]\right\}. \tag{2.39b}$$

(2.39c)

It is easy to check from the above expressions that in general we have $|t_1| \geq |t_{2,3}|$, where the equal sign holds if $\alpha = 1$, implying that $\beta = 1$ and $\zeta = \frac{1}{3}$, and the greater-than sign holds if $\alpha > 1$.

It will be shown in the next chapter where we present our calculation for the antiferromagnetic transition line, that the geometric changes (in the form of α, β or ζ as defined in this chapter) do not appear in the tight-binding band structure directly. Their footprints are entirely contained the hopping amplitudes $t_{1,2,3}$.

2.3 The topological phase transition

As already mentioned in the previous chapter, imbalance in hopping parameters drives the relocation of the Dirac points in the FBZ; in order for the Dirac points to exist, the magnitudes of the three hopping amplitudes must satisfy the triangular inequalities, otherwise the two inequivalent Dirac points will merge into one (or differ by a primitive reciprocal lattice vector, depending on which pair of inequivalent Dirac points one considers). This is the point of topological transition from a semi-metallic phase to a insulating phase. This can be understood from the right half of Figure 2.2: If α is large, each atomic site communicates only with its nearest neighbor in the vertical direction. In other words, the system approaches an insulating zero-dimensional limit.

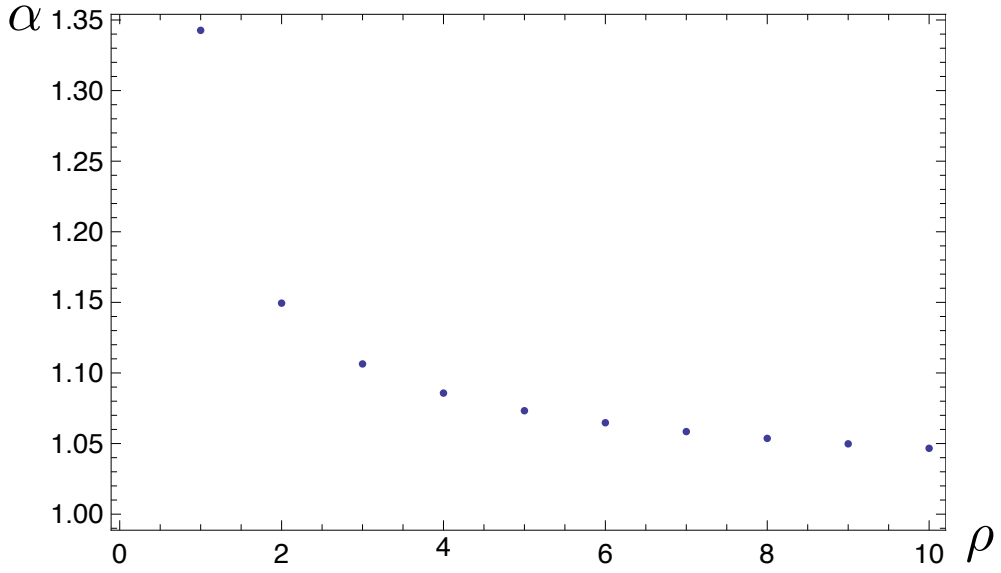

Figure 2.3: The values of $\alpha = E_1/E_0$ that satisfy Equation (2.40) for a few values of ρ. For $\rho = 7$, as an example, $\alpha \approx 1.058$, indicating that $\sim 6\%$ of difference in laser amplitudes is required to achieve the topological transition.

Given the expressions in the previous section, the transition takes place at

$$\frac{t_1}{t_{2,3}} = \exp\left[\frac{\pi^2}{6}\sqrt{\rho}(\alpha + 3\beta(1-2\zeta)^2 - 12\beta\zeta^2)\right] \frac{(\alpha-2)^2 - 3(\pi\beta\zeta)^2}{\alpha^2 - \pi^2[1+3\zeta(\zeta-1)\beta^2]} = 2. \tag{2.40}$$

The exponential dependence of $\frac{t_1}{t_{2,3}}$ on $\sqrt{\rho}$ and α is inherited from the form of the hopping parameter for a symmetric honeycomb lattice, i.e. Equation (2.17). Choosing a reasonable value for ρ ($>> 1$ for tight binding calculation), this ratio changes rapidly with α as a result of this exponential factor. As illustrated in Figure 2.3, Equation (2.40), and thus the topological quantum phase transition, can be achieved with α being a few percent greater than unity. Because the exponential dependence of the expression (2.17) on $\sqrt{\rho}$, albeit with different prefactors, is also present in the semi-classical result (2.18), we expect the above conclusion regarding the achievability of the topological phase transition to hold for the semi-classical result. Note that α is the ratio between electric field amplitudes. The actual parameter which experimentalists control and measure is usually the intensity, which is proportional to the square of this amplitude.

3

Antiferromagnetic transition

As already discussed in the Introduction, because the honeycomb lattice is bipartite, antiferromagnetic ordering of spins is imminent in the large-U limit. In this chapter, we analyze the antiferromagnetic transition in the anisotropic honeycomb lattice. We focus our attention on the situation described by Equation (1.29). Reference [78] suggests that the antiferromagnetic transition in the honeycomb lattice is first order in nature. Nevertheless, our analysis in this thesis is based on the assumption that this is a second order phase transition.

As a first step, the mean-field self-consistent method will be used to determine the transition line [79–81]. In this treatment, the transition line is approached from the strongly-interacting side, in which the antiferromagnetic order is assumed to be the ground state in the large-U limit. Assuming a second order phase transition, the transition line is then determined by the vanishing of the antiferromagnetic order parameter. The phase diagram combining the results of this mean-field treatment and the topological transition discussed in Section 1.2.2 will be presented as the result of this investigation.

The mean-field analysis is followed up by the Stoner's criterion calculation. In this method, the magnetic susceptibility is calculated in the eigenspace of the kinetic Hamiltonian. A magnetic instability is signaled by the divergence of the susceptibility, which point in parameter space is then identified with the phase transition point. This method complements the previous mean-field calculation, in the sense that the transition line is approached from the weakly-interacting side.

Finally, we derive effective models for the system in the large-U limit. This derivation will be performed in the spirit of the t-J model. By emphasizing the

dimer structure, which dominates in the large-t' limit, the effective Hamiltonian offers deeper physical insight into the nature of the antiferromagnetic transition.

3.1 Mean-field self-consistent calculation

3.1.1 Mean field decoupling

The starting point of our calculation is the Hamiltonian

$$\mathcal{H} = \mathcal{H}_0 + \mathcal{V}, \tag{3.1}$$

where

$$\mathcal{H}_0 = -\sum_{\langle ij\rangle\sigma} t_{ij} a^\dagger_{i\sigma} b_{j\sigma} + \text{H.c.} - \mu \sum_{i\alpha\sigma} n^\alpha_{i\sigma}, \tag{3.2}$$

where the hopping amplitudes $t_{1,2,3}$ are as described in Equation (1.29), and

$$\mathcal{V} = U \sum_{i\alpha} (n^\alpha_{i\uparrow} - \frac{1}{2})(n^\alpha_{i\downarrow} - \frac{1}{2}), \tag{3.3}$$

where U is the interaction strength, and $n^\alpha_{i\sigma} = \alpha^\dagger_{i\sigma}\alpha_{i\sigma}$, where $\alpha = a, b$, is the number operator for lattice site i in sublattice α and spin-σ. The band structure of $\mathcal{H}_0$ has been analyzed in Section (1.2.1) and (1.2.2).

The order parameter that we consider is

$$\Delta^\alpha = \langle n^\alpha_{i\uparrow} - n^\alpha_{i\downarrow} \rangle, \tag{3.4}$$

which is the average population imbalance between the two spins on a randomly chosen lattice site i. In this mean-field treatment, we assume Δ^α to be spatially uniform, i.e. independent of the lattice site index i. The superscript $\alpha = A, B$ is

the sub-lattice index, and we assume

$$\Delta^A = -\Delta^B \equiv \Delta, \tag{3.5}$$

which makes it clear that we are looking at the antiferromagnetic phase.

Now we consider a particular lattice site i. The number operators in Equations (3.6-3.9) concern this lattice site, so that we can omit the lattice site index i without causing any confusion. We have

$$n_\uparrow^\alpha(n_\downarrow^\alpha - n_\uparrow^\alpha) = n_\uparrow^\alpha n_\downarrow^\alpha - n_\uparrow^\alpha \tag{3.6}$$

where we have taken into account the fact that $(n_\sigma^\alpha)^2 = n_\sigma^\alpha$, so that

$$\begin{aligned} n_\uparrow^\alpha n_\downarrow^\alpha &= n_\uparrow^\alpha - n_\uparrow^\alpha(n_\uparrow^\alpha - n_\downarrow^\alpha) \\ &= n_\uparrow^\alpha \left[1 - (n_\uparrow^\alpha - n_\downarrow^\alpha)\right] \\ &\approx n_\uparrow^\alpha(1 - \Delta^\alpha), \end{aligned} \tag{3.7}$$

where we have applied the approximation $n_\uparrow^\alpha - n_\downarrow^\alpha \approx \Delta^\alpha$ in the last line. Similarly, we can obtain

$$n_\uparrow^\alpha n_\downarrow^\alpha \approx n_\downarrow^\alpha(1 + \Delta^\alpha). \tag{3.8}$$

Symmetrization between the two spins then yields

$$n_\uparrow^\alpha n_\downarrow^\alpha \approx \frac{1}{2}\left[n_\uparrow^\alpha(1 - \Delta^\alpha) + n_\downarrow^\alpha(1 + \Delta^\alpha)\right]. \tag{3.9}$$

In the context of the mean-field approximation as shown in Equation (3.9), and transforming to the momentum space using the Fourier transform defined in

(1.15), we obtain the mean-field Hamiltonian

$$\mathcal{H}^{\Delta} = \sum_{\boldsymbol{k}} d^{\dagger}_{\boldsymbol{k}} M_{\boldsymbol{k}} d_{\boldsymbol{k}}, \text{ with } d^{\dagger}_{\boldsymbol{k}} = (a^{\dagger}_{\boldsymbol{k}\uparrow}\ b^{\dagger}_{\boldsymbol{k}\uparrow}\ a^{\dagger}_{\boldsymbol{k}\downarrow}\ b^{\dagger}_{\boldsymbol{k}\downarrow}), \tag{3.10}$$

and

$$M_{\boldsymbol{k}} = \begin{pmatrix} -\frac{U\Delta}{2} & -\gamma^{\boldsymbol{k}}_{t'} & 0 & 0 \\ -\gamma^{\boldsymbol{k}*}_{t'} & \frac{U\Delta}{2} & 0 & 0 \\ 0 & 0 & \frac{U\Delta}{2} & -\gamma^{\boldsymbol{k}}_{t'} \\ 0 & 0 & -\gamma^{\boldsymbol{k}*}_{t'} & -\frac{U\Delta}{2} \end{pmatrix}. \tag{3.11}$$

The eigen-energies are

$$E^{\boldsymbol{k}}_{\lambda=\pm} = \lambda\sqrt{\left(\frac{U\Delta}{2}\right)^2 + |\gamma^{\boldsymbol{k}}_{t'}|^2}, \tag{3.12}$$

with each eigenvalue being two-fold degenerate, corresponding to the two-fold spin-degeneracy. Here $|\gamma^{\boldsymbol{k}}_{t'}|$ is given in Equation (1.30) [see Section 3.1.1.1 for further comments]. These energy bands are depicted in Figure 3.3(b) and (c) for two typical cases. We postpone their discussion to Section 3.1.3.3, where we analyze the quasi-particle spectra of the antiferromagnetic phase as a function of the hopping anisotropy t'/t. The corresponding normalized eigenvectors are, given that

$$\begin{aligned} \frac{U\Delta}{\sqrt{U^2\Delta^2 + 4|\gamma^{\boldsymbol{k}}_{t'}|^2}} &= \cos\theta, \\ \frac{2|\gamma^{\boldsymbol{k}}_{t'}|}{\sqrt{U^2\Delta^2 + 4|\gamma^{\boldsymbol{k}}_{t'}|^2}} &= \sin\theta \end{aligned} \tag{3.13}$$

with $\theta \in [0, \pi]$ and $\exp(i\phi_\gamma^{\boldsymbol{k}}) = \gamma_{t'}^{\boldsymbol{k}}/|\gamma_{t'}^{\boldsymbol{k}}|$,

$$\psi_1^{\boldsymbol{k}} = \begin{pmatrix} 0 \\ 0 \\ \sin(\frac{\theta}{2}) \exp(i\phi_\gamma^{\boldsymbol{k}}) \\ -\cos(\frac{\theta}{2}) \end{pmatrix}, \psi_2^{\boldsymbol{k}} = \begin{pmatrix} \cos(\frac{\theta}{2}) \exp(i\phi_\gamma^{\boldsymbol{k}}) \\ -\sin(\frac{\theta}{2}) \\ 0 \\ 0 \end{pmatrix},$$
$$\psi_3^{\boldsymbol{k}} = \begin{pmatrix} 0 \\ 0 \\ \cos(\frac{\theta}{2}) \exp(i\phi_\gamma^{\boldsymbol{k}}) \\ \sin(\frac{\theta}{2}) \end{pmatrix}, \psi_4^{\boldsymbol{k}} = \begin{pmatrix} \sin(\frac{\theta}{2}) \exp(i\phi_\gamma^{\boldsymbol{k}}) \\ \cos(\frac{\theta}{2}) \\ 0 \\ 0 \end{pmatrix}. \tag{3.14}$$

The first two eigenstates correspond to the negative eigenvalue in Equation (3.12), while the other two correspond to the positive one.

It is interesting to note how the eigenenergies (3.12) are capable of describing the opening of three sorts of energy gaps, hence three kinds of phase transitions. Both terms in the square root are nonnegative. When $U\Delta = 0$, the band gap exists if $t' > 2t$, as mentioned before, in which case the system assumes a band-insulating phase. This phase transition has to do with the change of the topological properties of the band structure, i.e. the existence and the non-existence of the Dirac points.

On the other hand, when $U\Delta \neq 0$, a gap opens due to interactions, and the system is in the Mott-insulating phase. Because this gap in the energy spectrum is intimately related to the antiferromagnetic order parameter Δ, the Mott transition, on the mean-field level, is accompanied by a simultaneous formation of antiferromagnetic ordering. In order to describe a possible Mott-insulator with no spin ordering that has been unveiled in recent quantum Monte Carlo (QMC) calculations [73], methods beyond a simple-minded mean-field approximation are required. Such a paramagnetic Mott-insulator is called a symmetric spin-liquid phase [65], the emergence of which in the case of the anisotropic honeycomb lattice is discussed in detail in the coming chapter.

3.1.1.1 Formal absence of the geometric changes

As discussed in Section 2.2, in realizing the anisotropic hopping amplitudes in an optical lattice, one may choose to change one of the electric field amplitudes with respect to the others. The consequences of this change include a series of geometric and local potential form changes [see Section 2.2 for detail]. While the latter changes are contained entirely in the expressions for the hopping amplitudes (2.39), the geometric changes make their appearances in the nearest-neighbor vectors (2.25) in the form of ζ, which is defined in Equation (2.21), and which appears directly in the structure factor

$$\begin{aligned}\gamma_{t'}^{\boldsymbol{k}} &= t' e^{i\boldsymbol{c}_1'\cdot\boldsymbol{k}} + t\left(e^{i\boldsymbol{c}_2'\cdot\boldsymbol{k}} + e^{i\boldsymbol{c}_3'\cdot\boldsymbol{k}}\right) \\ &= t' \exp\left(i3\zeta a k_y\right) + 2t \exp\left(-i\frac{3(1-2\zeta a k_y)}{2}\right)\cos\frac{\sqrt{3}ak_x}{2}, \end{aligned} \tag{3.15}$$

where a is the lattice constant and $\boldsymbol{k}$ is the crystal momentum with components k_x and k_y. However, if one tries to calculate the noninteracting tight-binding band structure $\pm|\gamma_{t'}^{\boldsymbol{k}}|$ using the above expression, one sees that ζ, which champions the geometric changes here, is absent. The resulting expression is exactly the same as Equation (1.30), namely

$$|\gamma_{t'}^{\boldsymbol{k}}| = \sqrt{t'^2 + 4t^2\cos^2 x + 4tt'\cos x\cos y} \tag{3.16}$$

in the rescaled coordinate system of $x = \frac{\sqrt{3}ak_x}{2}$ and $y = \frac{3ak_y}{2}$. This expression is calculated based on the assumption that the only changes are the hopping amplitudes.

3.1.2 Gap equation

The gap equation is obtained by evaluating the order parameter Δ:

$$\Delta = \langle n^A_{i\uparrow} - n^A_{i\downarrow} \rangle = \frac{\mathrm{Tr}\{\exp\left(-\beta \mathcal{H}^{\Delta}\right)(n^A_{i\uparrow} - n^A_{i\downarrow})\}}{\mathrm{Tr}\{\exp\left(-\beta \mathcal{H}^{\Delta}\right)\}} \tag{3.17}$$

with

$$\mathrm{Tr}\{\cdots\} \equiv \sum_l \langle l| \cdots |l\rangle \tag{3.18}$$

being the trace over a set of complete states $\{|l\rangle\}$.

Using the diagonalization results in the previous section, the gap equation is

$$\sum_{\boldsymbol{k}} \frac{1}{\sqrt{U^2\Delta^2 + 4|\gamma^{\boldsymbol{k}}_{t'}|^2}} \tanh\left(\frac{\beta}{4}\sqrt{U^2\Delta^2 + 4|\gamma^{\boldsymbol{k}}_{t'}|^2}\right) = \frac{N_{\mathrm{c}}}{U}, \tag{3.19}$$

With the help of the continuum limit approximation results obtained in Section (1.1.3), the above equation in the continuum and 0-T limits becomes

$$\int_{\diamond} \frac{dxdy}{2\pi^2} \frac{U}{\sqrt{U^2\Delta^2 + 4|\gamma^{\boldsymbol{k}}_{t'}|^2}} = 1. \tag{3.20}$$

Here $\int_{\diamond}$ means integration over the FBZ. Equation (3.20) is to be used to calculate the order parameter for each set of parameter values. The critical value of U is obtained by setting $\Delta = 0$ in Equation (3.20):

$$U_{\mathrm{c}} = \left(\int_{\diamond} \frac{dxdy}{2\pi^2} \frac{1}{2|\gamma^{\boldsymbol{k}}_{t'}|}\right)^{-1}. \tag{3.21}$$

3.1.2.1 Square lattice

Equation (3.21) is applicable to any bipartite lattice. In the case of the square lattice, for example, the appropriate expression for $\gamma^{\boldsymbol{k}}$ is

$$\gamma^{\boldsymbol{k}} = 2(\cos ak_x + \cos ak_y), \tag{3.22}$$

with a being the lattice constant. The zeros of γ are on the curves defined by the relation

$$k_x \pm k_y = \pm\frac{\pi}{a}. \tag{3.23}$$

The integrand on the right-hand-side of Equation (3.21) diverges on these curves, which are one-dimensional objects, thus yielding a vanishing critical U. In other words, the square lattice acquires antiferromagnetic ordering at infinitesimal interaction strength.

This is to be contrasted to the honeycomb lattice, in which case $\gamma^{\boldsymbol{k}}$ goes to zero linearly at the isolated Dirac points, which are zero-dimensional objects, as discussed in Section (1.2.1). This is exactly canceled by the linearly vanishing Jacobian in the polar coordinates. So in the honeycomb lattice, the integration does not diverge, so that the critical U is finite as presented in the next setion.

3.1.3 Results and discussion

The phase diagram obtained from Equation (3.21) is plotted in Figure 3.1. It consists of three phases: the semi-metallic (SM), the band-insulating (BI) and the antiferromagnetic phases (AF and AF$'$). In the next few sections, we discuss the phase diagram (3.1) in detail.

3.1.3.1 SM-AF transition

One of the first things that one notices from Figure 3.1 is that U_c/t varies roughly linearly for t'/t close to 1, before one observes a kink at $t' = 2t$ where the topological transition from a semi-metal to a band-insulator occurs in the weakly-

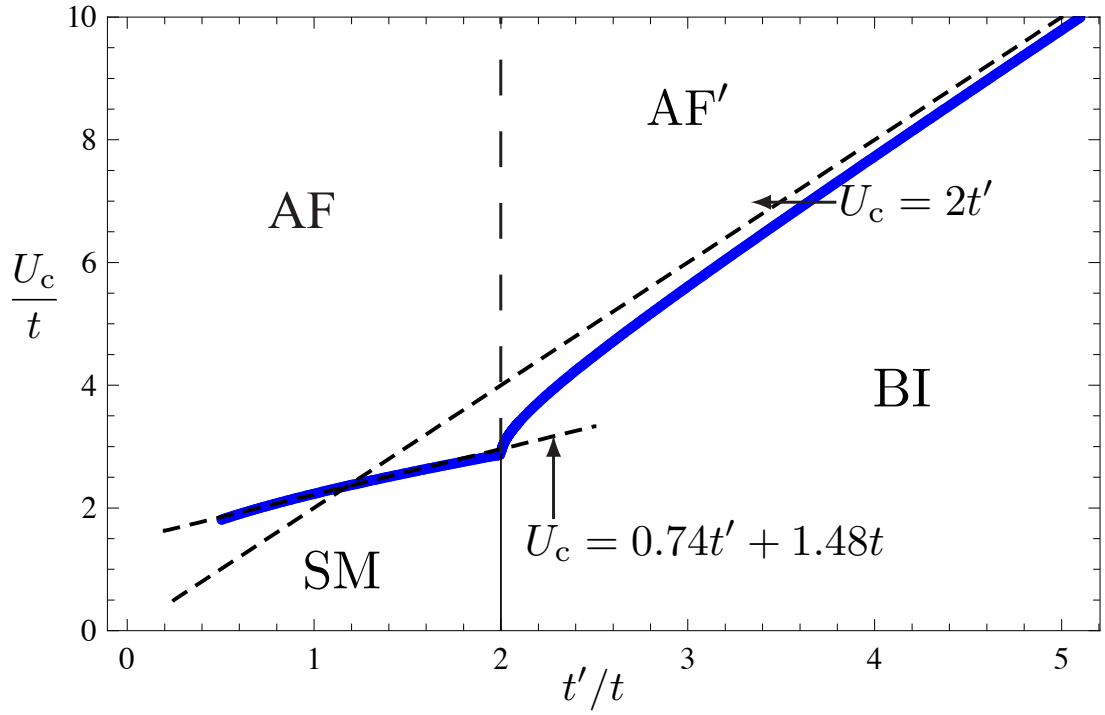

Figure 3.1: The mean-field phase diagram. The three phases are semi-metallic (SM), band-insulating (BI) and antiferromagnetic phases (AF and AF′). The SM and BI phases, as well as the AF and AF′ phases, are separated by the topological phase transition at $t' = 2t$ discussed previously. The transition line between the SM and the AF phases, as well as that separating the BI and the AF′ phases, can be approximately described by the two linear functions as indicated in the plot. These are to be explained by the arguments presented in the text.

interacting limit. This feature may be understood if one realizes that the interaction needs to overcome the total band width in order to align the spins. Thus as the total band width increases, the critical interaction strength must also increase. As mentioned previously, the antiferromagnetic transition occurs at $U_c \approx 2.23t$ in the isotropic honeycomb lattice with $t' = t$, for which case the bandwidth is given by $W = 6t$, and the critical value of U for the transition can be expressed in terms of W as

$$U_c \approx 0.37W. \tag{3.24}$$

On the other hand, in the anisotropic honeycomb lattice, the bandwidth is given by $W = 2(2t + t')$. Assuming scaling invariance of the above ratio, one would expect the relation

$$U_{\mathrm{c}} = 0.74t' + 1.48t \tag{3.25}$$

around $t' = t$. We have plotted this line in the phase diagram, and one notices that this scaling relation describes the transition line to great accuracy.

Note that our discussion here excludes the part of the phase space where $t' \ll t$, in which limit the 1D chain structure dominates. A treatment taking into account the Luttinger-liquid-behavior of the particles would be appropriate, but is beyond the scope of the current discussion.

3.1.3.2 BI-AF transition

From the energy eigenvalues (3.12) we see that, in the large-$\{U, t'\}$ limit, the AF Mott gap

$$\Delta_{\mathrm{M}} = \frac{U\Delta}{2} \tag{3.26}$$

competes with the band gap

$$\Delta_{\mathrm{BI}} = t' - 2t \tag{3.27}$$

at the M point where the Dirac points have merged. An expansion of the dispersion relation (3.12) at the M point yields

$$E^{\boldsymbol{k}_{\mathrm{M}}}_{\lambda=\pm} = \lambda \left[\sqrt{\Delta^2_{\mathrm{M}} + \Delta^2_{\mathrm{BI}}} + \mathcal{O}(|\boldsymbol{k}_{\mathrm{M}}|^2) \right], \tag{3.28}$$

where $\boldsymbol{k}_{\mathrm{M}}$ is the wave vector measured from the M point. Assume that the larger of these two gaps determines the state of the system, the transition point is obtained by solving

$$\Delta_{\mathrm{M}} = \Delta_{\mathrm{BI}}, \tag{3.29}$$

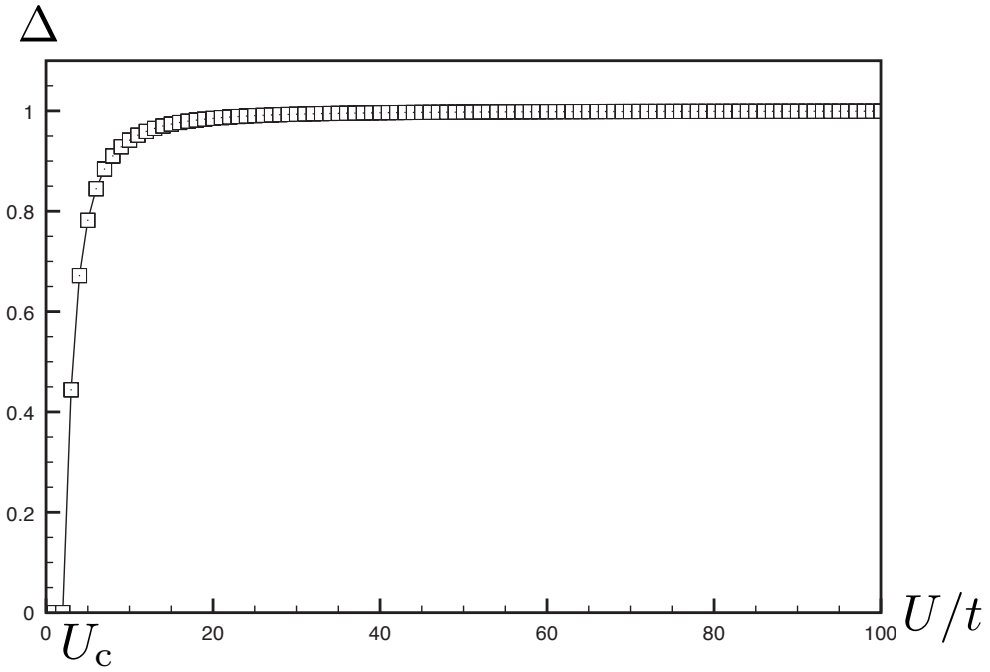

Figure 3.2: The order parameter as a function of U for the case $t' = t$. The transition point where Δ turns nonzero is at $U_c \simeq 2.23t$.

which yields (with $\Delta = 1$)

$$U_c = 2(t' - 2t) \approx 2t', \text{ if } t' \gg t \tag{3.30}$$

in the large-$\{U, t'\}$ limit. The phase diagram (3.1) shows indeed that this is the asymptotic value of the BI-AF transition line when $t' \gg 2t$.

3.1.3.3 Order parameter

Finally, we investigate how the order parameter changes with the model parameters. In Figure 3.2, the order parameter is plotted against U, for the particular case of $t' = t$. The critical point is where the order parameter turns nonzero, which is at $U_c \simeq 2.23t$ for this particular case, agreeing with previous results [22]. After that, the order parameter steadily increases, and approaches 1 in the limit $U \to \infty$.

In Figure 3.3, the order parameter is plotted against t', for the case $U = 5t$. The point of this plot is to investigate if a mark is left on the order parameter by the opening of a band gap at $t' = 2t$. As far as this plot goes, no such mark is observed. The transition from the AF to the BI phase is marked by the vanishing of the order parameter, which happens at $\sim 2.7t$ in this particular plot, as also suggested by Figure 3.1.

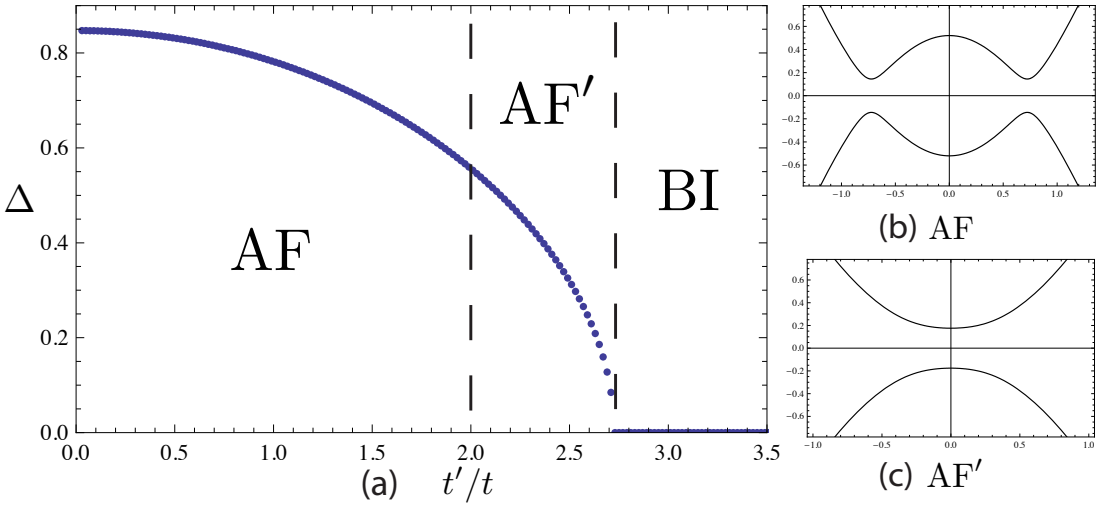

Figure 3.3: (a): The AF order parameter Δ as a function of t' for the case $U = 5t$. The point $\Delta = 0$ separates the BI and the antiferromagnetic phases, the latter of which is subdivided into the AF and the AF$'$ phases by the line $t' = 2t$. The difference between the AF and the AF$'$ phases is in their band structure (with merged/distinct minima), as may be seen in (b) for AF and (c) for AF$'$. Here we plotted the band structures obtained from Equation (3.12) along the one side of the hexagonal FBZ as depicted in Figure 1.1(b).

AF and AF$'$ phases The phase diagram 3.1 suggests that the AF and AF$'$ phases are the same thermodynamic phase. The difference between the AF and the AF$'$ phases stems from their excitation spectra, which are depicted in Figures 3.3(b) and (c).

In the AF phase, one has $t' < 2t$, in which case the system evolves from a semi-metal in the weakly-interacting limit, which features the massless Dirac points, to a Mott insulator with massive Dirac points in the strongly-interacting limit.

The Berry phases of the Dirac points in both cases are π and $-\pi$. The Mott gap opens at the position where the two inequivalent Dirac points are located in the semi-metallic phase, which are related to each other by time-reversal-symmetry. This is illustrated in Figure 3.3(b).

On the other hand, in the AF$'$ phase, one has $t' > 2t$, and the system evolves from a band-insulator with a band gap at the M point in the FBZ to a Mott insulator in the strongly-interacting limit. The Mott gap opens on top of the band gap at the M point. There is thus only one type of quasi-particles in the excitation spectrum, with a time-reversal-invariant momentum and a Berry phase of 0. This case is illustrated in Figure 3.3(c).

Thus in experiments probing the low energy excitation spectrum of the system, using, e.g., angle-resolved photoemission spectroscopy, two quasi-particle peaks are expected to be observed in the AF phase, which are related to each other by time-reversal symmetry, whereas only one can be observed in the AF$'$ phase. Notice that there have recently been proposals to adapt the condensed-matter technique of angle-resolved photoemission spectroscopy to cold atoms, in the framework of angle-resolved Raman spectroscopy [82, 83].

3.2 Stoner's criterion

In the previous section, we have investigated the antiferromagnetic phase transition from the strongly-correlated side, i.e. we have assumed the antiferromagnetic order to be the ground state in the large-U limit, and the transition is then determined from the vanishing of the order parameter in the gap equation (3.20). Alternatively, one may approach the transition line from the weakly-interacting side, which also serves as a way to check the consistency of the previous mean-field results. In this approach, one searches for the instabilities of the noninteracting paramagnetic ground state $|\Omega\rangle$ [84], which describes both the semi-metallic and the band-insulating phase. Stoner's criterion states that such instabilities may be identified with the poles of the zero-frequency susceptibilities corresponding to the ordered state – in the present case, to the antiferromagnetic phase. At its poles,

the susceptibility, which measures the response of the system to an external magnetic field, is infinite, which signifies a spontaneous instability. Zero-frequency is required so that the external field is static, and thus there is no external energy input. Both the divergence and the zero-frequency of the susceptibility are required by the phase transition to be spontaneous. One is therefore led to examine the transverse magnetic susceptibility $\chi(\mathbf{q},\omega)$, which measures the response of the system in the form of spin-flipping to an external magnetic field.

3.2.1 Weakly-interacting limit

The transverse magnetic susceptibility is calculated in the weakly-interacting limit, in which the natural basis is the eigen-basis of $\mathcal{H}_0$ in Equation (1.14), as shown in Equation (1.18). The creation operators in this basis are

$$\psi_{\lambda\sigma}^{\boldsymbol{k}\dagger} = \frac{1}{\sqrt{2}}(a_{\boldsymbol{k}\sigma}^{\dagger} + \lambda e^{-i\theta_\gamma^{\boldsymbol{k}}} b_{\boldsymbol{k}\sigma}^{\dagger}) \tag{3.31}$$

such that

$$\mathcal{H}_0 = \sum_{\boldsymbol{k}\lambda\sigma} \epsilon_\lambda^{\boldsymbol{k}} \psi_{\lambda\sigma}^{\boldsymbol{k}\dagger} \psi_{\lambda\sigma}^{\boldsymbol{k}}, \tag{3.32}$$

where $\epsilon_\lambda^{\boldsymbol{k}}$ is as shown in Equation (1.17). As before, $\lambda = \pm$ is the band index. In the same basis, we rewrite $\mathcal{V}$ in Equation (3.3) as

$$\mathcal{V} = \frac{U}{2N_\mathrm{c}} \sum_{\boldsymbol{k}\boldsymbol{k}'\boldsymbol{l}} \sum_{\{\lambda_j\}} g_\lambda(\boldsymbol{k},\boldsymbol{k}',\boldsymbol{l}) \psi_{\lambda_1\uparrow}^{\boldsymbol{k}+\boldsymbol{l}\dagger} \psi_{\lambda_2\uparrow}^{\boldsymbol{k}} \psi_{\lambda_3\downarrow}^{\boldsymbol{k}'-\boldsymbol{l}\dagger} \psi_{\lambda_4\downarrow}^{\boldsymbol{k}'} - \frac{U}{2} \sum_{\boldsymbol{k}\lambda\sigma} \psi_{\lambda\sigma}^{\boldsymbol{k}\dagger} \psi_{\lambda\sigma}^{\boldsymbol{k}}, \tag{3.33}$$

where

$$g_\lambda(\boldsymbol{k},\boldsymbol{k}',\boldsymbol{l}) = \frac{1}{2}\left\{1 + \lambda e^{i[\theta_\gamma(\boldsymbol{k},\boldsymbol{l}) + \theta_\gamma(\boldsymbol{k}',-\boldsymbol{l})]}\right\}, \tag{3.34}$$

with $\lambda = \prod_{j=1}^{4} \lambda_j$, and where

$$\theta_\gamma(\boldsymbol{k}, \boldsymbol{l}) = \theta_\gamma^{\boldsymbol{k}+\boldsymbol{l}} - \theta_\gamma^{\boldsymbol{k}} \tag{3.35}$$

is the difference between the phase angles $\theta_\gamma^{\boldsymbol{k}+\boldsymbol{l}}$ and $\theta_\gamma^{\boldsymbol{k}}$, which are defined in Equation (1.18).

3.2.2 Susceptibility

The transverse magnetic susceptibility is defined in the retarded form as

$$\chi(\boldsymbol{q}, \omega) = i \int d\tau \Theta(\tau) e^{i(\omega + i0^+)\tau} \langle [S^{\mathrm{L}}(\boldsymbol{q}, \tau), S^{\mathrm{R}}(\boldsymbol{r} = 0, \tau = 0)] \rangle, \tag{3.36}$$

where τ is the imaginary time, and

$$\Theta(\tau) = \begin{cases} 1 \text{ if } \tau > 0 \\ \frac{1}{2} \text{ if } \tau = 0 \\ 0 \text{ if } \tau < 0 \end{cases} \tag{3.37}$$

is the Heaviside theta function. The definition of the susceptibility requires the spin density operator, which in momentum space is given by

$$\tilde{S}^{\mu}(\boldsymbol{q}) = \sum_{\boldsymbol{p}\lambda\lambda'} h^{\lambda\lambda'}(\boldsymbol{p}, \boldsymbol{q}) \sum_{\sigma\sigma'} \tilde{\psi}^{\boldsymbol{p}+\boldsymbol{q}\dagger}_{\lambda\sigma} \frac{\tau^{\mu}_{\sigma\sigma'}}{2} \tilde{\psi}^{\boldsymbol{p}}_{\lambda'\sigma'}, \tag{3.38}$$

where

$$h^{\lambda\lambda'}(\boldsymbol{p}, \boldsymbol{q}) = \phi^{\dagger}_{\lambda \boldsymbol{p}+\boldsymbol{q}} \phi_{\lambda' \boldsymbol{p}} = \frac{1}{2} \left[1 + \lambda\lambda' \exp i \left(\theta_{\gamma'}^{\boldsymbol{p}+\boldsymbol{q}} - \theta_{\gamma'}^{\boldsymbol{p}} \right) \right] \tag{3.39}$$

is the overlapping of wave functions, τ^{μ} are the Pauli matrices

$$\tau^x = \begin{pmatrix} 0 & 1 \\ 1 & 0 \end{pmatrix}, \ \tau^y = \begin{pmatrix} 0 & -i \\ i & 0 \end{pmatrix}, \ \tau^z = \begin{pmatrix} 1 & 0 \\ 0 & -1 \end{pmatrix}. \tag{3.40}$$

Notice that the tilde sign signals the Heisenberg time dependence according to $\tilde{S} = e^{\mathcal{H}\tau} S e^{-\mathcal{H}\tau}$. The spin-raising and -lowering operators are then given by

$$\begin{aligned} \tilde{S}^{\mathrm{R}}(\boldsymbol{q}) &= \tilde{S}^{x}(\boldsymbol{q}) + i\tilde{S}^{y}(\boldsymbol{q}) = \sum_{\boldsymbol{p}\lambda\lambda'} h^{\lambda\lambda'}(\boldsymbol{p},\boldsymbol{q}) \tilde{\psi}^{\boldsymbol{p}+\boldsymbol{q}\dagger}_{\lambda\uparrow} \tilde{\psi}^{\boldsymbol{p}}_{\lambda'\downarrow}, \\ \tilde{S}^{\mathrm{L}}(\boldsymbol{q}) &= \tilde{S}^{x}(\boldsymbol{q}) - i\tilde{S}^{y}(\boldsymbol{q}) = \sum_{\boldsymbol{p}\lambda\lambda'} h^{\lambda\lambda'}(\boldsymbol{p},\boldsymbol{q}) \tilde{\psi}^{\boldsymbol{p}+\boldsymbol{q}\dagger}_{\lambda\downarrow} \tilde{\psi}^{\boldsymbol{p}}_{\lambda'\uparrow}. \end{aligned} \tag{3.41}$$

The Fourier transform between the coordinate- and momentum-space is

$$\tilde{S}^{\mathrm{R}}(\boldsymbol{r}) = \sum_{\boldsymbol{q}} e^{i\boldsymbol{q}\cdot\boldsymbol{r}} \tilde{S}^{\mathrm{R}}(\boldsymbol{q}). \tag{3.42}$$

With these quantities defined, the transverse susceptibility in coordinate space is written as

$$\tilde{\chi}(\boldsymbol{r}) = \sum_{\boldsymbol{q}} e^{i\boldsymbol{q}\cdot\boldsymbol{r}} \sum_{\boldsymbol{p}} \tilde{\chi}(\boldsymbol{p},\boldsymbol{q}), \tag{3.43}$$

where

$$\tilde{\chi}(\boldsymbol{p},\boldsymbol{q}) = \sum_{\lambda\lambda'} \tilde{\chi}_{\lambda\lambda'}(\boldsymbol{p},\boldsymbol{q}) \tag{3.44}$$

with

$$\tilde{\chi}_{\lambda\lambda'}(\boldsymbol{p},\boldsymbol{q}) = i\Theta(t) h^{\lambda\lambda'}(\boldsymbol{p},\boldsymbol{q}) \langle [\tilde{\psi}^{\boldsymbol{p}+\boldsymbol{q}\dagger}_{\lambda\downarrow}(t) \tilde{\psi}^{\boldsymbol{p}}_{\lambda'\uparrow}(t), \tilde{S}^{\mathrm{R}}(\boldsymbol{r}=0,\tau=0)] \rangle. \tag{3.45}$$

As discussed at the beginning of this section, Stoner's criterion dictates that magnetic instabilities occur at the poles of the $\chi(\boldsymbol{q},\omega=0)$ [85] in the momentum-frequency space.

To get the explicit expression for the susceptibility (3.43), we set up its equation of motion using the Heisenberg equation of motion in imaginary time

$$\partial_\tau \tilde{\mathcal{O}} = -[\tilde{\mathcal{O}}, \mathcal{H}], \tag{3.46}$$

and apply the generalized Hartree-Fock approximation

$$\psi^{\boldsymbol{p}\dagger}_{\lambda\sigma}\psi^{\boldsymbol{p}}_{\lambda\sigma} \to n_\sigma(\epsilon^{\boldsymbol{p}}_\lambda) = \langle \psi^{\boldsymbol{p}\dagger}_{\lambda\sigma}\psi^{\boldsymbol{p}}_{\lambda\sigma}\rangle \tag{3.47}$$

to reduce the order in the fermionic operators. After evaluating all the commutators, the resulting equation can be summarized as

$$\begin{aligned} &\frac{\partial}{\partial\tau}\tilde{\chi}_{\lambda\lambda'}(\boldsymbol{p},\boldsymbol{q}) \\ = \; &-\left\{\left(\epsilon^{\boldsymbol{p}}_{\lambda'} - \epsilon^{\boldsymbol{p}+\boldsymbol{q}}_{\lambda}\right) + \frac{U}{2N_{\mathrm{c}}}\sum_{\boldsymbol{k}\eta}\left[n_\downarrow(\epsilon^{\boldsymbol{k}}_\eta) - n_\uparrow(\epsilon^{\boldsymbol{k}}_\eta)\right]\right\}\tilde{\chi}_{\lambda\lambda'}(\boldsymbol{p},\boldsymbol{q}) - \left[n_\uparrow(\epsilon^{\boldsymbol{p}}_{\lambda'}) - n_\downarrow(\epsilon^{\boldsymbol{p}+\boldsymbol{q}}_{\lambda})\right]\times \\ &\left\{\delta(t)f^{\lambda\lambda'}(\boldsymbol{p},\boldsymbol{q}) + \frac{U}{2N_{\mathrm{c}}}\left[f^{\lambda\lambda'}(\boldsymbol{p},\boldsymbol{q})\tilde{\chi}(\boldsymbol{q}) - \frac{i}{2}\sin\left(\theta^{\boldsymbol{p}+\boldsymbol{q}}_{\gamma'} - \theta^{\boldsymbol{p}}_{\gamma'}\right)\tilde{\Delta}(\boldsymbol{q})\right]\right\}, \end{aligned} \tag{3.48}$$

where

$$n_\sigma(\epsilon^{\boldsymbol{p}}_\lambda) = \langle \psi^{\boldsymbol{p}\dagger}_{\lambda\sigma}\psi^{\boldsymbol{p}}_{\lambda\sigma}\rangle = \left[1 + \exp\left(\beta\epsilon^{\boldsymbol{p}}_\lambda\right)\right]^{-1}, \tag{3.49}$$

$$f^{\lambda\lambda'}(\boldsymbol{p},\boldsymbol{q}) = h^{\lambda\lambda'}(\boldsymbol{p},\boldsymbol{q})h^{\lambda'\lambda}(\boldsymbol{p}+\boldsymbol{q},-\boldsymbol{q}) = \frac{1}{2}[1 + \lambda\lambda'\cos(\theta^{\boldsymbol{p}+\boldsymbol{q}}_{\gamma'} - \theta^{\boldsymbol{p}}_{\gamma'})], \tag{3.50}$$

$$\tilde{\chi}(\boldsymbol{q}) = \sum_{\boldsymbol{k}}\tilde{\chi}(\boldsymbol{k},\boldsymbol{q}) \tag{3.51}$$

with $\tilde{\chi}(\boldsymbol{k},\boldsymbol{q})$ being defined in Equation (3.44), and

$$\tilde{\Delta}(\boldsymbol{q}) = i\Theta(\tau)\sum_{\boldsymbol{p}\eta\eta'} h^{-\eta\eta'}(\boldsymbol{p},\boldsymbol{q})\langle[\tilde{\psi}^{\boldsymbol{p}+\boldsymbol{q}\dagger}_{\lambda\downarrow}\tilde{\psi}^{\boldsymbol{p}}_{\lambda'\uparrow}, \tilde{S}^{\mathrm{R}}(\boldsymbol{r}=0,\tau=0)]\rangle \tag{3.52}$$

with

$$h^{-\lambda\lambda'}(\boldsymbol{p},\boldsymbol{q}) = \frac{1}{2}[1-\lambda\lambda' \exp i(\theta_{\gamma'}^{\boldsymbol{p}+\boldsymbol{q}} - \theta_{\gamma'}^{\boldsymbol{p}})]. \tag{3.53}$$

Here $\beta = \frac{1}{k_B T}$ with k_B and T being the Boltzmann constant and the absolute temperature, respectively.

Applying Fourier transformation to the both sides of the Equation (3.48), we obtain

$$\chi_{\lambda\lambda'}(\boldsymbol{q};\omega) \;=\; \chi^0_{\lambda\lambda'}(\boldsymbol{q};\omega)[1+U\tilde{\chi}(\boldsymbol{q};\omega)] + iUC_{\lambda\lambda'}(\boldsymbol{q};\omega)\Delta(\boldsymbol{q};\omega), \tag{3.54}$$

where

$$\chi^0_{\eta\eta'}(\boldsymbol{q};\omega) = A_{\eta\eta'}(\boldsymbol{q};\omega) + B_{\eta\eta'}(\boldsymbol{q};\omega) \tag{3.55}$$

with

$$A_{\eta\eta'}(\boldsymbol{q};\omega) = \frac{1}{2N_{\rm c}}\sum_{\boldsymbol{p}} m_{\eta\eta'}(\boldsymbol{p},\boldsymbol{q};\omega), \tag{3.56}$$

$$B_{\eta\eta'}(\boldsymbol{q};\omega) = \frac{1}{2N_{\rm c}}\sum_{\boldsymbol{p}} \eta\eta' \cos\left(\theta_{\gamma'}^{\boldsymbol{p}+\boldsymbol{q}} - \theta_{\gamma'}^{\boldsymbol{p}}\right) m_{\eta\eta'}(\boldsymbol{p},\boldsymbol{q};\omega), \tag{3.57}$$

$$m_{\eta\eta'}(\boldsymbol{p},\boldsymbol{q};\omega) = \frac{n_\uparrow(\epsilon_{\eta'}^{\boldsymbol{p}}) - n_\downarrow(\epsilon_{\eta}^{\boldsymbol{p}+\boldsymbol{q}})}{\omega - (\epsilon_{\eta'}^{\boldsymbol{p}} - \epsilon_{\eta}^{\boldsymbol{p}+\boldsymbol{q}}) - \frac{U}{N_{\rm c}}\sum_{\boldsymbol{k}\lambda}[n_\downarrow(\epsilon_\lambda^{\boldsymbol{k}}) - n_\uparrow(\epsilon_\lambda^{\boldsymbol{k}})] + i0^+}, \tag{3.58}$$

and

$$C_{\eta\eta'}(\boldsymbol{q};\omega) = \frac{1}{2N_{\rm c}}\sum_{\boldsymbol{p}} \eta\eta' \sin\left(\theta_{\gamma'}^{\boldsymbol{p}+\boldsymbol{q}} - \theta_{\gamma'}^{\boldsymbol{p}}\right) m_{\eta\eta'}(\boldsymbol{p},\boldsymbol{q};\omega). \tag{3.59}$$

Summing up all components, we obtain

$$\chi(\boldsymbol{q};\omega) = \chi^0(\boldsymbol{q};\omega)[1+U\chi(\boldsymbol{q};\omega)] + iUC(\boldsymbol{q};\omega)\Delta(\boldsymbol{q};\omega), \tag{3.60}$$

where

$$\chi^0(\boldsymbol{q};\omega) = \sum_{\lambda\lambda'} \chi^0_{\lambda\lambda'}(\boldsymbol{q};\omega), \tag{3.61}$$

$$C(\boldsymbol{q};\omega) = \sum_{\lambda\lambda'} C_{\lambda\lambda'}(\boldsymbol{q};\omega). \tag{3.62}$$

Now we define

$$\tilde{\Phi}(\boldsymbol{q}) = i\Theta(\tau) \sum_{\boldsymbol{p}\eta\eta'} \langle [\tilde{\psi}^{\boldsymbol{p}+\boldsymbol{q}\dagger}_{\eta\downarrow} \tilde{\psi}^{\boldsymbol{p}}_{\eta'\uparrow}, \tilde{S}^{\mathrm{R}}(\boldsymbol{r}=0,\tau=0)] \rangle \tag{3.63}$$

so that

$$\tilde{\Phi}(\boldsymbol{q}) = \tilde{\Delta}(\boldsymbol{q}) + \tilde{\chi}(\boldsymbol{q}). \tag{3.64}$$

Following the same method which led to Equation (3.60), we obtain

$$\Phi(\boldsymbol{q};\omega) = (A + B - iC) + U[A\Phi(\boldsymbol{q};\omega) + (B - iC)(\chi(\boldsymbol{q};\omega) - \Delta(\boldsymbol{q};\omega))], \tag{3.65}$$

where

$$A(\boldsymbol{q};\omega) = \sum_{\lambda\lambda'} A_{\lambda\lambda'}(\boldsymbol{q};\omega), \tag{3.66}$$

$$B(\boldsymbol{q};\omega) = \sum_{\lambda\lambda'} B_{\lambda\lambda'}(\boldsymbol{q};\omega). \tag{3.67}$$

Notice that A, B and C in Equation (3.65) are functions of momentum and frequency. These are left implicit for the sake of cleaner expressions.

With Equations (3.60), (3.64) and (3.65), we may solve for the susceptibility. Up to first order in U, we obtain

$$\chi(\boldsymbol{q};\omega) = \frac{\chi^0(\boldsymbol{q};\omega) - U(A^2 - B^2 - C^2)}{1 - 2UA}. \tag{3.68}$$

3.2.3 Critical equation and transition line

With the susceptibility defined in Equation (3.68), the Stoner's criterion

$$\chi(\boldsymbol{q}, \omega = 0)^{-1} = 0, \tag{3.69}$$

then yields the equation

$$2UA(\boldsymbol{q}; \omega = 0) = 1, \tag{3.70}$$

or

$$\frac{1}{N_\mathrm{c}} \sum_{\boldsymbol{p}\eta\eta'} \frac{n_\uparrow(\epsilon^{\boldsymbol{p}}_{\eta'}) - n_\downarrow(\epsilon^{\boldsymbol{p}+\boldsymbol{q}}_{\eta})}{-(\epsilon^{\boldsymbol{p}}_{\eta'} - \epsilon^{\boldsymbol{p}+\boldsymbol{q}}_{\eta}) - \frac{U}{N_\mathrm{c}} \sum_{\boldsymbol{k}\lambda} [n_\downarrow(\epsilon^{\boldsymbol{k}}_{\lambda}) - n_\uparrow(\epsilon^{\boldsymbol{k}}_{\lambda})] + i0^+} = \frac{1}{U}. \tag{3.71}$$

In the paramagnetic phase we have

$$n_\uparrow(\epsilon^{\boldsymbol{k}}_{\lambda}) = n_\downarrow(\epsilon^{\boldsymbol{k}}_{\lambda}) \equiv n(\epsilon^{\boldsymbol{k}}_{\lambda}), \tag{3.72}$$

and for half-filling at zero temperature, the occupation numbers are given by

$$n(\epsilon^{\boldsymbol{k}}_{\lambda}) = (1 - \lambda)/2. \tag{3.73}$$

We thus obtain the equation

$$N_\mathrm{c}^{-1} \sum_{\boldsymbol{p}} (|\gamma^{\boldsymbol{p}+\boldsymbol{q}}| + |\gamma^{\boldsymbol{p}}|)^{-1} = U^{-1}. \tag{3.74}$$

To obtain the critical, i.e. the smallest, value of U at which the Stoner criterion could be satisfied, we maximize the LHS of Equation (3.74) with respect to the ordering momentum $\boldsymbol{q}$. One finds that the maximum of the LHS of Equation (3.74), and hence the magnetic instability, always occurs at $\boldsymbol{q} = 0$. Notice that this position of the antiferromagnetic instability in the FBZ is different from that of the square lattice, where the the antiferromagnetic order doubles the

unit cell and thus modifies the FBZ. In the honeycomb lattice, however, the antiferromagnetic ordering respects the lattice structure, as we have mentioned above, and the instability therefore occurs at the Γ point at the center of the FBZ. The resulting equation for U_{c} is then

$$N_{\mathrm{c}}^{-1}\sum_{\boldsymbol{p}}(2|\gamma^{\boldsymbol{p}}|)^{-1} = (U_{\mathrm{c}})^{-1}\,, \tag{3.75}$$

which is identical to the mean-field self-consistent gap equation (3.21) upon taking the continuum limit. Thus the current calculation based on Stoner's criterion reproduces the exact same critical line as displayed in the phase diagram (3.1), even though the approach adopted in the current section is completely different from the mean-field self-consistent method. As mentioned at the beginning of this section, the two approaches complement each other, since they approach from the strong and weak interacting limit, respectively.

3.3 Effective Hamiltonians for the large-U limit

3.3.1 Effective model for single-occupancy

In the large-U limit, in order to avoid the huge penalty in energy caused by two particles occupying the same lattice site, each lattice site is either empty or singly occupied. At half-filling, this amounts to the Mott-insulating phase, in which there is exactly one particle per lattice site (single-occupancy). Here we derive an effective Hamiltonian for this particular limit, following the derivation of the t-J model [86, 87].

The starting point is the Hamiltonian (3.1). We define the projectors P_{SO} and P_η, where P_{SO} and P_η are the projectors for the subspace of single-occupancy and that with at least one empty site and one double-occupancy, respectively. We have

$$P_{\mathrm{SO}} + P_\eta = \mathbf{1}, \tag{3.76}$$

where **1** is the identity operator, so that

$$\mathcal{H} = \underbrace{P_{\mathrm{SO}}\mathcal{H}P_{\mathrm{SO}} + P_\eta\mathcal{H}P_\eta}_{\mathcal{H}_{\mathrm{D}}} + \underbrace{P_{\mathrm{SO}}\mathcal{H}P_\eta + P_\eta\mathcal{H}P_{\mathrm{SO}}}_{\mathcal{H}_\eta}. \tag{3.77}$$

We introduce the parameter ξ, so that

$$\mathcal{H}(\xi) = \mathcal{H}_{\mathrm{D}} + \xi\mathcal{H}_\eta. \tag{3.78}$$

Eventually ξ will be set to 1. We eliminate ξ, and hence $\mathcal{H}_\eta$, to the lowest order, with the help of the canonical transformation $e^{i\xi S}$ with $S^\dagger = S$, so that

$$\mathcal{H}_{\mathrm{eff}}(\xi) = e^{i\xi S}\mathcal{H}(\xi)e^{-i\xi S} = \mathcal{H}_{\mathrm{D}} + \mathcal{O}(\xi^2). \tag{3.79}$$

Collecting powers of ξ up to the second order, we obtain

$$\mathcal{H}_{\mathrm{eff}}(\xi) = \mathcal{H}_{\mathrm{D}} + \xi\left\{\mathcal{H}_\eta + i[S,\mathcal{H}_{\mathrm{D}}]\right\} + \xi^2\left\{i\left[S,\mathcal{H}_\eta\right] + \frac{1}{2}\left[S,[\mathcal{H}_{\mathrm{D}},S]\right]\right\} + \mathcal{O}(\xi^3). \tag{3.80}$$

The generator S is solved from

$$\mathcal{H}_\eta + i[S,\mathcal{H}_{\mathrm{D}}] = 0, \tag{3.81}$$

in order to eliminate the first-order term in ξ, from which we obtain

$$P_{\mathrm{SO}}SP_\eta = [(P_{\mathrm{SO}}\mathcal{H}P_{\mathrm{SO}})(P_{\mathrm{SO}}SP_\eta) + iP_{\mathrm{SO}}\mathcal{H}_\eta P_\eta](P_\eta\mathcal{H}P_\eta)^{-1} \tag{3.82}$$

by multiplying P_{SO} and P_η on the left and right sides of Equation (3.81), respectively. Its hermitian conjugate is naturally implied. The other components of S

can be taken as

$$\begin{aligned} P_{\mathrm{SO}} S P_{\mathrm{SO}} &\propto P_{\mathrm{SO}}, \\ P_\eta S P_\eta &\propto P_\eta \end{aligned} \tag{3.83}$$

with constant proportionality factors. Note that the hopping terms in $\mathcal{H}_0$, as shown in Equation (3.2), change the electronic configuration of a state, while $\mathcal{V}$ in Equation (3.3) does not. Furthermore, in the subspace of single-occupancy, the onsite interaction term does not contribute to the energy. Thus we have

$$P_{\mathrm{SO}} \mathcal{H} P_{\mathrm{SO}} = 0, \tag{3.84}$$

which leads to the expression

$$P_{\mathrm{SO}} S P_\eta = i P_{\mathrm{SO}} \mathcal{H}_\eta P_\eta (P_\eta \mathcal{H} P_\eta)^{-1} \approx i P_{\mathrm{SO}} \mathcal{H}_\eta P_\eta / U, \tag{3.85}$$

where we have made the approximation

$$P_\eta \mathcal{H} P_\eta \approx \langle P_\eta \mathcal{H} P_\eta \rangle \approx U. \tag{3.86}$$

The last equality in Equation (3.86) is justified if we consider the low energy sector of the large-U limit, in which there is only one doubly occupied site.

So we have

$$\begin{aligned}
\mathcal{H}_{\text{eff}}(\xi=1) &\approx \mathcal{H}_{\text{D}} + \frac{i}{2}[S, \mathcal{H}_\eta] && (3.87)\\
&= \mathcal{H}_{\text{D}} + \frac{1}{U}[P_\eta \mathcal{H} P_{\text{SO}} \mathcal{H} P_\eta - P_{\text{SO}} \mathcal{H} P_\eta \mathcal{H} P_{\text{SO}}] && (3.88)\\
&= \underbrace{P_{\text{SO}} \mathcal{H} P_{\text{SO}} - \frac{1}{U} P_{\text{SO}} \mathcal{H} P_\eta \mathcal{H} P_{\text{SO}}}_{P_{\text{SO}} \mathcal{H}_{\text{eff}} P_{\text{SO}}} && (3.89)\\
&\quad + \underbrace{P_\eta \mathcal{H} P_\eta + \frac{1}{U} P_\eta \mathcal{H} P_{\text{SO}} \mathcal{H} P_\eta}_{P_\eta \mathcal{H}_{\text{eff}} P_\eta}. && (3.90)
\end{aligned}$$

We are interested in only the subspace of single-occupancy, so we have effectively

$$\mathcal{H}_{\text{SO}} = P_{\text{SO}} \mathcal{H} P_{\text{SO}} - \frac{1}{U} P_{\text{SO}} \mathcal{H} P_\eta \mathcal{H} P_{\text{SO}}. \tag{3.91}$$

For the same reason that led to Equation (3.84), we have

$$P_{\text{SO}} \mathcal{H} P_\eta \mathcal{H} P_{\text{SO}} = P_{\text{SO}} \mathcal{H}_0 P_\eta \mathcal{H}_0 P_{\text{SO}}. \tag{3.92}$$

We consider as an example the hopping term $a^\dagger_{i\sigma} b_{j\sigma}$:

$$\begin{aligned}
a^\dagger_{i\sigma} b_{j\sigma} &= a^\dagger_{i\sigma}(1 - n^A_{i\bar\sigma} + n^A_{i\bar\sigma}) b_{j\sigma} (1 - n^B_{j\bar\sigma} + n^B_{j\bar\sigma})\\
&= \underbrace{a^\dagger_{i\sigma} n^A_{i\bar\sigma} b_{j\sigma}(1 - n^B_{j\bar\sigma})}_{(\cdot)_A \;\; (\cdot)_B \,\to\, (\cdot\cdot)_A \;\; ()_B} + \underbrace{a^\dagger_{i\sigma}(1 - n^A_{i\bar\sigma}) b_{j\sigma} n^B_{j\bar\sigma}}_{()_A \;\; (\cdot\cdot)_B \,\to\, (\cdot)_A \;\; (\cdot)_B}\\
&\quad + \underbrace{a^\dagger_{i\sigma}(1 - n^A_{i\bar\sigma}) b_{j\sigma}(1 - n^B_{j\bar\sigma})}_{()_A \;\; (\cdot)_B \,\to\, (\cdot)_A \;\; ()_B} + \underbrace{a^\dagger_{i\sigma} n^A_{i\bar\sigma} b_{j\sigma} n^B_{j\bar\sigma}}_{(\cdot)_A \;\; (\cdot\cdot)_B \,\to\, (\cdot\cdot)_A \;\; (\cdot)_B}, \qquad (3.93)
\end{aligned}$$

where $\bar\sigma$ is the spin opposite to σ. In the under braces, brackets $()_A$ $()_B$ denote a pair of nearest-neighboring lattice sites, while a dot $\cdot$ denotes a particle. Empty

brackets denote empty lattice sites. For example,

$$(\cdot)_A \;\; (\cdot)_B \;\; \rightarrow \;\; (\cdot\cdot)_A \;\; ()_B \tag{3.94}$$

represents the event in which two singly occupied lattice sites turns into a doubly occupied A-site and an empty B-site, or, in other words, a hopping event from B-site to A-site beginning from two singly-occupied lattice sites. In the final expression of the Equation (3.93), only the first term has an initial state of single-occupancy, and only the second term has a final state of single-occupancy. They are the only contributions to the two terms $P_\eta \mathcal{H}_0 P_{\mathrm{SO}}$ and $P_{\mathrm{SO}} \mathcal{H}_0 P_\eta$, respectively. The same consideration leads to similar conclusions for the term $b^\dagger_{j\sigma} a_{i\sigma}$. So we have

$$\begin{aligned} P_{\mathrm{SO}} \mathcal{H}_0 P_\eta \mathcal{H}_0 P_{\mathrm{SO}} \;=\; & \sum_{\langle ij \rangle \sigma} t_{ij}^2 \Bigg[\underbrace{b^\dagger_{j\sigma}(1-n^B_{j\bar{\sigma}}) a_{i\sigma} n^A_{i\bar{\sigma}} a^\dagger_{i\sigma} n^A_{i\bar{\sigma}} b_{j\sigma} (1-n^B_{j\bar{\sigma}})}_{\text{Hopping from } b \text{ to } a \text{ and back}} \\ & + \underbrace{a^\dagger_{i\sigma}(1-n^A_{i\bar{\sigma}}) b_{j\sigma} n^B_{j\bar{\sigma}} b^\dagger_{j\sigma} n^B_{j\bar{\sigma}} a_{i\sigma} (1-n^A_{i\bar{\sigma}})}_{\text{Hopping from } a \text{ to } b \text{ and back}} \Bigg] \end{aligned} \tag{3.95}$$

Each of the two terms in Equation (3.95) describes a virtual super-exchange process, i.e. a particle experiences a round trip of hopping back and forth between two, nearest-neighboring in this case, sites. The energy cost of this process is $\frac{4t_{ij}^2}{U}$, where the factor of 4 will become clear at the end of this section. Using the fermionic anti-commutation relation

$$\left[\alpha, \beta^\dagger\right]_+ = \delta_{\alpha\beta}, \tag{3.96}$$

we can re-write the above expressions as

$$b^{\dagger}_{j\sigma}(1-n^{B}_{j\bar{\sigma}})a_{i\sigma}n^{A}_{i\bar{\sigma}}a^{\dagger}_{i\sigma}n^{A}_{i\bar{\sigma}}b_{j\sigma}(1-n^{B}_{j\bar{\sigma}}) = (1-n^{A}_{i\sigma})n^{A}_{i\bar{\sigma}}(1-n^{B}_{j\bar{\sigma}})n^{B}_{j\sigma}, \quad (3.97)$$

$$a^{\dagger}_{i\sigma}(1-n^{A}_{i\bar{\sigma}})b_{j\sigma}n^{B}_{j\bar{\sigma}}b^{\dagger}_{j\sigma}n^{B}_{j\bar{\sigma}}a_{i\sigma}(1-n^{A}_{i\bar{\sigma}}) = (1-n^{A}_{i\bar{\sigma}})n^{A}_{i\sigma}(1-n^{B}_{j\sigma})n^{B}_{j\bar{\sigma}}. \quad (3.98)$$

Thus we have

$$P_{\mathrm{SO}}\mathcal{H}_0 P_\eta \mathcal{H}_0 P_{\mathrm{SO}} = 2\sum_{\langle ij\rangle\sigma} t^2_{ij}(1-n^{A}_{i\sigma})n^{A}_{i\bar{\sigma}}(1-n^{B}_{j\bar{\sigma}})n^{B}_{j\sigma} \quad (3.99)$$

We recast the above equation in terms of the spin operators, which are defined as

$$\boldsymbol{S}^{\alpha}_{i} = \frac{1}{2}\Psi^{\alpha\dagger}_{i}\boldsymbol{\tau}\Psi^{\alpha}_{i} \text{ with } \Psi^{\alpha\dagger}_{i} = \left(\alpha^{\dagger}_{i\uparrow}\ \alpha^{\dagger}_{i\downarrow}\right), \quad (3.100)$$

where α is the sub-lattice index, and the components of $\boldsymbol{\tau}$ are the Pauli matrices (3.40). Explicitly, we have

$$\begin{aligned} S^{\alpha x}_{i} &= \frac{1}{2}(\alpha^{\dagger}_{i\uparrow}\alpha_{i\downarrow} + \alpha^{\dagger}_{i\downarrow}\alpha_{i\uparrow}), \\ S^{\alpha y}_{i} &= \frac{i}{2}(\alpha^{\dagger}_{i\downarrow}\alpha_{i\uparrow} - \alpha^{\dagger}_{i\uparrow}\alpha_{i\downarrow}), \\ S^{\alpha z}_{i} &= \frac{1}{2}(n^{\alpha}_{i\uparrow} - n^{\alpha}_{i\downarrow}). \end{aligned} \quad (3.101)$$

Using the relation $(n^{\alpha}_{i\sigma})^2 = n^{\alpha}_{i\sigma}$, we have

$$\begin{aligned} \frac{1}{2}S^{\alpha z}_{i}(n^{\alpha}_{i\uparrow} - n^{\alpha}_{i\downarrow}) &= (S^{\alpha z}_{i})^2, \\ \frac{1}{2}S^{\alpha z}_{i}(n^{\alpha}_{i\uparrow} + n^{\alpha}_{i\downarrow}) &= \frac{1}{2}S^{\alpha z}_{i}, \end{aligned} \quad (3.102)$$

which gives us

$$\begin{aligned} S_i^{\alpha z} n_{i\uparrow}^{\alpha} &= S_i^{\alpha z}(\frac{1}{2} + S_i^{\alpha z}), \\ S_i^{\alpha z} n_{i\downarrow}^{\alpha} &= S_i^{\alpha z}(\frac{1}{2} - S_i^{\alpha z}). \end{aligned} \tag{3.103}$$

So we have

$$\begin{aligned} (1 - n_{i\downarrow}^{\alpha}) n_{i\uparrow}^{\alpha} &= (n_{i\uparrow}^{\alpha} - n_{i\downarrow}^{\alpha}) n_{i\uparrow}^{\alpha} \\ &= 2 S_i^{\alpha z} n_{i\uparrow}^{\alpha} \\ &= S_i^{\alpha z}(2 S_i^{\alpha z} + 1), \end{aligned} \tag{3.104}$$

and

$$\begin{aligned} (1 - n_{i\uparrow}^{\alpha}) n_{i\downarrow}^{\alpha} &= (n_{i\downarrow}^{\alpha} - n_{i\uparrow}^{\alpha}) n_{i\downarrow}^{\alpha} \\ &= -2 S_i^{\alpha z} n_{i\downarrow}^{\alpha} \\ &= S_i^{\alpha z}(2 S_i^{\alpha z} - 1). \end{aligned} \tag{3.105}$$

Using the above results, we obtain

$$P_{\mathrm{SO}} \mathcal{H}_0 P_\eta \mathcal{H}_0 P_{\mathrm{SO}} = 4 \sum_{\langle ij \rangle} (t_{ij})^2 \, S_i^{Az} S_j^{Bz} (4 S_i^{Az} S_j^{Bz} - 1). \tag{3.106}$$

Finally, we arrive at the effective Hamiltonian for the limit of single-occupancy

$$\mathcal{H}_{\mathrm{SO}} = - \sum_{\langle ij \rangle} \frac{4 \, (t_{ij})^2}{U} S_i^{Az} S_j^{Bz} (4 S_i^{Az} S_j^{Bz} - 1). \tag{3.107}$$

According to the definitions in Equation (3.101), the eigenvalues of $S_i^{\alpha z}$ are 0 and $\pm \frac{1}{2}$. With this knowledge, it is easy to see that the ground state energy of this

effective Hamiltonian is

$$E_{\mathrm{g}} = -\sum_{\langle ij \rangle} \frac{2\left(t_{ij}\right)^2}{U}, \tag{3.108}$$

which is achieved when

$$S_i^z S_j^z = -\frac{1}{4} \text{ for all } \langle ij \rangle. \tag{3.109}$$

Thus, in conclusion, in the limit of single occupancy, the anti-alignment of spins emerges naturally due to the $\frac{4t^2}{U}$ interaction – the so called super-exchange interaction, agreeing with our previous results that the ground state in the large-U limit is the antiferromagnetic-Mott state.

3.3.2 Effective model for the $t'/t \to \infty$ limit

As we can see in the phase diagram (3.1), the AF phase shrinks, and the critical interaction strength increases as t' increases. In order to understand this feature, in this section we derive effective Hamiltonians for the limit of large-t'.

In the large-t' limit, the dimer structure dominates the physics. So we make use of this hint, and perform our derivation in the Hilbert space spanned by the ground states of the simple-minded Hamiltonian for a dimer. The inter-dimer hopping will be taken as perturbation. Essentially what we do here is to exclude those states that do not contribute dynamically to the dimer model. The resulting Hilbert space is smaller, and the corresponding effective Hamiltonian is thus more revealing.

3.3.2.1 The limits of $t'/t \to \infty$ and $U/t' \to \infty$

The Hamiltonian in the limit where $t'/t \to \infty$ can be approximated as the sum of decoupled dimer Hamiltonians for the vertical bonds of the honeycomb lattice:

$$\mathcal{H} \approx \sum_{\text{dimers}} \mathcal{H}_{\text{dim}}, \tag{3.110}$$

where

$$\mathcal{H}_{\text{dim}} = -t' \sum_{\sigma} (a_\sigma^\dagger b_\sigma + b_\sigma^\dagger a_\sigma) + U \left[(n_\uparrow^A - \frac{1}{2})(n_\downarrow^A - \frac{1}{2}) + (n_\uparrow^B - \frac{1}{2})(n_\downarrow^B - \frac{1}{2}) \right]. \tag{3.111}$$

Within this subspace and at half-filling, we have

$$\mathbf{1} = |\uparrow,\downarrow\rangle\langle\uparrow,\downarrow| + |\uparrow\downarrow,0\rangle\langle\uparrow\downarrow,0| + |0,\uparrow\downarrow\rangle\langle 0,\uparrow\downarrow| + |\downarrow,\uparrow\rangle\langle\downarrow,\uparrow|, \tag{3.112}$$

where the spins or zero on the left and right of the comma describe the occupancy of the site in the A- and B-sublattice, respectively, whether it is a bra or a ket. This convention will also be used in the discussion that follows. The other two possible states ($|\uparrow,\uparrow\rangle$ and $|\downarrow,\downarrow\rangle$) have been omitted in Equation (3.112), because they contribute neither to the kinetic term, because hopping is not allowed thanks to the Pauli principle, nor to the interacting term, because each site is singly occupied. Because of this omission, the subspace of single-occupancy is spanned by the singlet and triplet states.

With this knowledge, we can write the dimer Hamiltonian in its matrix form

$$\mathcal{H}_{\text{dim}} = \boldsymbol{d}^\dagger M \boldsymbol{d}, \tag{3.113}$$

where

$$\boldsymbol{d}^\dagger = (|\uparrow,\downarrow\rangle, |\uparrow\downarrow,0\rangle, |0,\uparrow\downarrow\rangle, |\downarrow,\uparrow\rangle), \tag{3.114}$$

and

$$M = \begin{pmatrix} -\frac{U}{2} & -t' & -t' & 0 \\ -t' & \frac{U}{2} & 0 & t' \\ -t' & 0 & \frac{U}{2} & t' \\ 0 & t' & t' & -\frac{U}{2} \end{pmatrix}. \tag{3.115}$$

The eigenvalues and normalized eigenvectors of the above matrix are

$$\begin{aligned} E_1 &= -E_2 = -\frac{U}{2}, \\ E_3 &= -E_4 = -\sqrt{4t'^2 + \left(\frac{U}{2}\right)^2}, \end{aligned} \tag{3.116}$$

and the corresponding eigenvectors are

$$\begin{aligned} \psi_1 &= \frac{1}{\sqrt{2}} \begin{pmatrix} 1 \\ 0 \\ 0 \\ 1 \end{pmatrix}, \psi_2 = \frac{1}{\sqrt{2}} \begin{pmatrix} 0 \\ -1 \\ 1 \\ 0 \end{pmatrix}, \\ \psi_3 &= \frac{1}{2} \begin{pmatrix} \cos\frac{\theta}{2} + \sin\frac{\theta}{2} \\ \cos\frac{\theta}{2} - \sin\frac{\theta}{2} \\ \cos\frac{\theta}{2} - \sin\frac{\theta}{2} \\ -\cos\frac{\theta}{2} - \sin\frac{\theta}{2} \end{pmatrix}, \psi_4 = \frac{1}{2} \begin{pmatrix} -\cos\frac{\theta}{2} + \sin\frac{\theta}{2} \\ \cos\frac{\theta}{2} + \sin\frac{\theta}{2} \\ \cos\frac{\theta}{2} + \sin\frac{\theta}{2} \\ \cos\frac{\theta}{2} - \sin\frac{\theta}{2} \end{pmatrix}, \end{aligned} \tag{3.117}$$

where

$$\cos\theta = \frac{4t'}{\sqrt{16t'^2 + U^2}}, \sin\theta = \frac{U}{\sqrt{16t'^2 + U^2}}, \tag{3.118}$$

and $0 < \theta < \frac{\pi}{2}$.

Among the four eigenstates (3.117), ψ_1 and ψ_3 are in the low-energy sector, and are of interest to us. As long as U remains finite, $E_1 > E_3$ as can be seen from Equations (3.116), and ψ_3 is the true ground state. In the limit $U/t' \to \infty$, the two states become

$$\begin{aligned} |\psi_1\rangle &\to \frac{1}{\sqrt{2}}(|\uparrow,\downarrow\rangle + |\downarrow,\uparrow\rangle) \equiv |\mathrm{T}\rangle\text{: the triplet} \\ |\psi_3\rangle &\to \frac{1}{\sqrt{2}}(|\uparrow,\downarrow\rangle - |\downarrow,\uparrow\rangle) \equiv |\mathrm{S}\rangle\text{: the singlet,} \end{aligned} \tag{3.119a}$$

and

$$E_3 \to -\frac{U}{2} = E_1, \tag{3.120}$$

i.e. the two states become degenerate. Only in this case, it is possible to superimpose the singlet and triplet states above to form the Néel-ordered states $|\uparrow,\downarrow\rangle$ and $|\downarrow,\uparrow\rangle$, which can be identified with the antiferromagnetic ordering. One thus understands why the antiferromagnetic phase transition is shifted to larger values of U upon increase of t'/t.

3.3.2.2 Effective model for the singlet-triplet sector

As explained in the previous sections, in the limits $t'/t \to \infty$ and $U/t' \to \infty$, the singlet and triplet states are the degenerate ground states. In this section, we derive an effective Hamiltonian for the Hilbert space spanned by these states, beginning from the Hamiltonian (3.1).

We define the projector P_{ST} and P_η, with

$$\begin{aligned} P_{\mathrm{ST}} &= P_{\mathrm{T}} + P_{\mathrm{S}} && (3.121)\\ P_{\mathrm{T}} &= |\mathrm{T}\rangle\langle\mathrm{T}|, && (3.122)\\ P_{\mathrm{S}} &= |\mathrm{S}\rangle\langle\mathrm{S}|, && (3.123)\\ \mathbf{1} &= P_{\mathrm{ST}} + P_\eta, && (3.124) \end{aligned}$$

where $|\mathrm{T}\rangle$ and $|\mathrm{S}\rangle$ are the triplet and singlet states as defined in Equations (3.119), respectively, and P_η projects onto dimer states of double occupancy on one site, and vaccum on the other. As noted in the discussion following Equation (3.112), the projector P_{ST} in this Hilbert subspace for a dimer is equivalent to P_{SO} in the original Hilbert space in Section (3.3.1), because of the omission of dynamically unimportant states. Alternatively, we can write down the projectors for the Néel ordered states:

$$\begin{aligned} P_+ &= |\uparrow,\downarrow\rangle\langle\uparrow,\downarrow|,\\ P_- &= |\downarrow,\uparrow\rangle\langle\downarrow,\uparrow|. && (3.125) \end{aligned}$$

In terms of these projectors, P_{ST} is given by

$$P_{\mathrm{ST}} \;=\; P_+ + P_- \tag{3.126}$$

Following the derivation in Section 3.3.1, we get the equation

$$\mathcal{H}_{\mathrm{ST}} = P_{\mathrm{ST}}\mathcal{H}P_{\mathrm{ST}} - \frac{1}{U}P_{\mathrm{ST}}\mathcal{H}P_\eta\mathcal{H}P_{\mathrm{ST}}. \tag{3.127}$$

For the same reasons as before, the first contribution in the above equation can be omitted. The second contribution gives us

$$\begin{aligned} P_{\mathrm{ST}}\mathcal{H}P_\eta\mathcal{H}P_{\mathrm{ST}} &= P_{\mathrm{ST}}\mathcal{H}_0P_\eta\mathcal{H}_0P_{\mathrm{ST}} \\ &= \underbrace{t'^2\sum_{\langle i'j'\rangle\sigma\sigma'} P_{\mathrm{ST}}(a^\dagger_{i'\sigma}b_{j'\sigma}+\mathrm{h.c.})P_\eta(a^\dagger_{i'\sigma'}b_{j'\sigma'}+\mathrm{H.c.})P_{\mathrm{ST}}}_{\text{Intra-dimer-hopping}} \\ &\quad \underbrace{+\,t^2\sum_{\langle ij\rangle\sigma\sigma'} P_{\mathrm{ST}}(a^\dagger_{i\sigma}b_{j\sigma}+\mathrm{h.c.})P_\eta(a^\dagger_{i\sigma'}b_{j\sigma'}+\mathrm{H.c.})P_{\mathrm{ST}}}_{\text{Inter-dimer-hopping}}. \end{aligned} \tag{3.128}$$

Here $\langle i'j'\rangle$ and $\langle ij\rangle$ denote nearest-neighboring sites connected by the vectors $\boldsymbol{c}_1$ and $\boldsymbol{c}_{2,3}$, respectively. These are to be evaluated in the same fashion as Equation (3.93).

Intra-dimer-hopping terms Using Equation (3.126) to expand the intra-dimer-hopping terms in Equation (3.128), we get the following four terms.

$$
\begin{aligned}
&\sum_{\sigma\sigma'} P_+(a^\dagger_{i'\sigma}b_{j'\sigma}+\text{h.c.})P_\eta(a^\dagger_{i'\sigma'}b_{j'\sigma'}+\text{h.c.})P_+ \\
=\;& P_+\{\underbrace{a^\dagger_{i'\uparrow}(1-n^A_{i'\downarrow})b_{j'\uparrow}n^B_{j'\downarrow}b^\dagger_{j'\uparrow}a_{i'\uparrow}}_{\text{spin-}\uparrow\text{ hops from }a\text{ to }b\text{ and back}}+\underbrace{b^\dagger_{j'\downarrow}(1-n^B_{j'\uparrow})a_{i'\downarrow}n^A_{i'\uparrow}a^\dagger_{i'\downarrow}b_{j'\downarrow}}_{\text{spin-}\downarrow\text{ hops from }b\text{ to }a\text{ and back}}\}P_+ \\
=\;& 2\times P_+(1-n^A_{i'\downarrow})n^A_{i'\uparrow}(1-n^B_{j'\uparrow})n^B_{j'\downarrow}P_+. \qquad (3.129)
\end{aligned}
$$

$$
\begin{aligned}
&\sum_{\sigma\sigma'} P_-(a^\dagger_{i'\sigma}b_{j'\sigma}+\text{h.c.})P_\eta(a^\dagger_{i'\sigma'}b_{j'\sigma'}+\text{h.c.})P_- \\
=\;& P_-\{\underbrace{a^\dagger_{i'\downarrow}(1-n^A_{i'\uparrow})b_{j'\downarrow}n^B_{j'\uparrow}b^\dagger_{j'\downarrow}a_{i'\downarrow}}_{\text{spin-}\downarrow\text{ hops from }a\text{ to }b\text{ and back}}+\underbrace{b^\dagger_{j'\uparrow}(1-n^B_{j'\downarrow})a_{i'\uparrow}n^A_{i'\downarrow}a^\dagger_{i'\uparrow}b_{j'\uparrow}}_{\text{spin-}\uparrow\text{ hops from }b\text{ to }a\text{ and back}}\}P_- \\
=\;& 2\times P_-(1-n^A_{i'\uparrow})n^A_{i'\downarrow}(1-n^B_{j'\downarrow})n^B_{j'\uparrow}P_-. \qquad (3.130)
\end{aligned}
$$

$$
\begin{aligned}
&\sum_{\sigma\sigma'} P_+(a^\dagger_{i'\sigma}b_{j'\sigma}+\text{h.c.})P_\eta(a^\dagger_{i'\sigma'}b_{j'\sigma'}+\text{h.c.})P_- \\
=\;& P_+\{\underbrace{a^\dagger_{i'\uparrow}(1-n^A_{i'\downarrow})b_{j'\uparrow}n^B_{j'\downarrow}b^\dagger_{j'\downarrow}n^B_{j'\uparrow}a_{i'\downarrow}(1-n^A_{i'\uparrow})}_{\text{spin-}\downarrow\text{ hops from }a\text{ to }b\text{, spin-}\uparrow\text{ hops from }b\text{ to }a} \\
&+\underbrace{b^\dagger_{j'\downarrow}(1-n^B_{j'\uparrow})a_{i'\downarrow}n^A_{i'\uparrow}a^\dagger_{i'\uparrow}n^A_{i'\downarrow}b_{j'\uparrow}(1-n^B_{j'\downarrow})}_{\text{spin-}\uparrow\text{ hops from }b\text{ to }a\text{, spin-}\downarrow\text{ hops from }a\text{ to }b}\}P_- \\
=\;& -2\times P_+a^\dagger_{i'\uparrow}a_{i'\downarrow}(1-n^A_{i'\uparrow})n^A_{i'\downarrow}b^\dagger_{j'\downarrow}b_{j'\uparrow}(1-n^B_{j'\downarrow})n^B_{j'\uparrow}P_-. \qquad (3.131)
\end{aligned}
$$

$$
\begin{aligned}
&\sum_{\sigma\sigma'} P_-(a^\dagger_{i'\sigma}b_{j'\sigma}+\text{h.c.})P_\eta(a^\dagger_{i'\sigma'}b_{j'\sigma'}+\text{h.c.})P_+ \\
=\;& P_-\{\underbrace{a^\dagger_{i'\downarrow}(1-n^A_{i'\uparrow})b_{j'\downarrow}n^B_{j'\uparrow}b^\dagger_{j'\uparrow}n^B_{j'\downarrow}a_{i'\uparrow}(1-n^A_{i'\downarrow})}_{\text{spin-}\uparrow\text{ hops from }a\text{ to }b\text{, and spin-}\downarrow\text{ hops from }b\text{ to }a} \\
&+\underbrace{b^\dagger_{j'\uparrow}(1-n^B_{j'\downarrow})a_{i'\uparrow}n^A_{i'\downarrow}a^\dagger_{i'\downarrow}n^A_{i'\uparrow}b_{j'\downarrow}(1-n^B_{j'\uparrow})}_{\text{spin-}\downarrow\text{ hops from }b\text{ to }a\text{, and spin-}\uparrow\text{ hops from }a\text{ to }b}\}P_+ \\
=\;& -2\times P_-a^\dagger_{i'\downarrow}a_{i'\uparrow}(1-n^A_{i'\downarrow})n^A_{i'\uparrow}b^\dagger_{j'\uparrow}b_{j'\downarrow}(1-n^B_{j'\uparrow})n^B_{j'\downarrow}P_+. \qquad (3.132)
\end{aligned}
$$

The trick used in the above calculation is the same as that used in Section (3.3.1). While the former two terms describe super-exchange processes, the latter two describe spin swaps. In summary, for intra-dimer-hopping, we have

$$2t'^2 \sum_{\langle i'j'\rangle\sigma} \left\{ (1-n^A_{i'\sigma}) n^A_{i'\bar{\sigma}} (1-n^B_{j'\bar{\sigma}}) n^B_{j'\sigma} - a^\dagger_{i'\sigma} a_{i'\bar{\sigma}} (1-n^A_{i'\sigma}) n^A_{i'\bar{\sigma}} b^\dagger_{j'\bar{\sigma}} b_{j'\sigma} (1-n^B_{j'\bar{\sigma}}) n^B_{j'\sigma} \right\}. \tag{3.133}$$

Inter-dimer-hopping terms For inter-dimer-hopping, we need to look at two nearest-neighbor dimers. The projector is the tensor product of two dimer projectors:

$$\begin{aligned} P^{\otimes 2}_{\rm ST} &= (P_+ + P_-)^{\otimes 2} = P_+ \otimes P_+ + P_- \otimes P_- + P_+ \otimes P_- + P_- \otimes P_+ \\ &= |\uparrow,\downarrow;\uparrow,\downarrow\rangle\langle\uparrow,\downarrow;\uparrow,\downarrow| + |\downarrow,\uparrow;\downarrow,\uparrow\rangle\langle\downarrow,\uparrow;\downarrow,\uparrow| \\ &\quad + |\uparrow,\downarrow;\downarrow,\uparrow\rangle\langle\uparrow,\downarrow;\downarrow,\uparrow| + |\downarrow,\uparrow;\uparrow,\downarrow\rangle\langle\downarrow,\uparrow;\uparrow,\downarrow|. \end{aligned} \tag{3.134}$$

As has been mentioned, in a particular dimer, the spin on the left and right of the comma belong to sub-lattice A and B, respectively. In the above notation, dimers are separated by semicolons. Hopping events take place between the two spins on the two immediate sides of a semicolon, which are inter-dimer-nearest-neighbors in the directions $\boldsymbol{c}_{2,3}$.

The term to be considered is

$$t^2 \sum_{\langle ij\rangle\sigma\sigma'} P^{\otimes 2}_{\rm ST} (a^\dagger_{i\sigma} b_{j\sigma} + \text{H.c.}) P^{\otimes 2}_{\eta} (a^\dagger_{i\sigma'} b_{j\sigma'} + \text{h.c.}) P^{\otimes 2}_{\rm ST}. \tag{3.135}$$

Among all the terms that we obtained form expanding the above term using the expression (3.134), terms involving $P_+ \otimes P_-$ or $P_- \otimes P_+$ do not contribute, since in states such as

$$|\uparrow,\downarrow;\downarrow,\uparrow\rangle, \tag{3.136}$$

the same spin state occupies the inter-dimer nearest-neighboring sites, in which case virtual hopping between them is forbidden. Processes involving spin-swapping, such as

$$|\uparrow,\downarrow;\uparrow,\downarrow\rangle \Longrightarrow |\uparrow,\uparrow;\downarrow,\downarrow\rangle, \tag{3.137}$$

do not contribute, either. This is because the final state after spin-swapping is outside the Hilbert space under consideration, as can be seen in Equation (3.134).

In the end, nonzero contributions come from only two terms:

$$\begin{aligned}
&\sum_{\sigma\sigma'} P_+\otimes P_+(a^\dagger_{i\sigma}b_{j\sigma}+\text{h.c.})P_\eta^{\otimes 2}(a^\dagger_{i\sigma'}b_{j\sigma'}+\text{h.c.})P_+\otimes P_+\\
=\;& P_+\otimes P_+\{a^\dagger_{i\uparrow}(1-n^A_{i\downarrow})b_{j\uparrow}n^B_{j\downarrow}b^\dagger_{j\uparrow}a_{i\uparrow}+b^\dagger_{j\downarrow}(1-n^B_{j\uparrow})a_{i\downarrow}n^A_{i\uparrow}a^\dagger_{i\downarrow}b_{j\downarrow}\}P_+\otimes P_+\\
=\;& 2\times P_+\otimes P_+ n^A_{i\uparrow}(1-n^A_{i\downarrow})n^B_{j\downarrow}(1-n^B_{j\uparrow})P_+\otimes P_+
\end{aligned} \tag{3.138}$$

$$\begin{aligned}
&\sum_{\sigma\sigma'} P_-\otimes P_-(a^\dagger_{i\sigma}b_{j\sigma}+\text{h.c.})P_\eta^{\otimes 2}(a^\dagger_{i\sigma'}b_{j\sigma'}+\text{h.c.})P_-\otimes P_-\\
=\;& P_-\otimes P_-\{a^\dagger_{i\downarrow}(1-n^A_{i\uparrow})b_{j\downarrow}n^B_{j\uparrow}b^\dagger_{j\downarrow}a_{i\downarrow}+b^\dagger_{j\uparrow}(1-n^B_{j\downarrow})a_{i\uparrow}n^A_{i\downarrow}a^\dagger_{i\uparrow}b_{j\uparrow}\}P_-\otimes P_-\\
=\;& 2\times P_-\otimes P_- n^A_{i\downarrow}(1-n^A_{i\uparrow})n^B_{j\uparrow}(1-n^B_{j\downarrow})P_-\otimes P_-
\end{aligned} \tag{3.139}$$

In summary, for inter-dimer-hopping, we have

$$2t^2\times\sum_{\langle ij\rangle\sigma} n^A_{i\sigma}\left(1-n^A_{i\bar{\sigma}}\right)n^B_{j\bar{\sigma}}\left(1-n^B_{j\sigma}\right). \tag{3.140}$$

The effective Hamiltonian Finally, the effective Hamiltonian for the singlet-triplet sector is obtained by combining the terms in Equations (3.133) and (3.140):

$$\begin{aligned}\mathcal{H}_{\mathrm{ST}} &= -\frac{2t'^2}{U}\times\sum_{\langle i'j'\rangle\sigma}\Big\{(1-n^A_{i'\sigma})n^A_{i'\bar{\sigma}}(1-n^B_{j'\bar{\sigma}})n^B_{j'\sigma}\\ &\quad -a^\dagger_{i'\sigma}a_{i'\bar{\sigma}}(1-n^A_{i'\sigma})n^A_{i'\bar{\sigma}}b^\dagger_{j'\bar{\sigma}}b_{j'\sigma}(1-n^B_{j'\bar{\sigma}})n^B_{j'\sigma}\Big\}\\ &\quad -\frac{2t^2}{U}\times\sum_{\langle ij\rangle\sigma}n^A_{i\sigma}\left(1-n^A_{i\bar{\sigma}}\right)n^B_{j\bar{\sigma}}\left(1-n^B_{j\sigma}\right). \qquad (3.141)\end{aligned}$$

We again recast everything in terms of the pseudo-spin operators are defined in Equation (3.100). We further define the spin-raising and -lowering operators as

$$S^{\alpha+}_i = \frac{1}{2}(S^{\alpha x}_i + iS^{\alpha y}_i) = \frac{1}{2}\alpha^\dagger_{i\uparrow}\alpha_{i\downarrow}, \qquad (3.142)$$

$$S^{\alpha-}_i = \frac{1}{2}(S^{\alpha x}_i - iS^{\alpha y}_i) = \frac{1}{2}\alpha^\dagger_{i\downarrow}\alpha_{i\uparrow}. \qquad (3.143)$$

Using our previous results in Section (3.3.1), we obtain

$$\begin{aligned}\mathcal{H}_{\mathrm{ST}} &= -\frac{4t'^2}{U}\sum_{\langle i'j'\rangle}\big\{S^{Az}_{i'}S^{Bz}_{j'}(4S^{Az}_{i'}S^{Bz}_{j'}-1)-2S^{A-}_{i'}S^{Bz}_{i'}(2S^{Az}_{i'}+1)S^{B+}_{j'}S^{Bz}_{j'}(2S^{z}_{Bj'}-1)\\ &\quad -2S^{A+}_{i'}S^{Az}_{i'}(2S^{Az}_{i'}-1)S^{B-}_{j'}S^{Bz}_{j'}(2S^{Bz}_{j'}+1)\big\}-\frac{4t^2}{U}\sum_{\langle ij\rangle}S^{Az}_iS^{Bz}_j(4S^{Az}_iS^{Bz}_j-1)\\ &= -\frac{4t'^2}{U}\sum_{\langle i'j'\rangle}\big\{S^{Az}_{i'}S^{Bz}_{j'}(4S^{Az}_{i'}S^{Bz}_{j'}-1)-S^{Ax}_{i'}S^{Bx}_{j'}-S^{Ay}_{i'}S^{By}_{j'}\big\}\\ &\quad -\frac{4t^2}{U}\sum_{\langle ij\rangle}S^{Az}_iS^{Bz}_j(4S^{Az}_iS^{Bz}_j-1) \qquad (3.144)\end{aligned}$$

We note that

$$\begin{aligned}\left(S_{i'}^{Az}S_{j'}^{Bz}\right)^2 &= \frac{1}{16}(n_{i'\uparrow}^A - n_{i'\downarrow}^A)^2(n_{j'\uparrow}^B - n_{j'\downarrow}^B)^2 \\ &= \frac{1}{16}(n_{i'\uparrow}^A + n_{i'\downarrow}^A - 2n_{i'\uparrow}^A n_{i'\downarrow}^A)(n_{j'\downarrow}^B + n_{j'\downarrow}^B - 2n_{j'\uparrow}^B n_{j'\downarrow}^B) \\ &= \frac{1}{16}n_{i'}^A n_{j'}^B, \end{aligned} \tag{3.145}$$

where $n_i^\alpha = \sum_\sigma n_{i\sigma}^\alpha$. In the subspace of single-occupancy, we always have

$$n_{i'\uparrow}^A n_{i'\downarrow}^A = n_{j'\uparrow}^B n_{j'\downarrow}^B = 0 \tag{3.146}$$

and

$$n_{i'}^A = n_{j'}^B = 1. \tag{3.147}$$

Equation (3.146) has been used in the calculation in Equation (3.145). So the terms $\left(S_{i'}^{Az}S_{j'}^{Bz}\right)^2$ and $\left(S_i^{Az}S_j^{Bz}\right)^2$ each contribute a constant, and thus both can be omitted.

Now consider

$$\begin{aligned} S_{i'}^{Az}S_{j'}^{Bz} &= \frac{1}{4}(n_{i'\uparrow}^A - n_{i'\downarrow}^A)(n_{j'\uparrow}^B - n_{j'\downarrow}^B) \\ &= \frac{1}{4}(n_{i'\uparrow}^A n_{j'\uparrow}^B + n_{j'\downarrow}^B n_{j'\downarrow}^B - n_{i'\uparrow}^A n_{j'\downarrow}^B - n_{i'\downarrow}^A n_{j'\uparrow}^B). \end{aligned} \tag{3.148}$$

Note that we consider the Hilbert space spanned by the basis $\{|\uparrow,\downarrow\rangle, |\downarrow,\uparrow\rangle\}$, and that

$$\begin{aligned} &n_{i'\uparrow}^A n_{j'\uparrow}^B |\uparrow,\downarrow\rangle = n_{i'\uparrow}^A n_{j'\uparrow}^B |\downarrow,\uparrow\rangle = 0, \\ &n_{i'\downarrow}^A n_{j'\downarrow}^B |\uparrow,\downarrow\rangle = n_{i'\downarrow}^A n_{j'\downarrow}^B |\uparrow,\downarrow\rangle = 0, \\ &\left(n_{i'\uparrow}^A n_{j'\downarrow}^B + n_{i'\downarrow}^A n_{j'\uparrow}^B\right)|\uparrow,\downarrow\rangle = |\uparrow,\downarrow\rangle, \\ &\left(n_{i'\uparrow}^A n_{j'\downarrow}^B + n_{i'\downarrow}^A n_{j'\uparrow}^B\right)|\downarrow,\uparrow\rangle = |\downarrow,\uparrow\rangle. \end{aligned} \tag{3.149}$$

Thus we have

$$S_{i'}^{Az} S_{j'}^{Bz} = -\frac{1}{4}. \tag{3.150}$$

This term also contributes a constant, and thus does not contribute to the dynamics.

Omitting the above constants, we have

$$\mathcal{H}_{\rm ST} = \frac{4t'^2}{U} \sum_{\langle i'j' \rangle} \left(S_{i'}^{Ax} S_{j'}^{Bx} + S_{i'}^{Ay} S_{j'}^{By} \right) + \frac{4t^2}{U} \sum_{\langle ij \rangle} S_i^{Az} S_j^{Bz}. \tag{3.151}$$

This Hamiltonian again favors the anti-alignment of spins. The new piece of information that is carried by the Hamiltonian (3.151), but not by the Hamiltonian (3.107), is that the roles played by the super-exchange interactions $\frac{4t^2}{U}$ and $\frac{4t'^2}{U}$ are different from each other. The re-writing of the Hamiltonian (3.151) in the next section will clarify this point further.

3.3.2.3 Dimers as entities

It turns out to be rewarding to consider each dimer in the $\boldsymbol{c}_1$ direction as a single entity, which is the correct picture in the limit $t'/t \to \infty$. In this section we re-write the model (3.151) in this picture. This will shed light on the different roles played by the two super-exchange interactions $\frac{4t^2}{U}$ and $\frac{4t'^2}{U}$, and reveal better the microscopic structure of the phase space in the large-$\{U, t'\}$ limit.

To this end, we define the creation and annihilation operators for a particular dimer composed of lattice sites i' and j':

$$\begin{aligned} a_+ &= b_{j'\downarrow} a_{i'\uparrow}, \;\; a_+^\dagger = a_{i'\uparrow}^\dagger b_{j'\downarrow}^\dagger, \\ a_- &= b_{j'\uparrow} a_{i'\downarrow}, \;\; a_-^\dagger = a_{i'\downarrow}^\dagger b_{j'\uparrow}^\dagger, \end{aligned} \tag{3.152}$$

so that

$$a_+^\dagger|0\rangle = a_{i'\uparrow}^\dagger b_{j'\downarrow}^\dagger|0\rangle = |\uparrow,\downarrow\rangle,$$
$$a_-^\dagger|0\rangle = a_{i'\downarrow}^\dagger b_{j'\uparrow}^\dagger|0\rangle = |\downarrow,\uparrow\rangle, \tag{3.153}$$

and

$$n_+ = a_+^\dagger a_+ = a_{i'\uparrow}^\dagger b_{j'\downarrow}^\dagger b_{j'\downarrow} a_{i'\uparrow} = n_{i'\uparrow}^A n_{j'\downarrow}^B,$$
$$n_- = a_-^\dagger a_- = a_{i'\downarrow}^\dagger b_{j'\uparrow}^\dagger b_{j'\uparrow} a_{i'\downarrow} = n_{i'\downarrow}^A n_{j'\uparrow}^B. \tag{3.154}$$

The pseudo-spin operators in this dimer picture are defined as

$$\begin{aligned}
\mathbb{S}^x &= \frac{1}{2}(a_+^\dagger, a_-^\dagger)\begin{pmatrix} 0 & 1 \\ 1 & 0 \end{pmatrix}\begin{pmatrix} a_+ \\ a_- \end{pmatrix}, \\
\mathbb{S}^y &= \frac{1}{2}(a_+^\dagger, a_-^\dagger)\begin{pmatrix} 0 & -i \\ i & 0 \end{pmatrix}\begin{pmatrix} a_+ \\ a_- \end{pmatrix}, \\
\mathbb{S}^z &= \frac{1}{2}(a_+^\dagger, a_-^\dagger)\begin{pmatrix} 1 & 0 \\ 0 & -1 \end{pmatrix}\begin{pmatrix} a_+ \\ a_- \end{pmatrix}.
\end{aligned} \tag{3.155}$$

It can be easily checked that the usual commutation relations for spin operators, namely

$$\left[\mathbb{S}^j, \mathbb{S}^k\right] = i\epsilon_{jkl}\mathbb{S}^l, \tag{3.156}$$

where ϵ_{jkl} is the Levi-Civita symbol, are obeyed. Explicitly, these operators in

terms of the original fermionic operators are given by

$$\begin{aligned} 2\mathbb{S}^x &= a_+^\dagger a_- + a_-^\dagger a_+ \\ &= a_{i'\uparrow}^\dagger a_{i'\downarrow} b_{j'\downarrow}^\dagger b_{j'\uparrow} + a_{i'\downarrow}^\dagger a_{i'\uparrow} b_{j'\uparrow}^\dagger b_{j'\downarrow}, \\ -i2\mathbb{S}^y &= a_-^\dagger a_+ - a_+^\dagger a_- \\ &= a_{i'\downarrow}^\dagger a_{i'\uparrow} b_{j'\uparrow}^\dagger b_{j'\downarrow} - a_{i'\uparrow}^\dagger a_{i'\downarrow} b_{j'\downarrow}^\dagger b_{j'\uparrow} \\ 2\mathbb{S}^z &= n_+ - n_- \\ &= n_{i'\uparrow}^A n_{j'\downarrow}^B - n_{i'\downarrow}^A n_{j'\uparrow}^B. \end{aligned} \tag{3.157}$$

The intra-dimer-hopping terms in the Hamiltonian (3.151) give

$$\begin{aligned} S_{i'}^{Ax} S_{j'}^{Ax} + S_{i'}^{Ay} S_{j'}^{Ay} &= \frac{1}{2}(a_{i'\uparrow}^\dagger a_{i'\downarrow} b_{j'\downarrow}^\dagger b_{j'\uparrow} + a_{i'\downarrow}^\dagger a_{i'\uparrow} b_{j'\uparrow}^\dagger b_{j'\downarrow}) \\ &= \mathbb{S}_n^x, \end{aligned} \tag{3.158}$$

where the subscript n labels the dimer composing of lattice sites i' and j'.

For the inter-dimer-hopping terms, we have

$$S_i^{Az} S_j^{Bz} = \frac{1}{4}(n_{i\uparrow}^A - n_{i\downarrow}^A)(n_{j\uparrow}^B - n_{j\downarrow}^B). \tag{3.159}$$

Because the particular Hilbert space that we are considering is spanned by the dimer states $|\uparrow,\downarrow\rangle$ and $|\downarrow,\uparrow\rangle$, we can infer the spin state on one lattice site from that on the other site in the same dimer. For example, we have

$$n_{i'\uparrow}^A \to n_{i'\uparrow}^A n_{j'\downarrow}^B, n_{j'\downarrow}^B \to n_{i'\uparrow}^A n_{j'\downarrow}^B, \tag{3.160}$$

where lattice sites i' and j' belong to the same dimer. We use this simple obser-

vation to re-write the inter-dimer-hopping term (3.159):

$$S_i^{Az} S_j^{Bz} \equiv -\frac{1}{4}(n_{j'\uparrow}^A n_{j\downarrow}^B - n_{j'\downarrow}^A n_{j\uparrow}^B)(n_{i\uparrow}^A n_{i'\downarrow}^B - n_{i\downarrow}^A n_{i'\uparrow}^B) = -\mathbb{S}_n^z \mathbb{S}_{n+1}^z, \tag{3.161}$$

where the nth dimer is composed of sites i and i', and the $(n+1)$th dimer is composed of sites j' and j.

In summary, the effective Hamiltonian in this dimer picture becomes

$$\mathcal{H}_{\rm ST} = \frac{4t'^2}{U}\sum_n \mathbb{S}_n^x - \frac{4t^2}{U}\sum_{\langle n,n+1\rangle} \mathbb{S}_n^z \mathbb{S}_{n+1}^z. \tag{3.162}$$

As we can see, this simple re-writing of the effective Hamiltonian (3.151) results in nothing other than the quantum Ising model. The intra-dimer-super-exchange $\frac{4t'^2}{U}$ acts as the external magnetic field in the x-direction, while the inter-dimer-super-exchange $\frac{4t^2}{U}$ acts as the nearest-neighbor spin-spin interaction in the z-direction, which tends to destroy the spin order in the x-direction created by the magnetic field. Notice that, while the dimers are arranged in a triangular structure, the inter-dimer interaction exists only between dimers connected by $\boldsymbol{a}_1$ and $\boldsymbol{a}_2$, but not between those connected by the vector $(\boldsymbol{a}_1 - \boldsymbol{a}_2)$ (see Figure 1.1(a)). Thus each dimer effectively has only 4 nearest neighbors, instead of 6 as in the case of the usual triangular lattice. Consequently, the Hamiltonian (3.162) lives on an effective square lattice. This is illustrated in Figure 3.4.

A few observations can be made on the model Hamiltonian (3.162). First of all, it can be checked from their definitions (3.155) that the eigen-relations of $\mathbb{S}^x$ are

$$\begin{aligned} \mathbb{S}^x|{\rm S}\rangle &= -\frac{1}{2}|{\rm S}\rangle, \\ \mathbb{S}^x|{\rm T}\rangle &= \frac{1}{2}|{\rm T}\rangle, \end{aligned} \tag{3.163}$$

where $|{\rm S}\rangle$ and $|{\rm T}\rangle$ are the singlet and triplet states as defined in Equation (3.119),

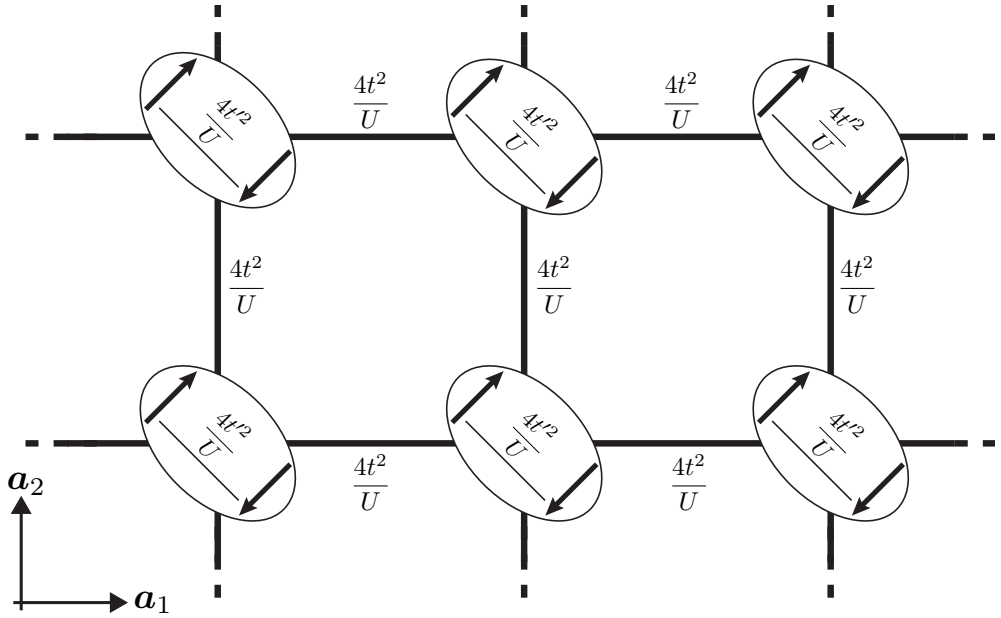

Figure 3.4: A schematic illustration of dimers on a square lattice for the large-U limit. The dimer states are chosen as an example to be $|\uparrow,\downarrow\rangle$ on all sites, corresponding to an antiferromagnetic state. The intra-dimer and inter-dimer superexchange interactions are $\frac{4t'^2}{U}$ and $\frac{4t^2}{U}$, respectively. The horizontal and vertical directions in this illustration correspond to the directions $\boldsymbol{a}_1$ and $\boldsymbol{a}_2$ in Figure 1.1(a), while the dimers are tilted so that they extend in the direction $\boldsymbol{a}_1 - \boldsymbol{a}_2$.

which, in turn, are the eigenstates of the Hamiltonian (3.113) in the limit of large-U/t', as discussed following Equation (3.118). Notice that the singlet state is lower in energy. On the other hand, the eigen-relations of $\mathbb{S}^z$ are

$$\begin{aligned} \mathbb{S}^z|\uparrow,\downarrow\rangle &= \frac{1}{2}|\uparrow,\downarrow\rangle, \\ \mathbb{S}^z|\downarrow,\uparrow\rangle &= -\frac{1}{2}|\downarrow,\uparrow\rangle. \end{aligned} \tag{3.164}$$

Thus the Néel ordered states $|\uparrow,\downarrow\rangle$ and $|\downarrow,\uparrow\rangle$ are the pseudo-spin-$\uparrow$ and pseudo-spin-$\downarrow$ states in the z-direction. As a result, the eigenstate of the first term of the Hamiltonian (3.162) is clearly $|\mathrm{S}\rangle^{\otimes N_\mathrm{c}}$, while, due to the negative sign associated with the $\frac{4t^2}{U}$ interaction as well as the fact that it is second order in $\mathbb{S}^z$, the ground states of the second term are the two degenerate ferromagnetic pseudo-spin states, namely $|\uparrow,\downarrow\rangle^{\otimes N_\mathrm{c}}$ or $|\downarrow,\uparrow\rangle^{\otimes N_\mathrm{c}}$, corresponding to the classical Néel ordered states in the original electronic picture.

The transition between the two ground states is controlled by the relative magnitudes between $\frac{4t^2}{U}$ and $\frac{4t'^2}{U}$, which favor the Néel ordered states and the singlet states on the dimer bonds, respectively. This qualitatively agrees with phase diagram Figure 3.1, in which the antiferromagnetic ordering is destroyed by a sufficiently large value of t'. Specifically, according to the phase diagram, for a particular value of U with $U \gg t$, the Néel ordering is destroyed if $t' \gtrsim U/2$. Furthermore, this phase transition is that of the quantum Ising model on the square lattice, which has been extensively discussed in the literature (see References [88, 89] for example). In particular, first of all, Hamiltonian (3.162) has only one critical point, corresponding to the transition from a paramagnet to a spin-ordered state. Moreover, in the paramagnetic (dimer singlet) phase, the system has exponentially decaying spin-spin correlations, whereas they are constant in the Néel ordered states. Precisely at the transition point, which is second order, one obtains algebraic spin-spin correlation with a power-law dependence on spatial separation [88].

Lastly, the ground state in the limit of large-t', namely $|\mathrm{S}\rangle^{\otimes N_\mathrm{c}}$, which has an exponentially decreasing pseudo-spin-spin correlation as noted above, can be

identified with the gapped spin-liquid phase in the large-t' limit, which will be described in the next chapter.

4

Spin-liquid transition

4.1 The spin-liquid phase transition

In the previous chapter, we have discussed the anti-ferromagnetic phase transition in the honeycomb lattice. Using the mean-field self-consistent method and Stoner's criterion, we obtained the same transition line as plotted in Figure 3.1. As mentioned in the discussion following the mean-field eigenenergies (3.12), this line represents two kinds of transitions that are not separated on the mean-field level: the Mott transition in the charge channel, and the anti-ferromagnetic transition in the spin channel. Indeed, we have seen from Equations (3.12) and (3.26) that the mean-field charge gap Δ_{M} is just proportional to the antiferromagnetic order parameter Δ, $\Delta_{\mathrm{M}} = U\Delta/2$. However, while the anti-ferromagnetic transition requires the Mott transition as a prerequisite, the converse is not true. In other words, it is possible to have a Mott insulator without anti-ferromagnetic spin-ordering. Such a phase is termed the spin-liquid phase. According to the above reasoning, if it exists at all, the spin-liquid phase lies in between the Fermi-liquid (including the (semi-) metallic and band-insulating phases) and the anti-ferromagnetic phases, below the anti-ferromagnetic transition line plotted in Figure 3.1. This is confirmed by the findings in Reference [73].

The spin-liquid phase transition is fundamentally different from the antiferromagnetic transition, in the sense that there is no spontaneous symmetry-breaking in the former transition, and hence no order parameter could be defined. In the antiferromagnetic phase, as compared to the metallic phase, the rotational invariance and sub-lattice-inversion symmetries are broken. These are reflected in the definition of the order parameter (3.4). In particular, the z-direction, along

which the spin-↑ and spin-↓ are defined, is picked out as a special direction, thus breaking the rotational invariance of the metallic phase. The sub-lattice-inversion symmetry is broken because upon exchanging the sub-lattice indices A and B, one has

$$\Delta \to -\Delta. \tag{4.1}$$

In contrast, no such symmetry breaking occurs in the spin-liquid phase transition, the classification of which require the so-called quantum order [65, 90]. Consequently, the usual mean-field self-consistent method that we used to determine the antiferromagnetic transition line is not applicable. Stoner's criterion is clearly not applicable here, either. This is because Stoner's criterion only concerns the instabilities in the spin sector, whereas in the spin-liquid phase transition from a metal to a spin-liquid, only a charge gap is opened, while the spins remain paramagnetic. For this reason, in this chapter the terms *spin-liquid phase transition* and *Mott transition* can be used interchangeably.

As discussed in Section 1.3.3, despite the debate on the feasibility of the spin-liquid phase in the honeycomb lattice, in this chapter we assume the applicability of the slave-rotor method, and use it to investigate the spin-liquid phase of the honeycomb lattice, as well as its evolution with the hopping anisotropy.

4.2 The U(1) slave-rotor method

For the reason stated in the previous section, instead of the standard mean-field method, we use the more sophistiscated slave-rotor method, which is designed for problems involving spin-charge-separation that is precisely what happens here. For a discussion of the relation between the slave-rotor method and other slave particle method, see Reference [69].

In the U(1) slave-rotor method [69, 72], a particle is decoupled into the charge and the spin degrees of freedom:

$$c_{i\sigma} = e^{i\theta_i} f_{i\sigma}, \tag{4.2}$$

where the local phase degree of freedom θ_i is conjugate to the total charge, and the auxiliary fermions $f_{i\sigma}$ (spinons) carry the spin. Notice that the number operator of the original particles coincides with that of the spinons:

$$n_{i\sigma} = c^\dagger_{i\sigma} c_{i\sigma} = f^\dagger_{i\sigma} f_{i\sigma} = n^f_{i\sigma}. \tag{4.3}$$

The angular momentum $L_i = i\partial_{\theta_i}$ is then introduced, whose eigenvalues correspond to the possible number of particles on the lattice site. Due to the Pauli principle, there can be a maximum of two spin-$\frac{1}{2}$ on one lattice: one spin-$\uparrow$ and one spin-$\downarrow$. On the other hand, the eigenvalues of L_i, which are to be interpreted as the possible number of particles on lattice site i, can be any number. In order to discard the unphysical part of the Hilbert space, the constraint

$$L_i + \sum_\sigma f^\dagger_{i\sigma} f_{i\sigma} = 1. \tag{4.4}$$

is imposed with an associated Lagrange multiplier h_i. This constraint glues the charge and the spin degrees of freedom back into one piece, and thus brings the slave-rotor picture back into the physical world.

Because the possible number of spinons are 0, 1 and 2 on the lattice site labelled by i, according to the constraint (4.4), we have the following table:

Eigenvalue of L_i	Occupancy
-1	double occupancy
0	single occupancy
1	vacuum

We may re-write the possible electronic wave functions on a particular lattice site in the slave-rotor picture as

$$\begin{aligned} |\text{vac}\rangle_{\text{elec}} &\equiv |1\rangle_\theta |\text{vac}\rangle_f, \\ |\uparrow\rangle_{\text{elec}} &\equiv |0\rangle_\theta |\uparrow\rangle_f, \\ |\downarrow\rangle_{\text{elec}} &\equiv |0\rangle_\theta |\downarrow\rangle_f, \\ |\uparrow\downarrow\rangle_{\text{elec}} &\equiv |-1\rangle_\theta |\uparrow\downarrow\rangle_f, \end{aligned} \tag{4.5}$$

where the subscript elec indicates the electronic wave function, and $|\text{vac}\rangle$ denotes the vacuum state. Defining that

$$e^{im\theta_i}|l\rangle_\theta = |l+m\rangle_\theta, \tag{4.6}$$

it is easy to check that all the properties of the original ladder operators are obeyed by the slave-rotor operators.

In this thesis, we attempt to use the slave-rotor method to describe two phases: the (semi-)metallic/band-insulating and the spin-liquid phase. In the (semi-)metallic/band-insulating phase, the charges are mobile, so that the number of charges, or the angular momentum L_j, on each lattice site fluctuates. Consequently, the local angular variables θ_j, which are canonically conjugate to each L_j, condense. On the other hand, in the spin-liquid phase, the charges are localized on the lattice sites, while the conjugate angular variable θ_j fluctuates.

In the U(1) slave-rotor method, one obtains complex Lagrangians (or Hamiltonians) for the spin and charge degrees of freedom that are coupled. They may be decoupled on the mean-field level with the help of a set of specially defined mean-field parameters. Then a set of self-consistent equations can be written down using the definitions of the mean-field parameters as well as the observation in the previous paragraph. The phase diagram is then obtained by solving this set of equations.

We would like to point out that the anti-ferromagnetic phase can also be covered within the slave-rotor method. This phase requires interaction induced spin-spin correlations (the super-exchange interaction), which can be realized by either manually introducing a Heisenberg spin-spin interaction term, as was done in Reference [91], or by splitting the interaction into two parts, which are taken to be affecting the charge and spin degrees of freedom, respectively. One such possible splitting scheme would be the re-writing of the interaction term

$$\mathcal{V} = U\sum_i n_{i\uparrow}n_{i\downarrow} = \frac{U}{4}\sum_i \left[(n_{i\uparrow}+n_{i\downarrow})^2 - (n_{i\uparrow}-n_{i\downarrow})^2\right]. \tag{4.7}$$

The first term in the last expression can be re-expressed using the angular momentum L_j and the constraint (4.4), thus taken as affecting the charge degree of freedom, while the antiferromagnetic order parameter (3.4) can be easily implemented in the mean-field decoupling of the second term. This calculation will be similar to the calculation performed in Reference [92], which was done for the symmetric case. It is not covered in this thesis and is left for future investigation.

4.3 The case of the anisotropic honeycomb lattice

The Hubbard model on the isotropic honeycomb lattice was studied within the U(1) slave-rotor method originally in Reference [69] as well as in Reference [71], the latter in the presence of spin-orbit coupling. Here we generalize the approach to the case of the anisotropic honeycomb lattice described by the Hubbard Hamiltonian (3.1). The calculation proceeds as described in the previous section. The set of equations will be solved with the help of Green's functions. There are more than one solutions, so an analysis of the free energy is necessary in order to discriminate them. The resulting phase diagram is then presented as the final result.

4.3.1 Model

At half-filling, the interaction term (3.3) may be re-written, with the help of Equation (4.3) and (4.4), as

$$\mathcal{V} = U \sum_i (n_{i\uparrow} - \frac{1}{2})(n_{i\downarrow} - \frac{1}{2}) = \frac{U}{2} \sum_i (\sum_\sigma n_{i\sigma} - 1)^2 = \frac{U}{2} \sum_i L_i^2 \tag{4.8}$$

up to a constant term with no dynamical importance. The Hamiltonian (3.1) in this slave-rotor picture becomes

$$\mathcal{H} = -\sum_{\langle ij \rangle \sigma} t_{ij} (f_{i\sigma}^{A\dagger} f_{j\sigma}^{B} e^{-i\theta_{ij}} + \text{H.c.}) + \frac{U}{2} \sum_i L_i^2 - \sum_i h_i (L_i + f_{i\sigma}^\dagger f_{i\sigma}), \tag{4.9}$$

where $\theta_{ij} = \theta_i - \theta_j$ and h_i is the Lagrange multiplier implementing the constraint (4.4).

The canonical conjugation relation

$$i\partial_\tau \theta_i = \frac{\partial \mathcal{H}}{\partial L_i} \tag{4.10}$$

implies (h will eventually be zero as will be discussed a bit further on)

$$L_i = \frac{i}{U}\partial_\tau \theta_i. \tag{4.11}$$

To proceed, we replace the phase field θ_i by the complex field X_j, with

$$X_j = e^{i\theta_j}. \tag{4.12}$$

The physical constraint

$$|X_j|^2 = 1 \tag{4.13}$$

is implemented with the help of the Lagrange multiplier ρ_j. In terms of the field X_j, the angular momentum is written as

$$L_j = \frac{1}{U} X_j^\dagger \partial_\tau X_j. \tag{4.14}$$

We consider the case described in Equation (1.29), and define the following mean-field operators:

$$\begin{aligned} Q_\theta &= \sum_\sigma \langle f_{i\sigma}^\dagger f_{j\sigma}\rangle_f,\ Q_f = \langle X_i^\dagger X_j\rangle_\theta, \\ Q'_\theta &= \sum_\sigma \langle f_{i'\sigma}^\dagger f_{j'\sigma}\rangle_f,\ Q'_f = \langle X_{i'}^\dagger X_{j'}\rangle_\theta. \end{aligned} \tag{4.15}$$

where $\langle ij\rangle$ and $\langle i'j'\rangle$ are nearest neighboring sites along the directions $\boldsymbol{c}_{2,3}$ and $\boldsymbol{c}_1$, respectively. The subscripts f and θ in Equations (4.15) indicate that the expectation values are defined using the mean-field Hamiltonians $\mathcal{H}_f$ and $\mathcal{H}_\theta$ defined below. Making use of the mean-field approximation relation $\alpha\beta \approx \langle\alpha\rangle\beta + \langle\beta\rangle\alpha - \langle\alpha\rangle\langle\beta\rangle$, we obtain

$$\mathcal{H} \approx \mathcal{H}_f + \mathcal{H}_\theta, \tag{4.16}$$

where

$$\mathcal{H}_f = \left(-t\sum_{\langle ij\rangle\sigma} Q_f f_{i\sigma}^{A\dagger} f_{j\sigma}^{B} - t'\sum_{\langle i'j'\rangle\sigma} Q'_f f_{i'\sigma}^{A\dagger} f_{j'\sigma}^{B}\right) + \text{H.c.} - \sum_{i\sigma} h_i n_{i\sigma}^{f}, \tag{4.17a}$$

$$\begin{aligned}\mathcal{H}_\theta = &\left(-t\sum_{\langle ij\rangle} Q_\theta X_i^{A\dagger} X_j^{B} - t'\sum_{\langle i'j'\rangle} Q'_\theta X_{i'}^{A\dagger} X_{j'}^{B}\right) + \text{H.c.} \\ &- \sum_j \frac{h_j}{U} X_j^\dagger \partial_\tau X_j - \frac{1}{2U}\sum_j (i\partial_\tau X_j^\dagger)(-i\partial_\tau X_j) - \sum_j \rho_j X_j^\dagger X_j,\end{aligned} \tag{4.17b}$$

self-consistently couple to each other via Equations (4.15). Notice that in Equations (4.17) we have omitted the constant term $-\langle\alpha\rangle\langle\beta\rangle$, which will be important only in the free energy analysis performed later. According to Equation (4.3), the filling of the spinons is the same as that of the electrons, which is half-filling in the present case. Assuming the h-field to be spatially uniform, i.e.

$$\sum_{i\sigma} h_i n_{i\sigma}^{f} \to h\sum_{i\sigma} n_{i\sigma}^{f}, \tag{4.18}$$

particle-hole symmetry in $\mathcal{H}_f$ then dictates that

$$h = 0. \tag{4.19}$$

The spinons are governed by the quasi-free Hamiltonian $\mathcal{H}_f$, which does not have an interaction term. This implies that there can be no spin-ordering within this model. Because the form of $\mathcal{H}_f$ parallels that of the kinetic Hamiltonian (1.14), the discussion in Section 1.2.2 about the topological phase transition applies to the spinon Hamiltonian $\mathcal{H}_f$. Explicitly, the phase transition occurs at

$$t'Q'_f = 2tQ_f. \tag{4.20}$$

In other words, the spinon excitations are gapless Dirac fermions if $t'Q'_f < 2tQ_f$, and gapped if $t'Q'_f > 2tQ_f$. The charge degree of freedom, on the other hand, is described by the quantum XY lattice Hamiltonian $\mathcal{H}_\theta$, the disordering transition of which corresponds to the opening of the charge gap, which is the essence of the Mott transition.

$\mathcal{H}_f$ and the kinetic part of $\mathcal{H}_\theta$ are easily diagonalized in momentum space via the Fourier transform defined similar to Equation (1.15). We obtain

$$\begin{aligned} f^{u\dagger}_{\boldsymbol{k}\sigma} &= \frac{1}{\sqrt{2}}(f^{A\dagger}_{\boldsymbol{k}\sigma} + e^{-i\theta^{\boldsymbol{k}}_{\Gamma f}} f^{B\dagger}_{\boldsymbol{k}\sigma}),\ f^{l\dagger}_{\boldsymbol{k}\sigma} = \frac{1}{\sqrt{2}}(f^{A\dagger}_{\boldsymbol{k}\sigma} - e^{-i\theta^{\boldsymbol{k}}_{\Gamma f}} f^{B\dagger}_{\boldsymbol{k}\sigma}), \\ X^{u\dagger}_{\boldsymbol{k}} &= \frac{1}{\sqrt{2}}(X^{A\dagger}_{\boldsymbol{k}} + e^{-i\theta^{\boldsymbol{k}}_{\Gamma\theta}} X^{B\dagger}_{\boldsymbol{k}}),\ X^{l\dagger}_{\boldsymbol{k}} = \frac{1}{\sqrt{2}}(X^{A\dagger}_{\boldsymbol{k}} - e^{-i\theta^{\boldsymbol{k}}_{\Gamma\theta}} X^{B\dagger}_{\boldsymbol{k}}), \end{aligned} \tag{4.21}$$

where the superscripts u and l denote the upper and lower energy levels, respectively, and

$$e^{i\theta^{\boldsymbol{k}}_{\Gamma f}} = \frac{\Gamma^{\boldsymbol{k}}_f}{|\Gamma^{\boldsymbol{k}}_f|},\ e^{i\theta^{\boldsymbol{k}}_{\Gamma\theta}} = \frac{\Gamma^{\boldsymbol{k}}_\theta}{|\Gamma^{\boldsymbol{k}}_\theta|} \tag{4.22}$$

with

$$\Gamma^{\boldsymbol{k}}_f = g^{\boldsymbol{k}}Q_f + g'^{\boldsymbol{k}}Q'_f, \Gamma^{\boldsymbol{k}}_\theta = g^{\boldsymbol{k}}Q_\theta + g'^{\boldsymbol{k}}Q'_\theta \tag{4.23}$$

and

$$g^{\boldsymbol{k}} = t(e^{i\boldsymbol{c}_2\cdot\boldsymbol{k}} + e^{i\boldsymbol{c}_3\cdot\boldsymbol{k}}),\ g'^{\boldsymbol{k}} = t'e^{i\boldsymbol{c}_1\cdot\boldsymbol{k}}. \tag{4.24}$$

The action is built from

$$\begin{aligned} S &\equiv \int_0^\beta d\tau \left\{ \sum_j \left[-iL_j \partial_\tau \theta_j + \sum_\sigma \bar{f}_{j\sigma} \partial_\tau f_{j\sigma} \right] + \mathcal{H} \right\} \\ &= S_f + S_\theta + \cdots = \int_0^\beta d\tau \mathcal{L}_f + \int_0^\beta d\tau \mathcal{L}_\theta + \cdots \end{aligned} \tag{4.25}$$

where

$$\mathcal{L}_f = \left(-tQ_f \sum_{\langle ij \rangle \sigma} \bar{f}^A_{i\sigma} f^B_{j\sigma} - t'Q'_f \sum_{\langle i'j' \rangle \sigma} \bar{f}^A_{i'\sigma} f^B_{j'\sigma} \right) + \text{H.c.} + \sum_{i\sigma} \bar{f}_{i\sigma} \partial_\tau f_{i\sigma}, \tag{4.26a}$$

$$\begin{aligned} \mathcal{L}_\theta &= \left(-tQ_\theta \sum_{\langle ij \rangle} X^{A*}_i X^B_j - t'Q'_\theta \sum_{\langle i'j' \rangle} X^{A*}_{i'} X^B_{j'} \right) + \text{H.c.} \\ &\quad + \frac{1}{2U} \sum_j (\partial_\tau X^*_j)(\partial_\tau X_j) - \rho \sum_j |X_j|^2. \end{aligned} \tag{4.26b}$$

In these equations, all fermionic and bosonic operators have been replaced by corresponding Grassmann and complex variables, respectively. The ellipsis in Equation (4.25) stand for terms that are independent of the variables f and X, and $\bar{f}$ denotes the conjugate of the Grassmann variable f. The ρ-field, which plays the role of the chemical potential of the X-field, is assumed to be uniform in this mean-field treatment.

Switching to the energy eigenspace via Fourier transformation and Equations (4.21), we obtain

$$\begin{aligned} S_f &= \int_0^\beta d\tau \mathcal{L}_f = \int_0^\beta d\tau \sum_{\boldsymbol{k}\sigma} \bar{f}^l_{\boldsymbol{k}\sigma} (\partial_\tau - |\Gamma^{\boldsymbol{k}}_f|) f^l_{\boldsymbol{k}\sigma}, \\ S_\theta &= \int_0^\beta d\tau \mathcal{L}_\theta = \int_0^\beta d\tau \sum_{\boldsymbol{k}} X^{l*}_{\boldsymbol{k}} (-\frac{1}{2U} \partial^2_\tau - \rho - |\Gamma^{\boldsymbol{k}}_X|) X^l_{\boldsymbol{k}}. \end{aligned} \tag{4.27}$$

Because we are considering the system at half-filling and zero temperature, the upper energy band is not populated. So we have ignored the operators f^u and X^u in the above expressions.

4.3.2 Green's functions

In this section we evaluate the Green's functions, which will be useful in the coming calculation. They can be expressed using the coherent state path integrals as

$$G_f(\boldsymbol{k},\tau) = -\langle f^l_{\boldsymbol{k}\sigma}(\tau) f^{l\dagger}_{\boldsymbol{k}\sigma}(0)\rangle = -\frac{\int \mathcal{D}^2[f^l_{\boldsymbol{\kappa}\sigma}(\tau')] f^l_{\boldsymbol{k}\sigma}(\tau)\bar{f}^l_{\boldsymbol{k}\sigma}(0) e^{-S_f}}{\int \mathcal{D}^2[f^l_{\boldsymbol{\kappa}\sigma}(\tau')] e^{-S_f}}, \quad (4.28)$$

$$G_\theta(\boldsymbol{k},\tau) = -\langle X^l_{\boldsymbol{k}}(\tau) X^{l\dagger}_{\boldsymbol{k}}(0)\rangle = -\frac{\int \mathcal{D}^2[X^l_{\boldsymbol{\kappa}}(\tau')] X^l_{\boldsymbol{k}}(\tau) X^{l*}_{\boldsymbol{k}}(0) e^{-S_\theta}}{\int \mathcal{D}^2[X^l_{\boldsymbol{\kappa}}(\tau')] e^{-S_\theta}}, \quad (4.29)$$

where

$$\mathcal{D}^2[f^l_{\boldsymbol{\kappa}\sigma}(\tau')] = \prod_{\boldsymbol{k}\sigma i} \frac{df^l_{\boldsymbol{k}\sigma i} d\bar{f}^l_{\boldsymbol{k}\sigma i}}{2\pi i}, \mathcal{D}^2[X^l_{\boldsymbol{\kappa}}(\tau')] = \prod_{\boldsymbol{k}i} \frac{dX^l_{\boldsymbol{k}i} dX^{*l}_{\boldsymbol{k}i}}{2\pi i} \quad (4.30)$$

with the index i labelling time steps, $i = 0$ corresponds to $\tau = 0$ and $i \to \infty$ corresponds to $\tau = \beta$. The following formulae [93] are useful in evaluating the path integrals above:

$$\frac{\int \prod_i d\bar{f}_i df_i f_{i'} \bar{f}_{j'} e^{-\sum_{ij} \bar{f}_i H_{ij} f_j}}{\int \prod_i d\bar{f}_i df_i e^{-\sum_{ij} \bar{f}_i H_{ij} f_j}} = -H^{-1}_{i'j'}, \quad (4.31)$$

$$\frac{\int \prod_i dx^*_i dx_i x_{i'} x^*_{j'} e^{-\sum_{ij} x^*_i H_{ij} x_j}}{\int \prod_i dx^*_i dx_i e^{-\sum_{ij} x^*_i H_{ij} x_j}} = H^{-1}_{i'j'}, \quad (4.32)$$

where f are Grassmann variables, x are complex numbers, and H is a matrix with a positive Hermitian part.

The spinon Green's function can be obtained by directly applying Formula

(4.31):

$$G_f(\boldsymbol{k}, i\omega_n) = (i\omega_n + |\Gamma_f^{\boldsymbol{k}}|)^{-1}, \tag{4.33}$$

where $\omega_n = \frac{(2n+1)\pi}{\beta}$ are the fermionic Matsubara frequencies.

4.3.2.1 Green's function for the X-field condensed phase

As discussed in Section (4.2), the (semi-)metallic/band-insulating phase corresponds to the condensed phase of the bosonic θ-field, or, equivalently, the X-field. In this phase, a macroscopic fraction of the field particles occupy the lowest energy

$$E^{\min} = -|\Gamma_\theta^{\max}| = -|2tQ_\theta + t'Q'_\theta| \tag{4.34}$$

with the same sign for Q_θ and Q'_θ. In contrary to the Dirac points, this energy is situated at the Γ point corresponding to $\boldsymbol{k} = 0$ at the center of the FBZ, which point thus calls for special treatment. Let the number of particles in the condensate be N_0. The Hamiltonian for the X-field in this condensed phase is

$$\mathcal{H}_\theta = -(\rho + |\Gamma_\theta^{\max}|)N_0 - \sum_{\boldsymbol{k}\neq 0}(\rho + |\Gamma_\theta^{\boldsymbol{k}}|)X_{\boldsymbol{k}}^\dagger X_{\boldsymbol{k}} - \frac{1}{2U}\sum_{\boldsymbol{k}\neq 0}(i\partial_\tau X_{\boldsymbol{k}}^\dagger)(-i\partial_\tau X_{\boldsymbol{k}}). \tag{4.35}$$

Like in a Bose-Einstein condensate, the chemical potential ρ in this condensed phase is equal to the lowest energy $-|\Gamma_\theta^{\max}|$, which is shown in Equation (4.34). The corresponding Lagrangian is

$$\mathcal{L}_\theta = \sum_{\boldsymbol{k}\neq 0} X_{\boldsymbol{k}}^\dagger \left(-\frac{\partial_\tau^2}{2U} + |\Gamma_\theta^{\max}| - |\Gamma_\theta^{\boldsymbol{k}}|\right) X_{\boldsymbol{k}} + \frac{1}{2U}\sum_{\boldsymbol{k}\neq 0}\partial_\tau\left(X_{\boldsymbol{k}}^\dagger \partial_\tau X_{\boldsymbol{k}}\right). \tag{4.36}$$

As a result, the action is

$$S_\theta = \int_0^\beta \mathcal{L}_\theta = \int_0^\beta \sum_{\boldsymbol{k}\neq 0} X_{\boldsymbol{k}}^\dagger \left(-\frac{\partial_\tau^2}{2U} + |\Gamma_\theta^{\max}| - |\Gamma_\theta^{\boldsymbol{k}}| \right) X_{\boldsymbol{k}}. \tag{4.37}$$

For nonzero wave vector, applying Equation (4.32), the Green's function is [94]

$$G_\theta(\boldsymbol{k}, i\nu_n) = -\left[\nu_n^2/U + \left(|\Gamma_\theta^{\max}| - |\Gamma_\theta^{\boldsymbol{k}}|\right)\right]^{-1},\ \boldsymbol{k} \neq 0; \tag{4.38}$$

while for $\boldsymbol{k} = 0$, provided that $N_0 \gg 1$, we can make the approximations

$$X_0 = X_0^\dagger \approx \sqrt{N_0}, \tag{4.39}$$

Thus we have

$$G_\theta(\boldsymbol{k} = 0, \tau) = -N_0 \tag{4.40}$$

directly from its definition Equation (4.29). Note that $\nu_n = \frac{2n\pi}{\beta}$ are the bosonic Matsubara frequencies.

4.3.2.2 Green's function for the X-field disordered phase

In the X-field disordered phase, we have infinitesimal N_0 by definition, and thus a chemical potential ρ such that $\rho < -|\Gamma_\theta^{\max}|$ [95]. The particle number, which is conjugate to the θ-field, is thus fixed on each lattice site, corresponding to the Mott-insulating phase. The difference between ρ and $-|\Gamma_\theta^{\max}|$ is naturally related to the nonzero charge gap in this phase, which will be defined in Equation (4.61) later.

For this case, we may apply Equation (4.32), and obtain [94]

$$G_\theta(\boldsymbol{k}, i\nu_n) = -[\nu_n^2/U + (|\rho| - |\Gamma_\theta^{\boldsymbol{k}}|)]^{-1}. \tag{4.41}$$

4.3.3 Mean-field equations

With the Green's functions evaluated, we are finally in the position to write down explicitly all the self-consistent equations. This needs to be done for the condensed and disordered phases of the X-field separately. The solutions to the set of equations for the X-field disordered phase would indicate the existence of the spin-liquid phase within our slave-rotor treatment. It is possible to have multiple solutions to the set of equation, which, as we shall see in Section 4.3.4, is indeed the case here. A free energy analysis is then performed in order to identify the true ground state of the system. This is presented in Section 4.3.5.

4.3.3.1 X-field condensed phase

The first self-consistent equation comes from the normalization of the X operators, i.e. (4.13). In terms of the Green's functions, this can be expressed as

$$1 = -\frac{1}{N_\mathrm{c}} \sum_{\boldsymbol{k}} \frac{1}{\beta} \sum_n G_\theta(\boldsymbol{k}, i\nu_n). \tag{4.42}$$

The term for the point $\boldsymbol{k} = 0$ is trivial, while for the rest of the FBZ, the Matsubara sum over the frequencies ν_n gives

$$\frac{1}{\beta} \sum_n G_\theta(\boldsymbol{k}, i\nu_n) = -\frac{U}{2\sqrt{U(|\Gamma_\theta^{\max}| - |\Gamma_\theta^{\boldsymbol{k}}|)}} \coth \frac{\beta\sqrt{U(|\Gamma_\theta^{\max}| - |\Gamma_\theta^{\boldsymbol{k}}|)}}{2}. \tag{4.43}$$

Define

$$n_0 = \frac{N_0}{2N_\mathrm{c}}, \tag{4.44}$$

which is the fraction of the particles in the condensate. The resulting equation is

$$1 = 2n_0 + \frac{1}{2N_\mathrm{c}} \sum_{\boldsymbol{k}\neq 0} \sqrt{\frac{U}{(|\Gamma_\theta^{\max}| - |\Gamma_\theta^{\boldsymbol{k}}|)}} \coth \frac{\beta\sqrt{U(|\Gamma_\theta^{\max}| - |\Gamma_\theta^{\boldsymbol{k}}|)}}{2}. \tag{4.45}$$

We consider the 0-T limit, in which case the coth factor on the right hand side of the above equation is just 1.

The rest of the self-consistent equations are obtained from the definitions of the mean-field parameters in Equations (4.15). For the purpose of illustration, we calculate Q_f and Q_θ explicitly:

$$\begin{aligned} 2tQ_f &= t\sum_{j=1,2}\langle X_i^{A\dagger}X_j^B\rangle = \frac{1}{N_{\rm c}}\sum_{\boldsymbol{k}} g^{\boldsymbol{k}}\langle X_{\boldsymbol{k}}^{A\dagger}X_{\boldsymbol{k}}^B\rangle \\ &= 2n_0 - \frac{1}{2N_{\rm c}}\sum_{\boldsymbol{k}\neq 0} g^{\boldsymbol{k}} e^{-i\theta_{\Gamma\theta}^{\boldsymbol{k}}}\langle X_{\boldsymbol{k}}^{l\dagger}X_{\boldsymbol{k}}^l\rangle \\ &= 2n_0 - \frac{1}{2N_{\rm c}}\sum_{\boldsymbol{k}\neq 0} g^{\boldsymbol{k}} e^{-i\theta_{\Gamma\theta}^{\boldsymbol{k}}}[-\frac{1}{\beta}\sum_n G(\boldsymbol{k},i\nu_n)] \\ &= 2n_0 - \frac{1}{4N_{\rm c}}\sum_{\boldsymbol{k}\neq 0}\frac{Q_\theta|g^{\boldsymbol{k}}|^2 + Q'_\theta g^{\boldsymbol{k}}g'^{\boldsymbol{k}*}}{|\Gamma_\theta^{\boldsymbol{k}}|}\sqrt{\frac{U}{|\Gamma_\theta^{\rm max}| - |\Gamma_\theta^{\boldsymbol{k}}|}}; \end{aligned} \tag{4.46}$$

$$\begin{aligned} 2tQ_\theta &= t\sum_{j=1,2}\sum_\sigma\langle f_{i\sigma}^{A\dagger}f_{j\sigma}^B\rangle = \frac{1}{N_{\rm c}}\sum_{\boldsymbol{k}} g^{\boldsymbol{k}}\sum_\sigma\langle f_{\boldsymbol{k}\sigma}^{A\dagger}f_{\boldsymbol{k}\sigma}^B\rangle \\ &= -\frac{1}{2N_{\rm c}}\sum_{\boldsymbol{k}} g^{\boldsymbol{k}} e^{-i\theta_\Gamma^{\boldsymbol{k}}}\sum_\sigma\langle f_{\boldsymbol{k}\sigma}^{l\dagger}f_{\boldsymbol{k}\sigma}^l\rangle \\ &= -\frac{1}{N_{\rm c}}\sum_{\boldsymbol{k}} g^{\boldsymbol{k}} e^{-i\theta_\Gamma^{\boldsymbol{k}}} \\ &= -\frac{1}{N_{\rm c}}\sum_{\boldsymbol{k}}\frac{Q_f|g^{\boldsymbol{k}}|^2 + Q'_f g^{\boldsymbol{k}}g'^{\boldsymbol{k}*}}{|\Gamma_f^{\boldsymbol{k}}|}. \end{aligned} \tag{4.47}$$

As a result, we have

$$tQ_f = n_0 - \frac{1}{8N_{\rm c}}\sum_{\boldsymbol{k}\neq 0}\frac{Q_\theta|g^{\boldsymbol{k}}|^2 + Q'_\theta g^{\boldsymbol{k}}g'^{\boldsymbol{k}*}}{|\Gamma_\theta^{\boldsymbol{k}}|}\sqrt{\frac{U}{|\Gamma_\theta^{\rm max}| - |\Gamma_\theta^{\boldsymbol{k}}|}}, \tag{4.48}$$

$$tQ_\theta = -\frac{1}{2N_{\rm c}}\sum_{\boldsymbol{k}}\frac{Q_f|g^{\boldsymbol{k}}|^2 + Q'_f g^{\boldsymbol{k}}g'^{\boldsymbol{k}*}}{|\Gamma_f^{\boldsymbol{k}}|} \tag{4.49}$$

with [see Equation (4.24)]

$$g^{\boldsymbol{k}} = 2t \exp\left(-i\frac{ak_y}{2}\right)\cos\frac{\sqrt{3}ak_x}{2}, g'^{\boldsymbol{k}} = t' \exp\left(iak_y\right). \tag{4.50}$$

Similar considerations lead to the following equations for Q'_f and Q'_θ:

$$t'Q'_f = n_0 - \frac{1}{4N_\mathrm{c}}\sum_{\boldsymbol{k}\neq 0}\frac{Q'_\theta|g'^{\boldsymbol{k}}|^2 + Q_\theta g'^{\boldsymbol{k}} g^{\boldsymbol{k}*}}{|\Gamma_\theta^{\boldsymbol{k}}|}\sqrt{\frac{U}{|\Gamma_\theta^{\max}| - |\Gamma_\theta^{\boldsymbol{k}}|}}, \tag{4.51}$$

$$t'Q'_\theta = -\frac{1}{N_\mathrm{c}}\sum_{\boldsymbol{k}}\frac{Q'_f|g'^{\boldsymbol{k}}|^2 + Q_f g^{\boldsymbol{k}*} g'^{\boldsymbol{k}}}{|\Gamma_f^{\boldsymbol{k}}|}. \tag{4.52}$$

Equations (4.45) and (4.48)-(4.52) form a complete set of self-consistent equations for the X-field condensed phase. The set of variables to be solved for are

$$\left\{n_0, Q_f, Q'_f, Q_\theta, Q'_\theta\right\}. \tag{4.53}$$

4.3.3.2 X-field disordered phase

In the X-field disordered phase, $n_0 = 0$ by definition. Instead, the chemical potential becomes a variable, with [95]

$$\rho < -|\Gamma_\theta^{\max}|. \tag{4.54}$$

To obtain the set of equations for the disordered phase, we start from that for

the condensed phase, set $N_0 = 0$, and replace $|\Gamma_\theta^{\max}|$ by $|\rho|$. The results are:

$$1 = \frac{1}{2N_c}\sum_{\boldsymbol{k}}\sqrt{\frac{U}{(|\rho| - |\Gamma_\theta^{\boldsymbol{k}}|)}}, \tag{4.55}$$

$$tQ_f = -\frac{1}{8N_c}\sum_{\boldsymbol{k}}\frac{Q_\theta|g^{\boldsymbol{k}}|^2 + Q'_\theta g^{\boldsymbol{k}} g'^{\boldsymbol{k}*}}{|\Gamma_\theta^{\boldsymbol{k}}|}\sqrt{\frac{U}{|\rho| - |\Gamma_\theta^{\boldsymbol{k}}|}}, \tag{4.56}$$

$$t'Q'_f = -\frac{1}{4N_c}\sum_{\boldsymbol{k}}\frac{Q'_\theta|g'^{\boldsymbol{k}}|^2 + Q_\theta g'^{\boldsymbol{k}} g^{\boldsymbol{k}*}}{|\Gamma_\theta^{\boldsymbol{k}}|}\sqrt{\frac{U}{|\rho| - |\Gamma_\theta^{\boldsymbol{k}}|}}, \tag{4.57}$$

$$tQ_\theta = -\frac{1}{2N_c}\sum_{\boldsymbol{k}}\frac{Q_f|g^{\boldsymbol{k}}|^2 + Q'_f g'^{\boldsymbol{k}*} g^{\boldsymbol{k}}}{|\Gamma_f^{\boldsymbol{k}}|}, \tag{4.58}$$

$$t'Q'_\theta = -\frac{1}{N_c}\sum_{\boldsymbol{k}}\frac{Q'_f|g'^{\boldsymbol{k}}|^2 + Q_f g^{\boldsymbol{k}*} g'^{\boldsymbol{k}}}{|\Gamma_f^{\boldsymbol{k}}|}. \tag{4.59}$$

Note that all the summations above are over the entire FBZ. The set of variables to be solved for are

$$\left\{\rho, Q_f, Q'_f, Q_\theta, Q'_\theta\right\}. \tag{4.60}$$

4.3.4 Solutions

4.3.4.1 Second order transition line

The charge gap is defined as

$$\Delta_c = 2\sqrt{U(|\rho| - |\Gamma_\theta^{\boldsymbol{k}}|_{\max})}, \tag{4.61}$$

which is nonzero in the Mott-insulating phase (the disordered phase of the X-field), and zero in the metallic/band-insulating phase (the condensed phase of the X-field). The exact opposite is true for the condensate population N_0, which is nonzero in the condensed phase by definition, and zero in the disordered phase. A second order transition of the X-field from the condensed phase to the disordered phase would be signaled by the vanishing of both the charge gap Δ_c and the

condensate population N_0. We can use this information to write down the set of equations for the second order transition line, by either setting $N_0 = 0$ in the equations for the condensed phase, or by setting $\rho = -|\Gamma_\theta^{\max}|$ in the equations for the disordered phase. The resulting transition line is plotted in Figure 4.1. This line has a sharp kink at $t'/t \approx 1.019$, after which the curve goes backward

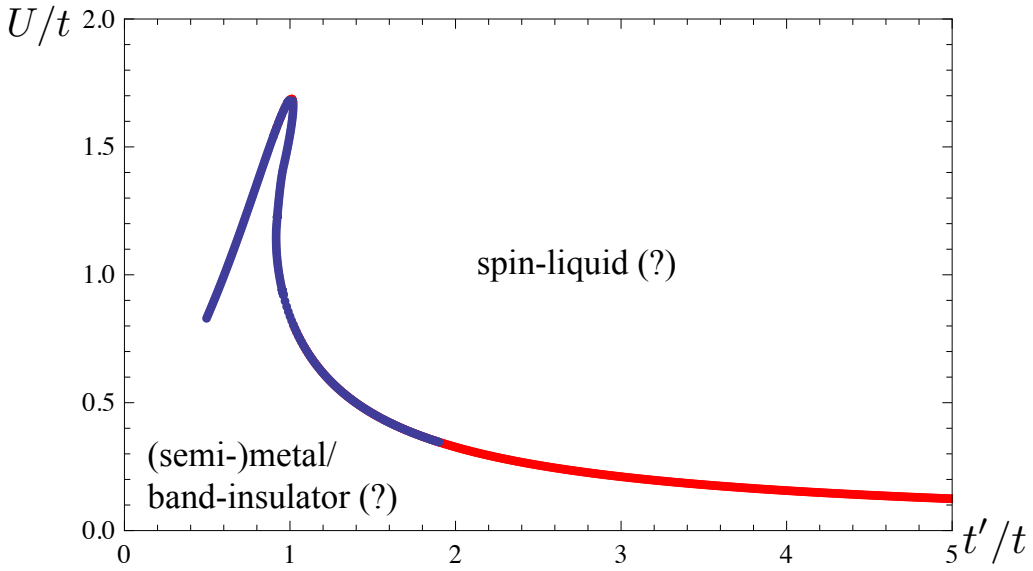

Figure 4.1: The transition line obtained under the assumption of a second order transition. Only part of it forms the true transition line, as will be explained later.

in the direction of decreasing t'/t, and eventually turns again to the direction of increasing t'/t at $t'/t \approx 0.92$. For the values of $0.92 < t'/t < 1.019$, this line is crossed three times upon increasing U, indicating three phase transitions. Similarly, for certain range of U values, upon increasing t', this line is crossed twice, indicating two phase transitions. One would expect the phase above (or to the right of, for the vertical portion) and below (or to the left of) this transition line to be the spin-liquid and the metallic/band-insulating phases, respectively, as indicated in the plot. However, more detailed calculations show that it is not entirely the case. For the upper most part of the curve for $t'/t < 1.019$, i.e. the part of the curve before the sharp kink, everything works as expected; i.e. the phases immediately above and immediately below it are the spin-liquid and the metallic phases, respectively. On the other hand, for the part of the curve after the kink at $t'/t \approx 1.019$, we find the exact opposite. For example, for $t'/t = 1.2$,

immediately above the curve, a nonzero value of n_0 is found, while immediately below the curve, one obtains nonzero Δ_c, indicating a counterintuitive physical picture. This is the reason for us to put question marks in Figure 4.1. These issues will be resolved in the free energy analysis in a coming section, which dictates that the nonphysical part of the second order transition curve is energetically unfavorable, hence does not represent the ground state of the system.

4.3.4.2 First order solutions

In addition to the above second order transition line, we found two other solutions that satisfy Equations (4.55)-(4.59) for the spin-liquid phase:

- The *chain solution* has vanishing mean-field parameters on the bonds in the $\boldsymbol{c}_1$ direction:

$$Q'_f = Q'_\theta = 0, \tag{4.62}$$

  and thus describes a system effectively composed of decoupled zig-zag chains in the $\boldsymbol{c}_2$-$\boldsymbol{c}_3$ direction in Figure 1.1. Self-consistent calculation yields

$$Q_\theta = -\frac{2}{\pi} \approx -0.637 \tag{4.63}$$

  while $Q_f > 0$ and $\rho < -|\Gamma_\theta^{\max}|$, both of which are functions of U. The associated spin-liquid phase in this case is gapless in the spin channel, since

$$t'Q'_f = 0 < 2tQ_f. \tag{4.64}$$

- The *dimer solution* has vanishing parameters on the $\boldsymbol{c}_2$ and $\boldsymbol{c}_3$ directions:

$$Q_f = Q_\theta = 0. \tag{4.65}$$

  Hence this solution describes a system composed of decoupled dimers living on the bonds in the direction $\boldsymbol{c}_1$, as shown in Figure 1.1. Self-consistency

requires that

$$Q'_f = 0.5, Q'_\theta = -1. \tag{4.66}$$

One may easily verify that

$$\Delta_{\rm c} = U \tag{4.67}$$

for this solution, independent of t'. The relation between ρ and U can thus be derived:

$$U = 4(|\rho| - t'). \tag{4.68}$$

This spin-liquid is gapped in the spinon channel, since

$$t'Q'_f = 0.5t' > 2tQ_f = 0. \tag{4.69}$$

These two solutions span the whole phase space, and do not require the presence of the rotor-condensed phase. The transition between these phases and the rotor-condensed phase of the second order solution above will be of first order.

Among the three solutions, the physical solution for each set of model parameters is the one with the lowest free energy, the analysis of which will be presented next.

4.3.5 Free energy analysis

To calculate the free energy, we need to take into account all the dynamically unimportant constants that have been omitted so far, namely those terms proportional to $\langle\alpha\rangle\langle\beta\rangle$ as explained below Equation (4.17). We thus have

$$\mathcal{H} \approx \mathcal{H}_f + \mathcal{H}_\theta + C, \tag{4.70}$$

where the constant term C is given by

$$\begin{aligned} C &= -2[t\sum_{\langle ij\rangle} Q_f Q_\theta + t'\sum_{\langle i'j'\rangle} Q'_f Q'_\theta] + \sum_i \rho \\ &= -[4N_c t Q_f Q_\theta + 2N_c t' Q'_f Q'_\theta] + 2N_c\rho. \end{aligned} \tag{4.71}$$

The Helmholtz free energy per lattice site $\mathcal{E}$ is defined as

$$\mathcal{E} = -\frac{1}{2N_c\beta}\log Z, \tag{4.72}$$

where Z is the partition function, which is given by

$$\begin{aligned} Z &= \mathrm{Tr}\{\exp(-\beta\mathcal{H})\} \approx \mathrm{Tr}\{\exp(-\beta\mathcal{H}_f)\exp(-\beta\mathcal{H}_\theta)\exp(-\beta C)\} \\ &= \sum_{\phi_f\phi_\theta} \langle\phi_f| \otimes \langle\phi_\theta| \exp(-\beta\mathcal{H}_f)\exp(-\beta\mathcal{H}_\theta)\exp(-\beta C)|\phi_\theta\rangle \otimes |\phi_f\rangle \\ &= \sum_{\phi_f} \langle\phi_f| \exp(-\beta\mathcal{H}_f)|\phi_f\rangle \times \sum_{\phi_\theta} \langle\phi_\theta| \exp(-\beta\mathcal{H}_\theta)|\phi_\theta\rangle \times \exp(-\beta C) \\ &= Z_f \times Z_\theta \times \exp(-\beta C), \end{aligned} \tag{4.73}$$

where $\{|\phi_f\rangle\}$ and $\{|\phi_\theta\rangle\}$ are complete basis for the spinons and charges, respectively. The free energy can thus be expressed as

$$\mathcal{E} = -\frac{1}{2N_c\beta}\ln Z \approx \mathcal{E}_f + \mathcal{E}_\theta + \frac{C}{2N_c} \tag{4.74}$$

The free energy for the spinons is

$$\mathcal{E}_f = -\frac{1}{N_c}\sum_{\boldsymbol{k}} |\Gamma_f^{\boldsymbol{k}}|. \tag{4.75}$$

For the charges, we need to consider the condensed and disordered phase

separately. For the condensed phase, one has

$$\mathcal{E}_\theta = \frac{1}{2N_\mathrm{c}} \sum_{\boldsymbol{k}\neq 0} \sqrt{2U(|\Gamma_\theta^{\max}| - |\Gamma_\theta^{\boldsymbol{k}}|)}, \tag{4.76}$$

while for the disordered phase, we replace in the above equation $|\Gamma_\theta^{\max}|$ by $|\rho|$, and obtain

$$\mathcal{E}_\theta = \frac{1}{2N_\mathrm{c}} \sum_{\boldsymbol{k}} \sqrt{2U(|\rho| - |\Gamma_\theta^{\boldsymbol{k}}|)}. \tag{4.77}$$

4.3.6 Phase diagram

The free energy plots for the three solutions for a few typical values of t' are shown in Figure 4.2. In the case of a second order phase transition, the transition point is determined by the simultaneous vanishing of Δ_c and n_0. In Figure 4.2, this is the point connecting the red and black parts of the second order solution curve. On the other hand, if the lowest free energy point jumps to another solution before a second order transition is reached, one has a first order transition instead, the transition point of which is the point of jumping between the two solutions. With this in mind, we finally obtain the phase diagram plotted in Figure 4.3, where the antiferromagnetic transition line is also included for completeness. In Figure 4.4, a zoomed-in plot of the part of Figure 4.3 in the vicinity of the isotropic limit ($t' = t$) is plotted.

One finds that, for $t' \lesssim 1.005t$, the system undergoes a second-order phase transition (described by the transition line plotted in Figure 4.1) from the semimetal (SM) phase to a gapless spin-liquid phase (GLSL in Figure 4.3) upon increase of U/t; for $1.005t \lesssim t' \lesssim 1.019t$, the system first experiences the above-mentioned second-order phase transition from the SM to the GLSL (within the second order transition solution), and then a first-order phase transition to another gapless one of the chain solution [GLSL (Chain)]; for $1.019t \lesssim t' \lesssim 1.31t$, the second-order phase transition disappears and the system jumps directly from

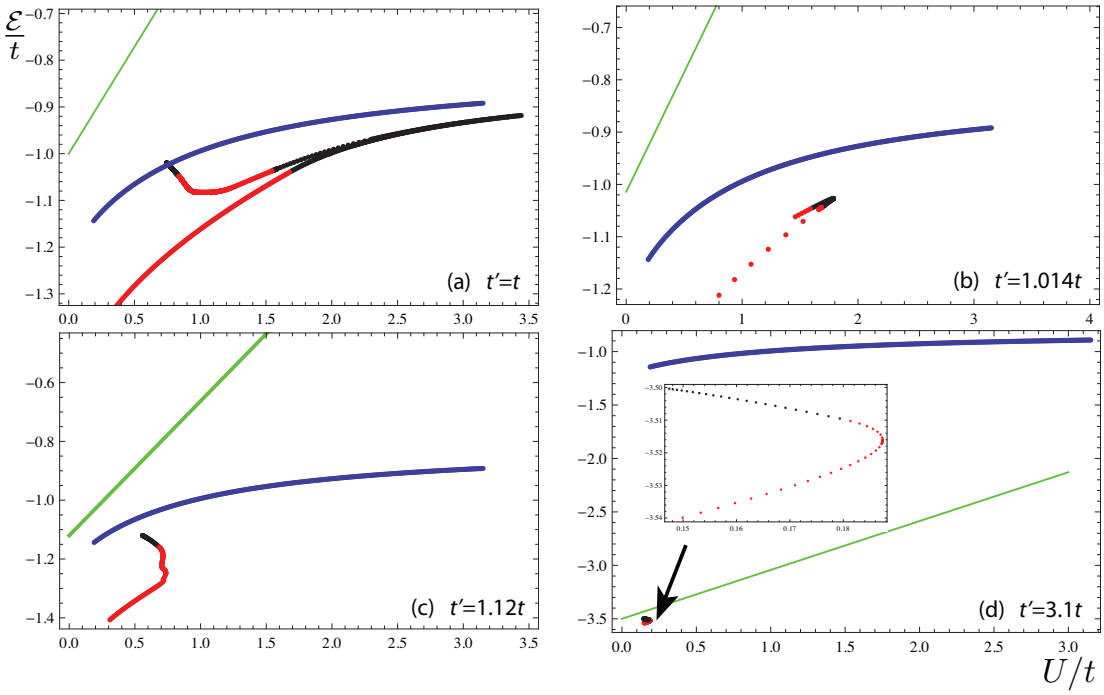

Figure 4.2: Plots of the free energy $\mathcal{E}$ against U for a few values of t'. Green, blue and black-red curves are for the Dimer, Chain and second-order solutions, respectively. For the second-order solution, the red and black parts of the curve correspond to the rotor-condensed and -disordered phases, respectively.

a SM phase to the GLSL (Chain) via a first order phase transition; finally, for $t' \gtrsim 1.31t$, the system undergoes a first-order phase transition from the SM [or band-insulating (BI)] phase to a gapped spin liquid of the dimer solution [GDSL (Dimer)]. The antiferromagnetic transition, which cuts the GLSL-GLSL (Chain) transition at $t' \lesssim 1.005t$, but which is otherwise well above the SM/BI-spin-liquid transitions described here, is not treated within the current slave-rotor description. As already mentioned, in principle, the antiferromagnetic transition may be described within a slave-rotor theory by reintroducing spin-charge correlations into the Hamiltonians (4.17a) [91]. Another possibility is discussed in Section (4.2).

For the isotropic case $t' = t$, our result of the second-order transition point $U_c/t \approx 1.68$ agrees with References [69, 71]. In this limit, the free-energy analysis indicates that the gapless SL of the second-order solution is the lowest while the gapped SL of the dimer solution is the highest in energy among the three solutions.

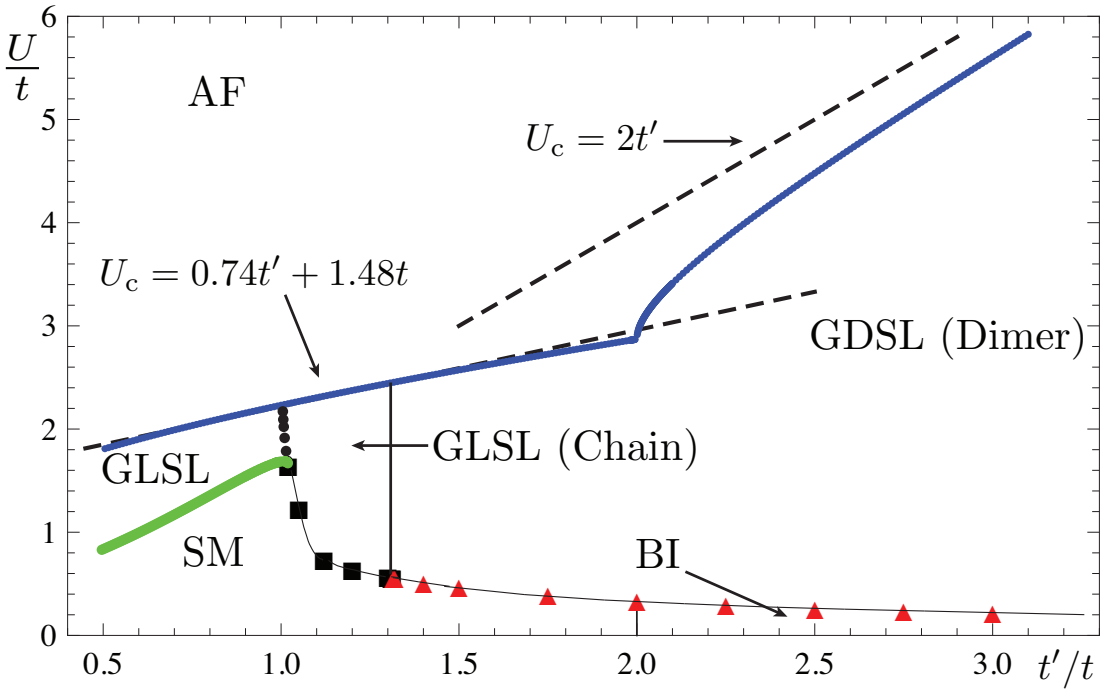

Figure 4.3: Mean-field phase diagram obtained for the anisotropic repulsive Hubbard model on the honeycomb lattice at zero temperature and half-filling. The upper thinner blue line delineates the antiferromagnetic phase, whereas the two linear functions (the dashed lines) for U_c are obtained from simple scaling arguments (see Section (3.1)). The lower thick green line indicates a second-order phase transition between the semi-metal (SM) and the gapless spin-liquid (GLSL), whereas the dotted lines are first-order transitions, which consist of three sections: the black round dots for $1.005 \lesssim t'/t \lesssim 1.02$ between the GLSL of the second-order solution and that of the chain solution [GLSL (Chain)], the black squares for $1.02 \lesssim t'/t \lesssim 1.31$ between the SM and the GLSL (chain) and, above $t'/t \simeq 1.31$, the red triangles between the SM [or band-insulator (BI)] and a gapped spin-liquid [GDSL (Dimer)] that consists of decoupled dimers on the bonds with t'. The curve across the black squares and red triangles is drawn to direct the eyes.

This is in contrast to the findings in References [73, 96], where a gapped SL was identified as the true ground state. However, only an upper bound of the free energy of the dimer solution is provided by our free energy analysis. This is especially the case in the isotropic limit, in which a discrimination among the three hopping parameters is unphysical. Indeed, possible kinetic dimer terms (e.g. resonating dimer moving around a hexagon) could lower the energy of the gapped SL of the dimer solution [97]. At a general value of t', the free energies

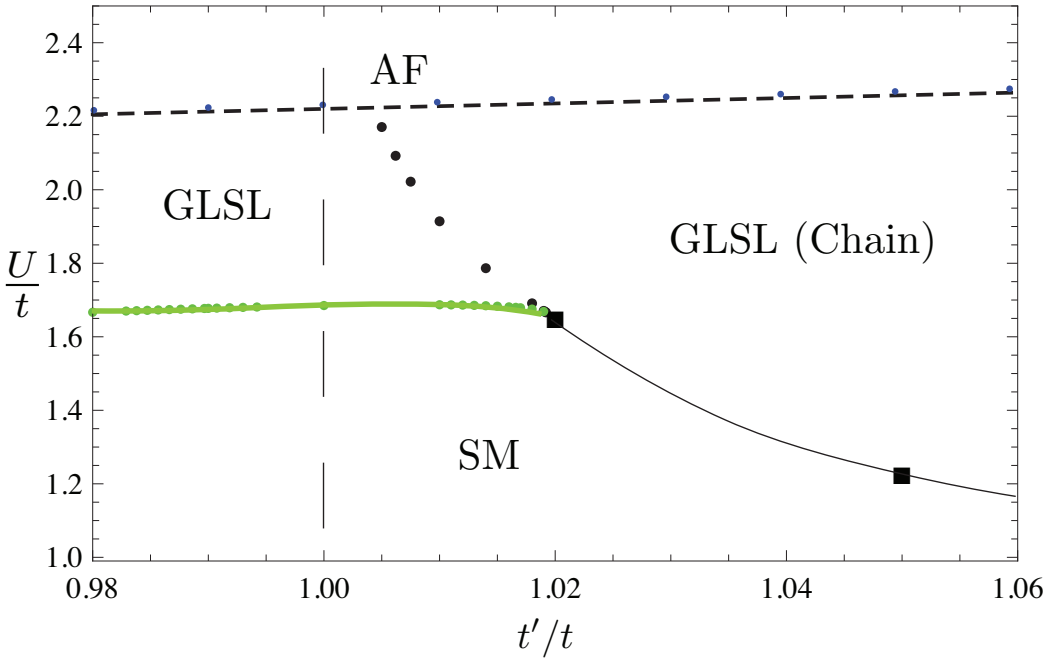

Figure 4.4: Zoom on the phase diagram in the vicinity of $t' = t$. For the notation and meaning of the symbols, refer to Figure 4.3. The dashed vertical line denotes the isotropic limit $t' = t$.

are modified by these terms such that they are adiabatically connected to the (also modified) isotropic case. Furthermore, the gapless chain solution may be unstable to an infinitesimal interchain coupling that, in the context of the square lattice, is known to open a spin gap [98]. An analysis of kinetic dimer terms and the stability of the chain solution is, however, beyond the scope of this thesis.

4.3.6.1 Relation with the effective Hamiltonian

It is clear from the phase diagram (4.3) that the gapped spin-liquid phase of the dimer solutions dominates the phase space in the large-t' limit. In this limit, nearest-neighboring sites connected by $\boldsymbol{c}_1$ form dimers, which structure dominates the physical properties of the system, and which is weakly perturbed by the inter-dimer-super-exchange interaction $\frac{4t^2}{U}$. This phase can be identified with the eigen-phase of the $\mathbb{S}^x$ in the effective Hamiltonian (3.162), which has spin-singlets on each and every bond along $\boldsymbol{c}_1$. Both of the two phases are described by dimers,

and the spin-spin correlation in both cases are expected to decay exponentially. A further hint at the identity of the two phases comes from the excitation gap. The antiferromagnetic transition line plotted in Figure 3.1 asymptotically approaches the line $U_c = 2t'$ in the large-t' limit. Taking this asymptotic relation literally, one would conclude that, in the effective model (3.162), the energy gap between the singlet and the triplet states is given by $\frac{4t'^2}{U} = 2t'$ in the vicinity of the transition line. On the other hand, for the Dimer solution described in Section 4.3.4.2, the band gap in the spinon channel is given by $2(t'Q'_f - 2tQ_f) = t'$ [see Equation (1.32)], with $Q'_f = 0.5$ and $Q_f = 0$ as indicated in Equations (4.65) and (4.66). While the numerical factors are different, the two energy gaps agree on the functional form, i.e. they both depend on t' alone, and not on U or t, indicating the possibility that the two energy gaps are of the same origin.

As mentioned before, the true ground state is probably that of resonating dimers (singlets) moving around the hexagons, which is a special case of the short range resonating valence-bond (RVB) state [74–76]. The transition between the spin-liquid and the antiferromagnetic phases will then be that of the quantum Ising model, as described in References [88, 89].

5

Pairing transition in the bilayer honeycomb lattice

Following the isolation of monolayer graphene sheets, the synthesis of multilayer graphene has triggered the ongoing wave of investigation of such multilayer honeycomb lattice system [13, 99–101]. This is driven in part by the desire to make graphene-based materials with a tunable energy gap, which can be opened in bilayer graphene by a potential difference between the two layers, and also by the fact that bilayer graphenes are a class of materials that are interesting in their own right.

There are two typical ways of stacking for bilayer graphene, with different band structures and electronic properties. Most of the research interests have been attracted toward the AB-stacked bilayer graphene [13,99–103], in which the sub-lattice A of the upper layer is directly above sub-lattice B of the lower one, while the sites of the sub-lattice B in the upper layer are above the hexagon centers of the lower layer. This is the natural stacking found in graphite. As has been briefly mentioned in Section 1.3.3.2, the additional inter-layer nearest-neighbor hopping amplitude changes the linear dispersion of the monolayer graphene at the K and K$'$ points to parabolic, mimicking that of massive Dirac points. The Berry phase of these massive Dirac points is $\pm 2\pi$ instead of $\pm\pi$ for electrons in monolayer graphene. The sign depends on the valley K and K$'$ in both cases. More importantly, the density of states at these points is nonzero instead of linearly vanishing as in the monolayer counter part [13, 35, 102]. Thus the interaction effects are more prominent in AB-stacked bilayer graphene than in monolayer graphene. This renders the AB-stacked bilayer graphene a more plausible superconducting candidate than its monolayer counterpart, the latter of which requires

the proximity effect when being inserted between two layers of superconducting materials [104], or doping [105], in order to superconduct. By including the inter-layer next nearest neighbor hopping between the sub-lattice B of the upper layer and the sub-lattice A of the lower layer, which is comparable in magnitude to the interlayer nearest-neighbor-hopping in bilayer graphene[1] [35], the Fermi surface becomes anisotropic at low energies. This phenomenon is called trigonal-warping [106]. The Fermi surface at each valley splits into four small pockets for energies $\leq$1meV, which are linear at the zero energy, corresponding to four Dirac points. The Berry phases at these Dirac points are $\pm 1 \times \{\pi, \pi, \pi, -\pi\}$ [107], summing up to $\pm 2\pi$ for the two valleys. By twisting the two layers with respect to each other along the axis perpendicular to the lattice plane, we can have the interesting phenomenon of merging of Dirac points [107], similar to the topological Lifshitz transition in the anisotropic monolayer honeycomb lattice, which we have discussed in Section 1.2.2.

The AA-stacking is another way of constructing bilayer graphenes, which so far has received limited theoretical attention [108–115]. In this stacking, the sub-lattices A and B in the upper layer are directly above their counter parts in the lower layer, as illustrated in Figure 5.1. Although it is not the natural stacking, AA-stacking of bilayer graphene is often encountered in growing graphene [116]. It has been found that bilayer graphene tends to exist in this stacking, and is very difficult to distinguish from monolayer graphene using scanning tunneling microscopy [117]. The number of lattice sites per unit cell is doubled as compared to the monolayer case. The reciprocal lattice structure is identical to that in the monolayer case, which is displayed in Figure 1.1(b). Due to its in-plane symmetries that are identical to those of the monolayer graphene, the band structure displayed by the AA-stacked bilayer graphene resembles two copies of the monolayer graphene band structure [112, 115]. By including the inter-layer nearest-neighbor hopping amplitude, which acts as effective chemical potentials, the degeneracy of the two copies of monolayer graphene bands can be lifted. This will be discussed in detail in the coming sections.

[1] In graphite, the interlayer nearest-neighbor hopping is ~ 0.4eV, while the interlayer next-nearest-neighbor hopping is ~ 0.3eV. The intralayer nearest-neighbor-hopping is ~ 3eV.

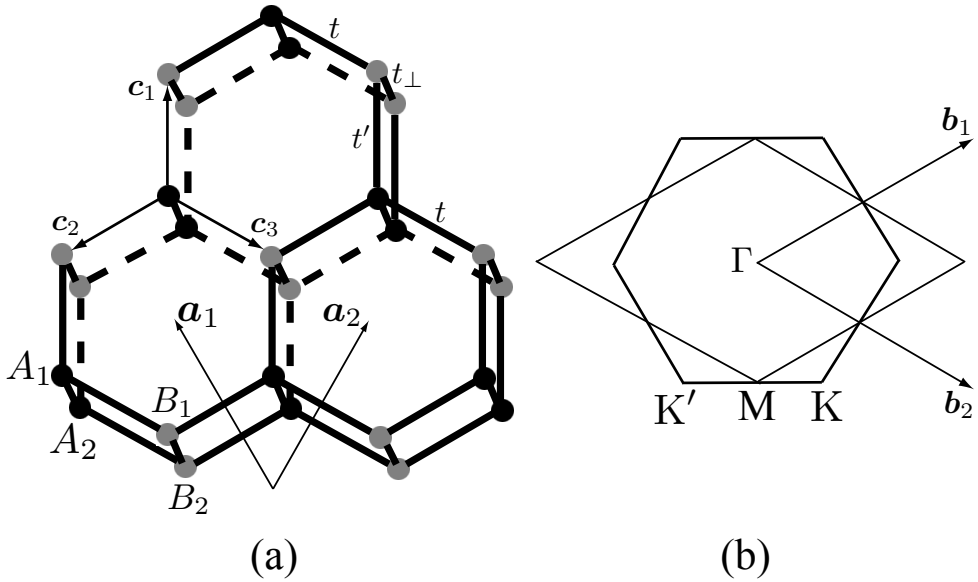

Figure 5.1: (a) The AA-stacking bilayer honeycomb lattice. One layer of honeycomb lattice is directly placed on top of the other. The subscript of A_1, B_2 etc. is the layer index. The two kinds of intra-layer nearest-neighbor hopping amplitudes t and t' are described in Equation (1.29). The additional parameter $t_\perp$ introduced here is the interlayer nearest-neighbor hopping amplitude. Please see the caption of Figure 1.1(a) for the meanings of the other designations. (b) The reciprocal space structure of the AA-stacking bilayer honeycomb lattice, which is identical to Figure 1.1(b).

5. PAIRING TRANSITION IN THE BILAYER HONEYCOMB LATTICE

In this chapter, we consider the pairing transition in an AA-stacked bilayer honeycomb lattice. We have the optical lattice system in mind. Considering that the AA-stacking bilayer is simply two layers of the same crystal structure with no in-plane mismatch, it should not be difficult to construct such an optical potential, especially given the well established monolayer constructions [32, 55]. One such possibility would be using a beam-splitter to create two vertically separated identical laser beams out of one, three such configurations can then be used to construct the AA-stacked bilayer honeycomb optical lattice following, e.g., the setup illustrated in Figure 1.3(a). We consider again the situation described by Equation (1.29) with the two kinds of intra-layer hopping amplitudes t and t', as indicated in Figure 5.1(a). For interlayer hoppings, we consider only those between nearest neighbors, which amplitude will be denoted as $t_\perp$. Doping, which shifts the Fermi level, is introduced as an additional ingredient.

The comprehension of the noninteracting tight-binding band structure is crucial for the understanding of our results, so it will be studied as the first step. We then study the mean-field decoupled system being doped to the Dirac points, which are shifted away from zero energy by the inter-layer hopping amplitude. In the limit of large inter-layer hopping, the critical interaction strength for the pairing transition is found to be doubled as compared to the monolayer case. Finally, we study in detail the mean-field phase space of two typical cases representing the two classes $t' < 2t$ and $t' > 2t$. The correlation between the size of the Fermi surface and the magnitude of the order parameter, and that between the finiteness of the size of the Fermi surface and the existence of a finite critical interaction strength are found.

5.1 Model

5.1.1 The kinetic Hamiltonian

The kinetic part of the model is

$$\mathcal{H}_0 = \left[-t \sum_{\langle ij \rangle \sigma l} a^{l\dagger}_{i\sigma} b^{l}_{j\sigma} - t' \sum_{\langle i'j' \rangle \sigma l} a^{l\dagger}_{i'\sigma} b^{l}_{j'\sigma} - t_\perp \sum_{(ij)\sigma} (a^{1\dagger}_{i\sigma} a^{2}_{i\sigma} + b^{1\dagger}_{j\sigma} b^{2}_{j\sigma}) \right] + \text{H.c.}, \tag{5.1}$$

where $t_\perp$ is the inter-layer nearest-neighbor hopping, and the superscript $l = 1, 2$ is the layer index. We consider the anisotropic nearest-neighbor hopping amplitudes t and t' within each layer, which are defined in Equation (1.29), and are shown in Figure 5.1(a). In Equation (5.1), $\langle ij \rangle$ and $\langle i'j' \rangle$ are in-plane nearest neighbors with hopping amplitudes t and t', respectively, while (ij) is over the in-plane nearest neighbors in an arbitrary but fixed direction. In the case of (ij), each "lattice site" consists of two interlayer nearest neighbors. All other symbols have the same meaning as those in the Hamiltonian (1.14). All hopping parameters considered in this article are greater than or equal to zero. But as noted later, our analysis is valid for the case of $t' < 0$ and $t_\perp < 0$ as well.

Due to the particular mean-field order parameter that we look at in this chapter, which involves pairing, the momentum space basis that we choose to diagonalize $\mathcal{H}_0$ is

$$\Psi^\dagger_{\boldsymbol{k}} = \left(a^{1\dagger}_{\boldsymbol{k}\uparrow}, a^{1}_{-\boldsymbol{k}\downarrow}, b^{1\dagger}_{\boldsymbol{k}\uparrow}, b^{1}_{-\boldsymbol{k}\downarrow}, a^{2\dagger}_{\boldsymbol{k}\uparrow}, a^{2}_{-\boldsymbol{k}\downarrow}, b^{2\dagger}_{\boldsymbol{k}\uparrow}, b^{2}_{-\boldsymbol{k}\downarrow} \right). \tag{5.2}$$

This so called Nambu space effectively doubles the Hilbert space by bringing the particle and hole spaces into equal footing, which is precisely what is needed when considering the pairing transition. The resulting energy bands are

$$E^{\boldsymbol{k}}_j = \pm |\gamma^{\boldsymbol{k}}_{t'}| \pm t_\perp, \tag{5.3}$$

where j labels the different energies, and

$$|\gamma_{t'}^{\boldsymbol{k}}| = \sqrt{t'^2 + 4t^2\cos^2 x + 4t't\cos x\cos y}, \tag{5.4}$$

where $x = \sqrt{3}ak_x/2$ and $y = 3ak_y/2$, and a is the honeycomb lattice constant. In the absence of pairing, each of the above bands is doubly degenerate due to the doubling of the degrees of freedom. Notice that changing the sign of t' in Equation (5.4) is equivalent to the translation $y \to y+\pi$, while changing the sign of $t_\perp$ in Equation (5.3) does not change the band structure at all.

The basis (5.2) amounts to particle-hole-transforming the spin-$\downarrow$ particles, thus the eigen-energies of the spin-$\downarrow$ particles acquire an overall minus sign. This is not obvious at half-filling, because the energies are symmetric with respect to zero in this case, as can be seen in Equations (5.3). Only when the chemical potential term

$$-\mu\sum_{il\sigma} n_{i\sigma}^{l} \tag{5.5}$$

is taken into account, we have different doped energy levels for the spin-$\uparrow$ and spin-$\downarrow$ particles as

$$\begin{aligned} E_j^{\boldsymbol{k}} - \mu &: \text{ for spin-}\uparrow\text{ particles,} \\ E_j^{\boldsymbol{k}} + \mu &: \text{ for spin-}\downarrow\text{ particles,} \end{aligned} \tag{5.6}$$

because the Fermi surfaces of the two kinds of particles move in opposite directions. However, these purely formal differences do not affect the physics, which is the same for spin-$\uparrow$ and spin-$\downarrow$ particles.

5.1.1.1 Uncorrelated tight-binding band structure

The band structure is obtained in Equation (5.3). The particular case of $t_\perp = 0$, in which the two layers decouple into two independent sheets with dispersion relations $E = \pm|\gamma_{t'}^{\boldsymbol{k}}|$, has been analyzed in Section (1.2.1). We repeat it here for

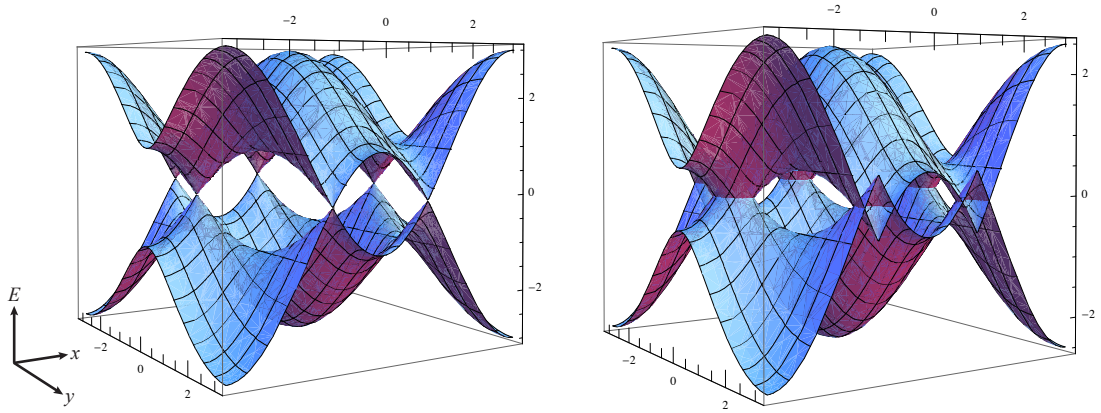

(a) $t' = t,\ t_\perp = 0$ (b) $t' = t,\ t_\perp = 0.5t$

Figure 5.2: The band structure in units of t close to zero energy for $t' = t$ and (a) $t_\perp = 0$ and (b) $t_\perp = 0.5t$. Notice the upward and downward shift for the lower and upper bands, respectively, in the case of $t_\perp = 0.5t$. This is in accordance with Equation (5.3). Note that these are plotted in the rescaled coordinates x and y described in Equation (1.11). The bands that are far from zero energy are not shown here.

the sake of discussion. Remember that for $t' < 2t$, the band structure features the so-called Dirac points at zero energy, at which the upper (positive) and lower (negative) bands touch at conical intersections, while for $t' > 2t$, there are no more Dirac points, but instead a band gap opens at the center of the bands. At half-filling, the former phase is a semi-metal, while the latter is a band-insulator. The band gap in the latter phase is $2(t' - 2t)$ centering at zero, and the top and bottom of the bands are given by $\pm(t' + 2t)$ for both phases. The width of each band in the semi-metallic and the band-insulating phases are thus $(t' + 2t)$ and $4t$, respectively.

Switching on $t_\perp$, the degeneracy of the energy bands is lifted according to Equation (5.3), which is illustrated in Figure 5.2 for the energy bands close to zero energy for the case of $t' = t$.

By varying t', $t_\perp$ and μ, the model (5.1) displays a variety of phases, which is the main topic of this section. We discuss separately the two classes $t' < 2t$ and $t' > 2t$. We consider positive half of the bands as an example. The negative bands are obtained from the particle-hole symmetry of the band structure. In Figure 5.4, we plot the phase diagrams for the cases of $t' = t$ and $t' = 3t$, representing

the two classes $t' < 2t$ and $t' > 2t$, respectively.

The case of $t' < 2t$ The phase diagram for $t' < 2t$, represented by the particular case $t' = t$, is plotted in Figure 5.4(a). The most salient feature of the band structure in this case is the existence of the Dirac points. With nonzero $t_\perp$, these points are no longer at zero energy, but are shifted by $\pm t_\perp$ according to Equation (5.3). The case of $t_\perp = 0$ has been discussed previously. For $0 < t_\perp \leq (t' + 2t)/2$, as can be deduced from the band structure (5.3), the Dirac points of the bands $\pm|\gamma^{\boldsymbol{k}}_{t'}| + t_\perp$ are submerged by the bands $\pm|\gamma^{\boldsymbol{k}}_{t'}| - t_\perp$ and vice versa, a case that is illustrated in Figure 5.3(a). Thus the semi-metallic phase is absent for this case, because a nonzero density of states is provided by the bands that do not take part in the formation of the Dirac points at $E = t_\perp$, and the system is thus metallic. For $t_\perp > (t' + 2t)/2$, the Dirac points no longer overlap with the finite surfaces of the other bands, as illustrated in Figure 5.3(b). From Equations (5.6), we see that in order to dope the system to the Dirac points, one needs $\mu = t_\perp$. When the Fermi level is at these points, the system assumes a semi-metallic phase, which is denoted by the dot at the origin as well as the thick line with $t_\perp = \mu > (t' + 2t)/2$ in Figure 5.4(a).

We now consider the case of $t' = t$ and $t_\perp = 4t$ as an explicit example, the band structure of which (for $k_x = 0$) is shown in the bottom panel of Figure 5.7. The Dirac points of the bands $\pm|\gamma^{\boldsymbol{k}}_{t'}|$ are now at the energy $t_\perp = 4t$, while the top and bottom of these bands are at energies $t_\perp + t' + 2t = 7t$ and $t_\perp - t' - 2t = t$, respectively. Thus for $0 < \mu < t$ as well as $\mu > 7t$, the Fermi level lies in band gaps, and so the system is a band-insulator, while for $t < \mu < 7t$ with the exception of $\mu = 4t$, the Fermi level lies within a band, and the system is a metal. At $\mu = 4t$, the Fermi level is at the Dirac points, and the system is a semi-metal, as discussed before. This case is denoted by the horizontal dotted line at $t_\perp = 4t$ in Figure 5.4(a). Other values of $t_\perp$ can be analyzed in a similar way, from which one obtains the phase diagram Figure 5.4(a).

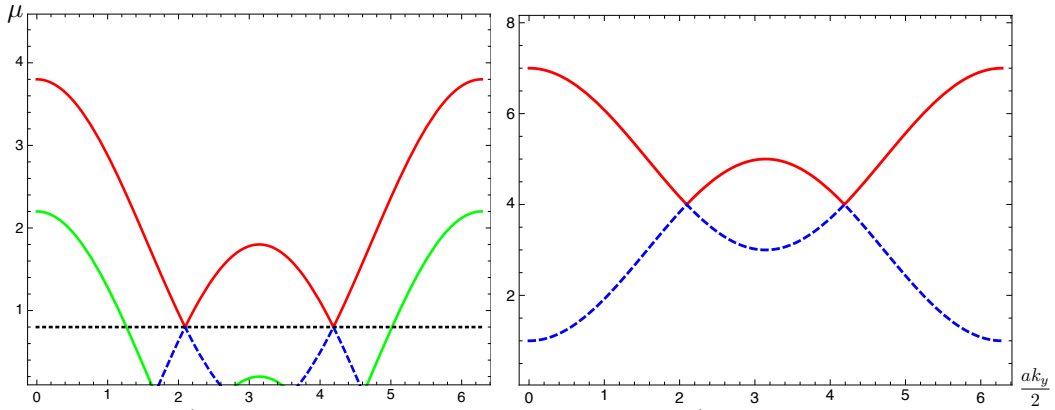

(a) $t' = t, t_\perp = 0.8t$ (b) $t' = t, t_\perp = 4t$

Figure 5.3: The uncorrelated band structures Equation (5.3) along the line $k_x = 0$ are plotted for $t' = t$ and (a) $t_\perp = 0.8t$ and (b) $t_\perp = 4t$, in the rescaled coordinate $\frac{ak_y}{2}$. The energy is depicted in units of t. The Dirac points in (a), which are marked by the horizontal dotted line, are submerged by the other band, while those in (b) stand out from the other bands. Note that only the parts with $\mu > 0$ are plotted. The parts with $\mu < 0$ are the mirror image with respect to the horizontal axis.

The case of $t' > 2t$ The case of $t' = 3t$ is plotted in Figure 5.4(b), representing the class of $t' > 2t$. As discussed before, in this case a band gap, given by $2(t'-2t)$, occurs at the M point at the center of the bands $\pm|\gamma_{t'}^{\boldsymbol{k}}|$. Naturally, there is no semi-metallic phase due to the absence of the Dirac points.

Like in the previous section, here we consider the particular case of $t' = 3t$ and $t_\perp = 2.5t$ as an example. The center of the bands $\pm|\gamma_{t'}^{\boldsymbol{k}}| + t_\perp$ is at the energy $t_\perp = 2.5t$, which coincides with the center of the band gap of magnitude $2(t' - 2t) = 2t$. The top of the band $|\gamma_{t'}^{\boldsymbol{k}}| + t_\perp$ is at $t' + 2t + t_\perp = 7.5t$, while the bottom of $-|\gamma_{t'}^{\boldsymbol{k}}| + t_\perp$ is at $-t' - 2t + t_\perp = -2.5t$ in the negative half of the band structure. Furthermore, part of the band $|\gamma_{t'}^{\boldsymbol{k}}| - t_\perp$, the top and bottom of which are at the energy $t' + 2t - t_\perp = 2.5t$ and $t' - 2t - t_\perp = -1.5t$, respectively, also extends to the positive half of the band structure. Thus for the particular case under consideration, the two bands $|\gamma_{t'}^{\boldsymbol{k}}| - t_\perp$ and $-|\gamma_{t'}^{\boldsymbol{k}}| + t_\perp$ overlap in an energy window of $0 < E < 1.5t$. To summarize, for $0 < \mu < 2.5t$ and $3.5t < \mu < 7.5t$, the Fermi level lies within a band or bands, and system is a metal, while for $2.5t < \mu < 3.5t$ and $\mu > 7.5t$, the Fermi level lies within band gaps, and the system is band-insulating. This case is denoted by the horizontal dotted line at

$t_\perp = 2.5t$ in Figure 5.4(b), and is plotted in the lower panel in Figure 5.8. Other values of $t_\perp$ can be analyzed in a similar fashion, which gives rise to the phase diagram in Figure 5.4(b).

5.1.2 The interaction term

Here we consider the attractive onsite interaction term

$$\mathcal{V} = -U \sum_{il} (n^l_{i\uparrow} - \frac{1}{2})(n^l_{i\downarrow} - \frac{1}{2}), \tag{5.7}$$

where as before, $U > 0$ is the interaction strength.

The order parameter under consideration is

$$\Delta = \langle \alpha^l_{i\downarrow} \alpha^l_{i\uparrow} \rangle, \tag{5.8}$$

where $\alpha = a, b$ denote the annihilation operators, and l is the layer index. This order parameter describes the onsite pairing between a spin-$\uparrow$ particle and a spin-$\downarrow$ particle. The condensation of these pairs gives rise to a superfluid phase or singlet conductivity if the operators α describe charged fermions. It is assumed to be translational invariant, which, when transformed into the momentum space, means the pairing between crystal momenta $\boldsymbol{k}$ and $-\boldsymbol{k}$. We use this order parameter to decouple the second order term in the expanded interaction term $\mathcal{V}$:

$$\begin{aligned} n_{i\uparrow} n_{i\downarrow} &= \alpha^\dagger_{i\uparrow} \alpha^\dagger_{i\downarrow} \alpha_{i\downarrow} \alpha_{i\uparrow} \\ &\approx \Delta^* \alpha_{i\downarrow} \alpha_{i\uparrow} + \Delta \alpha^\dagger_{i\uparrow} \alpha^\dagger_{i\downarrow} - |\Delta|^2. \end{aligned} \tag{5.9}$$

In the following, we will take Δ to be real, which can be guaranteed by a global

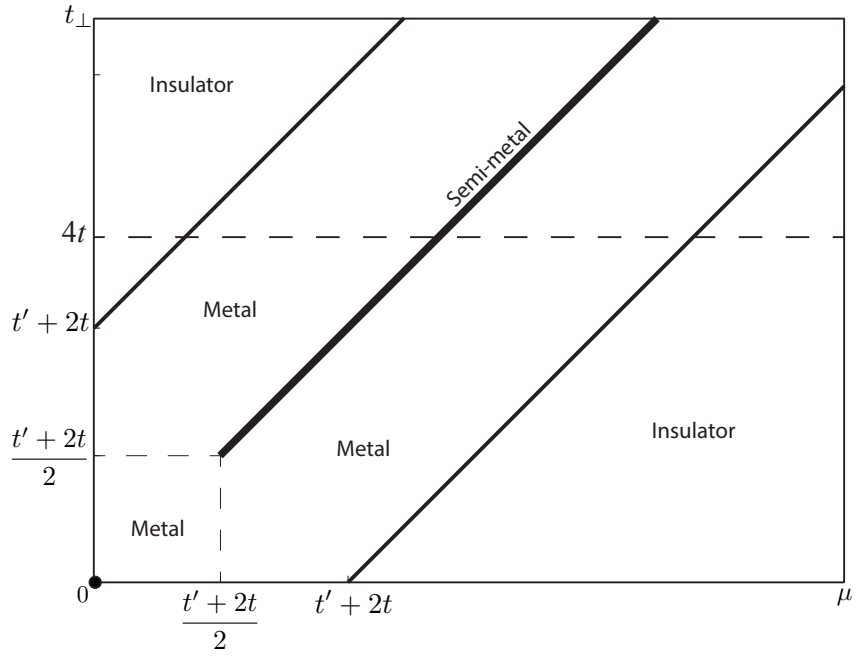

(a)

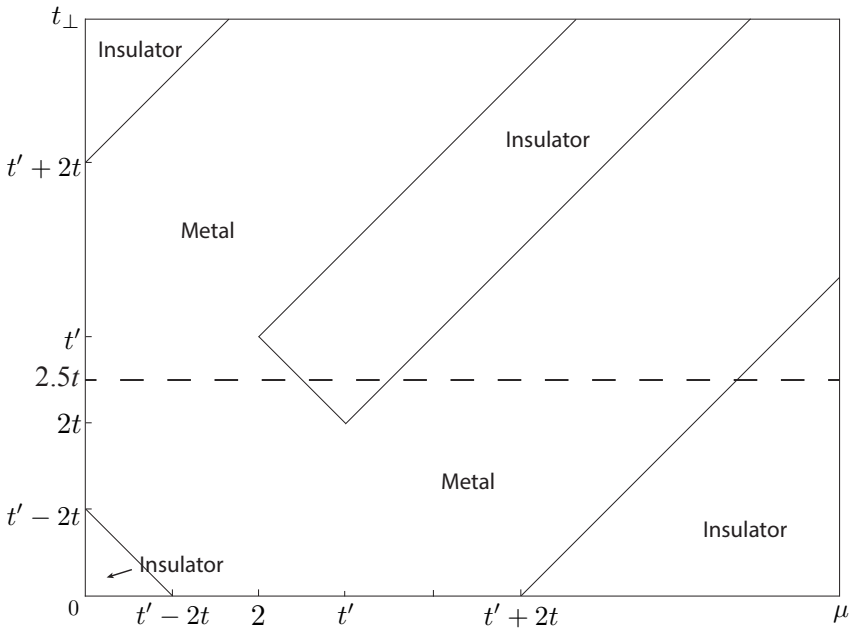

(b)

Figure 5.4: (a) Uncorrelated phase diagram for $t' < 2t$ ($t' = t$ for this particular plot). The semi-metallic phase consists only of the isolated dot at $t_\perp = \mu = 0$ and the thick line, defined by $t_\perp = \mu$ for $t_\perp > \frac{t'+2t}{2}$. The horizontal dashed lines marks $t_\perp = 4t$, corresponding to the case plotted in Figure 5.7. (b) Uncorrelated phase diagram for $t' > 2t$ ($t' = 3t$ for this particular plot). The horizontal dashed lines marks $t_\perp = 2.5t$, corresponding to the case plotted in Figure 5.8.

gauge transformation [1]. The other terms in the expanded $\mathcal{V}$ are proportional to

$$-\frac{1}{2}\left(n^l_{i\uparrow}+n^l_{i\uparrow}\right)+\frac{1}{4}. \tag{5.10}$$

The first term can be taken care of by renormalizing the chemical potential, while the constant term $(\frac{1}{4})$ can be dropped. The decoupled interaction term hence is

$$\mathcal{V}_{\mathrm{MF}}=-U\sum_{il}\left(\Delta^*\alpha^l_{i\downarrow}\alpha^l_{i\uparrow}+\Delta\alpha^{l\dagger}_{i\uparrow}\alpha^{l\dagger}_{i\downarrow}-|\Delta|^2\right). \tag{5.11}$$

5.1.3 Mean-field equations

In terms of the mean-field decoupled interaction term (5.11), the mean-field eigenenergies are

$$E^{\boldsymbol{k}}_j(\Delta)=\pm\sqrt{U^2\Delta^2+(|\gamma^{\boldsymbol{k}}_{t'}|\pm t_\perp\pm\mu)^2}, \tag{5.12}$$

where j again labels the different energy eigenvalues. As mentioned previously, the bands with $-\mu$ and $+\mu$ are for spin-$\uparrow$ and spin-$\downarrow$ particles, respectively. The Dirac points are now located at the energies $\pm\sqrt{U^2\Delta^2+(t_\perp)^2}$, and the effective speed of light is rescaled as

$$\frac{t_\perp}{\sqrt{U^2\Delta^2+(t_\perp)^2}}v_{\mathrm{F}}, \tag{5.13}$$

where v_{F} is the Fermi velocity of the particles in the half-filled monolayer honeycomb lattice [see Equation (1.22)].

The Helmholtz free energy per lattice site is given by

$$F=-\frac{1}{4N_{\mathrm{c}}\beta}\log Z, \tag{5.14}$$

[1] The complex form of Δ is useful when it comes to describing the low-energy excitations of the system, which are generated precisely by the local fluctuation of the phase of the complex Δ. These will not be discussed in this thesis.

where Z is the partition function

$$Z = \mathrm{Tr}\left\{\exp\left(-\beta\mathcal{H}_{\mathrm{MF}}\right)\right\}, \tag{5.15}$$

in terms of $\beta = (k_B T)^{-1}$ with k_B and T being the Boltzmann constant and absolute temperature, respectively, and

$$\mathcal{H}_{\mathrm{MF}} = \mathcal{H}_0 + \mathcal{V}_{\mathrm{MF}} - \mu \sum_{il\sigma} n^l_{i\sigma}. \tag{5.16}$$

In the $T \to 0$ and continuum limits, it can be shown that the free energy is given by

$$F = \int_{\diamond} \frac{dxdy}{8\pi^2} \sum_j \Theta\left(-E^{\boldsymbol{k}}_j(\Delta)\right) E^{\boldsymbol{k}}_j(\Delta) + U\Delta^2, \tag{5.17}$$

up to constant terms, where the $\diamond$ subscript means that the integration is over the FBZ, and $x = \frac{\sqrt{3}ak_x}{2}$ and $y = \frac{3ak_y}{2}$. Here $\Theta(x)$ is the Heaviside function, with

$$\Theta(x) = \begin{cases} 1 \text{ if } x > 0 \\ \frac{1}{2} \text{ if } x = 0 \\ 0 \text{ if } x < 0 \end{cases} \tag{5.18}$$

The minimization of Equation (5.17) with respect to Δ gives the value of the order parameter.

To obtain the critical interaction strength (U_{c}), we calculate $\partial F/\partial\Delta$, where F is given in Equation (5.17). Setting the resulting expression to be 0, and taking the limit $\Delta \to 0$, we obtain the equation

$$U_{\mathrm{c}} = \Big(\int_{\diamond} \frac{dxdy}{16\pi^2} \sum_j \frac{\Theta\left(-E_j(\Delta)\right)}{\left|E_j(\Delta)\right|}\Big|_{\Delta\to 0} \Big)^{-1}. \tag{5.19}$$

Similar to the antiferromagnetic transition in the square lattice, which was discussed in Section 3.1.2.1, U_{c} is zero as long as a finite size Fermi surface exists,

because of the diverging integrand $\frac{1}{|E_j|}$ on the right-hand-side of Equation (5.19). In other words, as long as a finite size Fermi surface exists, the paring of spins occurs at an infinitesimal U. On the other hand, if the Fermi surface is composed of isolated Dirac points, a finite U_c exists, since $\frac{1}{|E_j|}$ diverges like $\frac{1}{q}$, where q is the distance in the reciprocal space relative to a Dirac point, as demonstrated in Equation (1.25). This divergence is exactly canceled by the linearly vanishing two-dimensional Jacobian, thus resulting in a finite integration result. In the insulating phase, there is no more diverging integrand, thus a finite value of U_c can be calculated using Equation (5.19) as well. Therefore one expects finite values for U_c in the parameter space corresponding to only the semi-metallic and band-insulating phases of the uncorrelated system.

5.1.4 Relation to the antiferromagnetic order in the repulsive model

The attractive model at half-filling ($\mu = 0$) is related to the repulsive one via the partial particle-hole-transformation

$$\begin{aligned} a^{1\dagger}_{i\downarrow} &\to -a^{1}_{i\downarrow}, \\ a^{2\dagger}_{i\downarrow} &\to a^{2}_{i\downarrow}, \\ b^{1\dagger}_{i\downarrow} &\to b^{1}_{i\downarrow}, \\ b^{2\dagger}_{i\downarrow} &\to -b^{2}_{i\downarrow}, \end{aligned} \tag{5.20}$$

while spin-$\uparrow$ operators remain unchanged. It is easy to check that under this transformation, the only change in the Hamiltonian is the sign of the interaction strength.

Under this transformation, the order parameter becomes

$$\langle \alpha^{l}_{i\downarrow} \alpha^{l}_{i\uparrow} \rangle \to \pm \langle \alpha^{l\dagger}_{i\downarrow} \alpha^{l}_{i\uparrow} \rangle, \tag{5.21}$$

where the sign on the right hand side is determined by its sub-lattice and layer indices according to Equation (5.20). In contrast to the attractive model, the

order parameter on the right hand side of Equation (5.21) reflects a singlet pairing of electron-hole pairs that may be identified with excitonic condensation. The right hand side of Equation (5.21) is the expectation value of

$$S_- = S_x - iS_y, \tag{5.22}$$

where S_x and S_y are the x- and y-components of the spin operator $\boldsymbol{S}$, which is defined as

$$\boldsymbol{S} = \frac{1}{2}\boldsymbol{\psi}^\dagger \boldsymbol{\tau} \boldsymbol{\psi} \text{ with } \boldsymbol{\psi} = \left(c_\uparrow^\dagger \; c_\downarrow^\dagger\right), \tag{5.23}$$

where τ are the Pauli matrices (3.40). The z-component of $\boldsymbol{S}$ is

$$S_z = \frac{1}{2}\left(n_\uparrow - n_\downarrow\right). \tag{5.24}$$

The expectation value of the z-component is clearly proportional to the anti-ferromagnetic order parameter (3.4). The conclusion here is that the pairing order parameter (5.8) is intimately related to the anti-ferromagnetic order parameter (3.4) via partial particle-hole-transformation and rotation in the operator space [111]. Notice the signs of the order parameter on the right-hand-side of Equation (5.21), which changes from one site to its nearest neighbors, hinting at staggered magnetization. The critical interaction strength that we obtained from Equation (5.19) for the case of $t_\perp = 0$, $t' = t$ and $\mu = 0$ (i.e. the monolayer symmetric honeycomb lattice at half-filling) is $U_\mathrm{c} \approx 2.23t$, agreeing with our result in Section (3.1) and that in Reference [22].

5.2 Results

In this section, we study the mean-field phase diagrams of the system with onsite attractive interactions (5.7), which is mean-field decoupled in Equation (5.11). The discussion will be based on the uncorrelated phase diagrams, which have been studied in Section 5.1.1.1. In the following sections, the values of Δ are

obtained by minimizing Equation (5.17), while U_c are the solutions of Equation (5.19). We first study the critical interaction strength as a function of $t_\perp$ in the case where the honeycomb lattice is doped to the Dirac points, which are at the energies $\pm t_\perp$, and then study the two typical mean-field phase diagrams of $t' < 2t$ and $t' > 2t$ in detail.

5.2.1 Bilayer honeycomb lattice doped to the Dirac points

In this section we consider the case where $t' < 2t$, in which case one has Dirac points at $\mu = t_\perp$. As discussed before, the Dirac points are submerged by finite Fermi surfaces if $0 < t_\perp \leq (t' + 2t)/2$, in which case the system doped to the Dirac points of one set of bands is covered by the Fermi surface and the associated nonzero density of states of another band, so that the critical U is zero according to the discussion following Equation (5.19). For $t_\perp = 0$ or $t_\perp > (t' + 2t)/2$, the Dirac points are isolated. With $\mu = t_\perp$ the system is doped to the Dirac points, so that it assumes a semi-metallic phase. As discussed previously following Equation (5.19), the critical U is finite at these Dirac points.

Using Equation (5.19) to calculate the critical U for the semi-metallic phase, one has

$$U_c = \left(\int_\diamond \frac{dxdy}{16\pi^2} \left(\frac{2}{|\gamma_{t'}^{\boldsymbol{k}}|} + \frac{1}{\left||\gamma_{t'}^{\boldsymbol{k}}| - 2t_\perp\right|} + \frac{1}{\left||\gamma_{t'}^{\boldsymbol{k}}| + 2t_\perp\right|} \right) \right)^{-1}, \tag{5.25}$$

where we have used the doped energies in Equation (5.12) and the relation $t_\perp = \mu$ for the semi-metallic phase.

In the case $t_\perp = 0$, Equation (5.25) for the bilayer is, as it should be, identical to Equation (3.21) for the monolayer case, and so is the resulting critical U, which is plotted in Figure 3.1.

On the other hand, in the limit of large-$t_\perp$, we have

$$U_c \approx \left(\int_\diamond \frac{dxdy}{8\pi^2} \frac{1}{|\gamma_{t'}^{\boldsymbol{k}}|} \right)^{-1} - \left(\int_\diamond \frac{dxdy}{8\pi^2} \frac{1}{|\gamma_{t'}^{\boldsymbol{k}}|} \right)^{-2} \frac{1}{8t_\perp} \tag{5.26}$$

up to leading order in $(t_\perp)^{-1}$. In the case of the symmetric honeycomb lattice with $t' = t$, the above equation amounts to

$$\frac{U_c}{t} \approx 4.46 - 2.49\frac{t}{t_\perp}. \tag{5.27}$$

In Figure 5.5, we have plotted the data calculated using Equation (5.25) for the case of $t' = t$, as well as the relation (5.27). As one may notice, the two plots have excellent agreement between each other in the large-$t_\perp/t$ limit. The critical U calculated using Equation (5.25) begins with the value $1.46t$ at $t_\perp = 1.5t + 0^+$, goes as $2.49t/t_\perp$ for large $t_\perp$, and asymptotically approaches the value $4.46t$, which is twice the monolayer critical value.

The reason for this doubling of critical U in the $t_\perp \to \infty$ limit can be understood by examining Equation (5.26). The four terms in the integrand on the right-hand-side of Equation (5.26) correspond to contributions of different spin species and energy bands. Consider, e.g., the spin-$\uparrow$ particles with doped energies $E_j^{\boldsymbol{k}} - \mu$ as discussed before Equation (5.6). Note that due to the Heaviside function in Equation (5.19), only bands with negative doped energies contribute. Furthermore, in the semi-metallic phase we have $\mu = t_\perp$. With these information in mind, and considering the dispersions in Equation (5.3), the two contributions from the spin-$\uparrow$ particles are attributed as

$$\begin{aligned}
\frac{1}{|\gamma_{t'}^{\boldsymbol{k}}|} \quad &: \quad \text{contribution from the band } -|\gamma_{t'}^{\boldsymbol{k}}| + t_\perp \\
&\qquad\quad \text{with doped energy } -|\gamma_{t'}^{\boldsymbol{k}}| + t_\perp - \mu, \\
\frac{1}{\big||\gamma_{t'}^{\boldsymbol{k}}| + 2t_\perp\big|} \quad &: \quad \text{contribution from the band } -|\gamma_{t'}^{\boldsymbol{k}}| - t_\perp \\
&\qquad\quad \text{with doped energy } -|\gamma_{t'}^{\boldsymbol{k}}| - t_\perp - \mu,
\end{aligned} \tag{5.28}$$

The difference between the two bands is clearly $2t_\perp$. As $t_\perp$ increases, the band $-|\gamma_{t'}^{\boldsymbol{k}}| - t_\perp$ moves farther away from the Fermi level, which is at the Dirac points of the band $-|\gamma_{t'}^{\boldsymbol{k}}| + t_\perp$. In the limit $t_\perp \to \infty$, the band $-|\gamma_{t'}^{\boldsymbol{k}}| - t_\perp$ is too far below the Fermi level to be influenced by the interaction. Similar consideration

for the particle-hole-transformed spin-↓ particles leads to the same conclusion for the band $-|\gamma_{t'}^{\boldsymbol{k}}| + t_\perp$. Comparing the $t_\perp \to \infty$ limit to the case of $t_\perp = 0$, the number of bands subjected to the interaction effects is halved in the former case, hence the critical interaction strength is doubled in order to trigger the same phase transition.

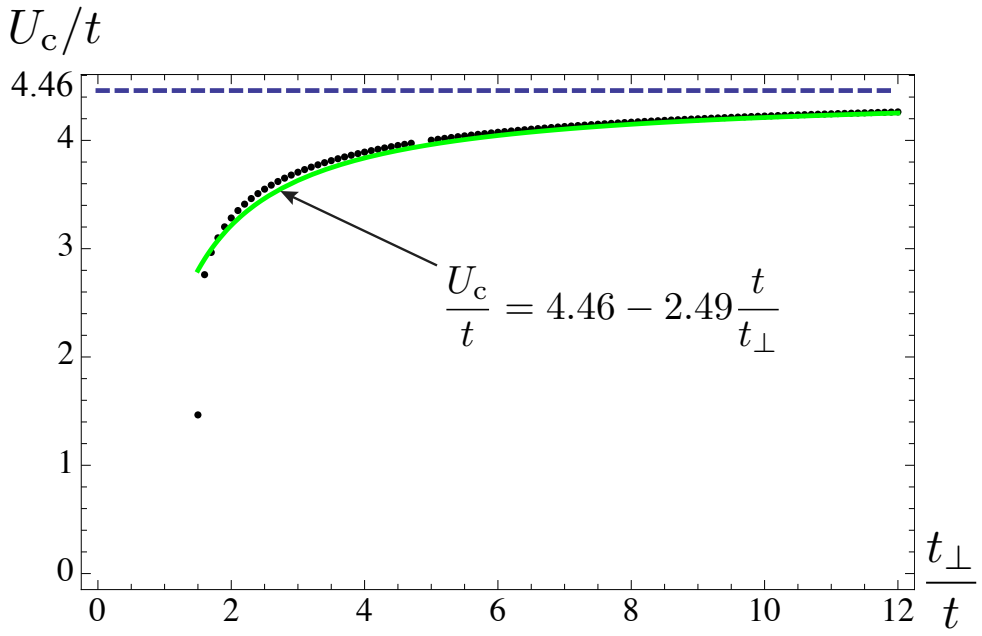

Figure 5.5: The black dots are calculated using Equation (5.25) for $t' = t$, while the solid green line is the relation (5.27). Both of the above are plotted starting from $t_\perp/t = 1.5$ on the horizontal axis, for reasons stated in Section 5.1.1.1. The horizontal dashed line is the asymptotic value 4.46. All quantities are measured in units of t.

5.2.1.1 The symmetric and antisymmetric dimer wave functions

As an attempt to understand the doubling of the critical U in the large-$t_\perp$, we consider the symmetric and antisymmetric wave functions on a dimer containing the two inter-layer nearest-neighboring sites, namely

$$D_{i\sigma\pm}^{\alpha} = \frac{\alpha_{i\sigma}^1 \pm \alpha_{i\sigma}^2}{\sqrt{2}}, \tag{5.29}$$

where $\alpha = a, b$ represent the sub-lattice indices as well as the corresponding fermionic operators, and the superscripts 1 and 2 of α are the layer indices. It can be checked that these operators obey the usual fermionic anti-commutation relations.

In terms of these dimer operators, we have

$$\begin{aligned} & a^{1\dagger}_{i\sigma} b^{1}_{j\sigma} + a^{2\dagger}_{i\sigma} b^{2}_{j\sigma} + b^{1\dagger}_{j\sigma} a^{1}_{i\sigma} + b^{2\dagger}_{j\sigma} a^{2}_{i\sigma} \\ = \; & D^{A\dagger}_{i\sigma+} D^{B}_{j\sigma+} + D^{A\dagger}_{i\sigma-} D^{B}_{j\sigma-} + D^{B\dagger}_{j\sigma+} D^{A}_{i\sigma+} + D^{B\dagger}_{j\sigma-} D^{A}_{i\sigma-} \end{aligned} \tag{5.30}$$

and

$$\alpha^{1\dagger}_{i\sigma} \alpha^{2}_{i\sigma} + \alpha^{2\dagger}_{i\sigma} \alpha^{1}_{i\sigma} = D^{\alpha\dagger}_{i\sigma+} D^{\alpha}_{i\sigma+} - D^{\alpha\dagger}_{i\sigma-} D^{\alpha}_{i\sigma-}. \tag{5.31}$$

Thus, in terms of the dimer operators $D_{\pm}$, the kinetic Hamiltonian (5.1) can be rewritten as

$$\mathcal{H}_0 \;=\; -\sum_{\langle ij\rangle\sigma\varepsilon} t_{ij} D^{A\dagger}_{i\sigma\varepsilon} D^{B}_{j\sigma\varepsilon} + \text{H.c.} - t_{\perp} \sum_{(ij)\sigma\alpha} \left(D^{\alpha\dagger}_{i\sigma+} D^{\alpha}_{i\sigma+} - D^{\alpha\dagger}_{i\sigma-} D^{\alpha}_{i\sigma-} \right) \tag{5.32}$$

where ε is the $\pm$ indices for the symmetric and antisymmetric combinations. Notice that $t_{\perp}$ and $-t_{\perp}$ act as the effective chemical potential for the D_{+} and D_{-} quasi-particles, respectively. The two sets of energy bands derived for the original particles as shown in Equation (5.3), namely

$$E^{\boldsymbol{k}}_{lj} = \pm|\gamma^{\boldsymbol{k}}_{t'}| - t_{\perp} \text{ and } E^{\boldsymbol{k}}_{uj} = \pm|\gamma^{\boldsymbol{k}}_{t'}| + t_{\perp}, \tag{5.33}$$

can then be interpreted as being occupied by the D_{+} and D_{-} particles, respectively. Notice that we have added the subscripts l and u to denote the lower and the upper energy bands. When the system is doped to the Dirac points of the $E^{\boldsymbol{k}}_{uj}$ bands, the $E^{\boldsymbol{k}}_{lj}$ bands are below the Fermi surface for sufficiently large values

of $t_\perp$, and so are completely filled. The difference between the Fermi surface and the middle of the $E^{\boldsymbol{k}}_{lj}$ bands is $2t_\perp$. As $t_\perp$ becomes very large, the $E^{\boldsymbol{k}}_{lj}$ bands are not only fully filled, but also far below the Fermi surface, and thus yield a vanishing contribution to the physical properties in the vicinity of the Fermi level. Consequently the $D_{i\sigma+}$ particles can be neglected in the discussion of large-$t_\perp$ limit, for $U \ll t_\perp$.

In terms of these D_+ and D_- operators, the number operators are given by

$$\begin{aligned} n^{\alpha 1}_{i\sigma} &= \frac{1}{2}\left(D^{\alpha\dagger}_{i\sigma+}D^{\alpha}_{i\sigma+} + D^{\alpha\dagger}_{i\sigma-}D^{\alpha}_{i\sigma-} + D^{\alpha\dagger}_{i\sigma+}D^{\alpha}_{i\sigma-} + D^{\alpha\dagger}_{i\sigma-}D^{\alpha}_{i\sigma+}\right), \\ n^{\alpha 2}_{i\sigma} &= \frac{1}{2}\left(D^{\alpha\dagger}_{i\sigma+}D^{\alpha}_{i\sigma+} + D^{\alpha\dagger}_{i\sigma-}D^{\alpha}_{i\sigma-} - D^{\alpha\dagger}_{i\sigma+}D^{\alpha}_{i\sigma-} - D^{\alpha\dagger}_{i\sigma-}D^{\alpha}_{i\sigma+}\right), \end{aligned} \tag{5.34}$$

with the help of which we can rewrite the onsite interaction term (5.7) as

$$\mathcal{V} = -\frac{U}{2}\sum_{i\alpha}\Big[\left(D^{\alpha\dagger}_{i\uparrow+}D^{\alpha}_{i\uparrow+} + D^{\alpha\dagger}_{i\uparrow-}D^{\alpha}_{i\uparrow-} - 1\right)\left(D^{\alpha\dagger}_{i\downarrow+}D^{\alpha}_{i\downarrow+} + D^{\alpha\dagger}_{i\downarrow-}D^{\alpha}_{i\downarrow-} - 1\right) \tag{5.35}$$

$$+\left(D^{\alpha\dagger}_{i\uparrow+}D^{\alpha}_{i\uparrow-} + D^{\alpha\dagger}_{i\uparrow-}D^{\alpha}_{i\uparrow+}\right)\left(D^{\alpha\dagger}_{i\downarrow+}D^{\alpha}_{i\downarrow-} + D^{\alpha\dagger}_{i\downarrow-}D^{\alpha}_{i\downarrow+}\right)\Big]. \tag{5.36}$$

The terms in (5.35) represent the onsite interaction between the D_+ and D_- quasiparticles, while those in (5.36) represent the flipping between the symmetric and antisymmetric wave functions. Similarly, the chemical potential term (5.5) can be rewritten as

$$-\mu\sum_{i\alpha\sigma\varepsilon} D^{\alpha\dagger}_{i\sigma\varepsilon}D^{\alpha}_{i\sigma\varepsilon}. \tag{5.37}$$

Neglecting the $D_{i\sigma+}$ particles for the reasons described before, one can define the pseudo-spin $\tilde{\sigma}$ such that

$$\tilde{\uparrow} \leftrightarrow \{\uparrow -\}, \tilde{\downarrow} \leftrightarrow \{\downarrow -\}. \tag{5.38}$$

In terms of this pseudo-spin notation, the Hamiltonian, after neglecting the $D_{i\sigma+}$

particles, becomes

$$\begin{aligned}\mathcal{H}_- &= -\sum_{\langle ij\rangle\tilde{\sigma}} t_{ij} D^{A\dagger}_{i\tilde{\sigma}} D^{B}_{j\tilde{\sigma}} + \text{H.c.} - (\mu - t_\perp) \sum_{(ij)\alpha\tilde{\sigma}} D^{\alpha\dagger}_{i\tilde{\sigma}} D^{\alpha}_{i\tilde{\sigma}} \\ &\quad -\frac{U}{2} \sum_{i\alpha} \left(D^{\alpha\dagger}_{i\tilde{\uparrow}} D^{\alpha}_{i\tilde{\uparrow}} - \frac{1}{2} \right) \left(D^{\alpha\dagger}_{i\tilde{\downarrow}} D^{\alpha}_{i\tilde{\downarrow}} - \frac{1}{2} \right), \end{aligned} \tag{5.39}$$

where the constants in the interaction term have been adjusted so that the half-filling of the particles corresponds $t_\perp = \mu$. Hamiltonian (5.39) is nothing other than the attractive Hubbard model for the honeycomb lattice, with an effective chemical potential $(\mu - t_\perp)$ for both A- and B-sublattice sites, and an effective interaction $-U/2$. For $t_\perp = \mu$, this effective model describes half-filling, which is equivalent to its repulsive counter part at the same filling. The latter case has been extensively discussed in the previous chapters.

Since the interaction strength in (5.39) is $\frac{U}{2}$ instead of the original U, the interaction is half as effective in this case. Consequently the critical U needs to be doubled as compared to the limit of $t_\perp \to 0$, in which limit all particles contributes to the physical properties. An equivalent way to look at this phenomenon, but which is not presented here, is to study the density of states, which is effectively halved in the limit $t_\perp \to \infty$. One thus obtains a result consistent with the qualitative argument given below Equation (5.27).

5.2.2 The case of $t' < 2t$

The system is in the semi-metallic phase when the Fermi level is at the Dirac points, which exist for $t' < 2t$ and $t_\perp = \mu = 0$ or $t_\perp = \mu > \frac{t'+2t}{2}$, as illustrated in Figure 5.4(a). As discussed in a previous section, in the semi-metallic phase a finite U_c can be calculated using Equation (5.19).

In Figure 5.7, we included a series of plots for the case $t' = t$, $t_\perp = 4t$. The part of the corresponding band structure with $\mu > 0$ is plotted in the lower panel, from which we can see that the Dirac points are at $\mu = 4t$. Correspondingly, in the upper panel for U_c against μ, an isolated value of $U_\text{c} = 3.92t$ exists at $\mu = 4t$, which is surrounded by the metallic phase in which one has $U_\text{c} = 0$. Because

$U_c < 4t$ at these Dirac points, the order parameter is nonzero in the middle panel, where U was taken to be $4t$.

For $0 < \mu < t$ and $\mu > 7t$, as can be seen in the lower panel of the band structure, the system is in the band-insulating state, for which a nonzero value of U is required to overcome the band gap and thus to form pairs. The value calculated from Equation (5.19) is shown in the upper panel of Figure 5.7. The horizontal dashed line in the upper panel marks the line $U = 4t$, which is the value of U used in the calculation of of the pairing order parameter Δ in the middle panel. Finite Δ exists when $U_c < 4t$, which is the case for the small range of μ right before $\mu = t$ and right after $\mu = 7t$, as indicated in the middle panel.

For $t < \mu < 4t$ and $4t < \mu < 7t$, the system is in the metallic state, i.e. a Fermi surface of finite size exists. According to the discussion before, the critical U is zero. In the language of the middle panel, finite Δ exists for any value of U in this phase. In the middle panel, notice the change in the magnitude of the order parameter, which increases with μ for $\mu > t$, reaches a local maximum at $\mu = 3t$, and reaches a local minimum at $\mu = 4t$. The reverse sequence of changes are observed starting from the minimum at $\mu = 4t$: it increases to a local maximum at $\mu = 5t$, and then decreases to 0 at $\mu = 7t$. Furthermore, at the points $\mu = 3t$ and $\mu = 5t$, the Fermi levels are at the so-called van Hove singularity, at which the density of states has a logarithmic divergence. The same trend is observed in the size of the Fermi surface, as shown in Figure 5.6 for $t < \mu < 4t$ as an example. This correlation can be explained by the fact that an increase in the size of the Fermi surface, as well as the attainment of the van Hove singularities, are accompanied by an increase in density of states, which elevates the effectiveness of the interaction, which is then ultimately reflected in the increase in the magnitude of the order parameter.

5.2.3 The case of $t' > 2t$

In the case where $t' > 2t$, the Dirac points no longer exist. The metallic and band-insulating phases span the interaction-free phase space, as shown in Figure 5.4(b).

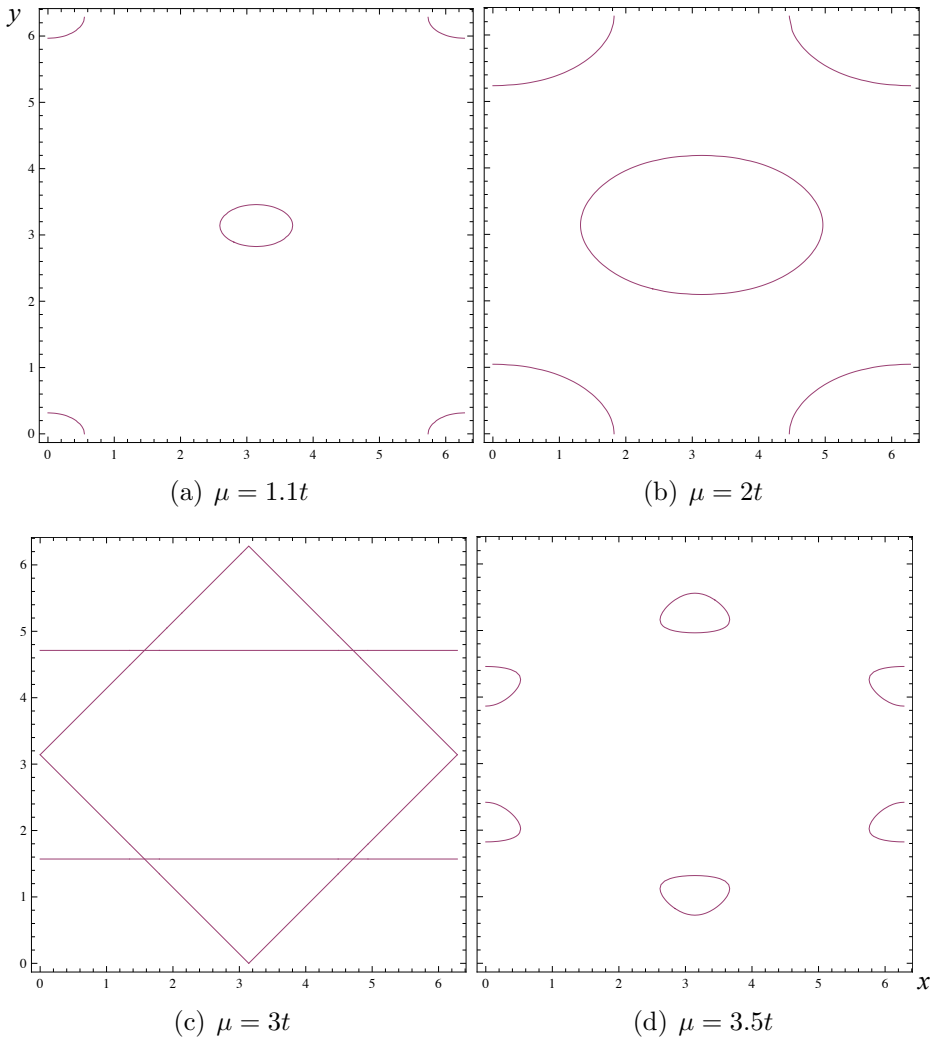

(a) $\mu = 1.1t$ (b) $\mu = 2t$

(c) $\mu = 3t$ (d) $\mu = 3.5t$

Figure 5.6: The Fermi surfaces for $t' = 1, t_\perp = 4t$ and $\mu = 1.1t$ in (a), $2t$ in (b), $3t$ in (c), and $3.5t$ in (d), respectively. The coordinates are such that $x = \frac{\sqrt{3}ak_x}{2}$ and $y = \frac{ak_y}{2}$. The size of the Fermi surface increases from $\mu = 1.1t$, attains its local maximum at $\mu = 3t$, and decreases to zero at $\mu = 4t$. The same trend of change is observed in the magnitude of the order parameter. Furthermore, at $\mu = 3t$ corresponding to the so called van Hove singularity, the density of states has a logarithmic divergence such that the interactions are the most efficient there. At the same point, the size of the Fermi surface as well as the magnitude of the order parameter attain their maximum values.

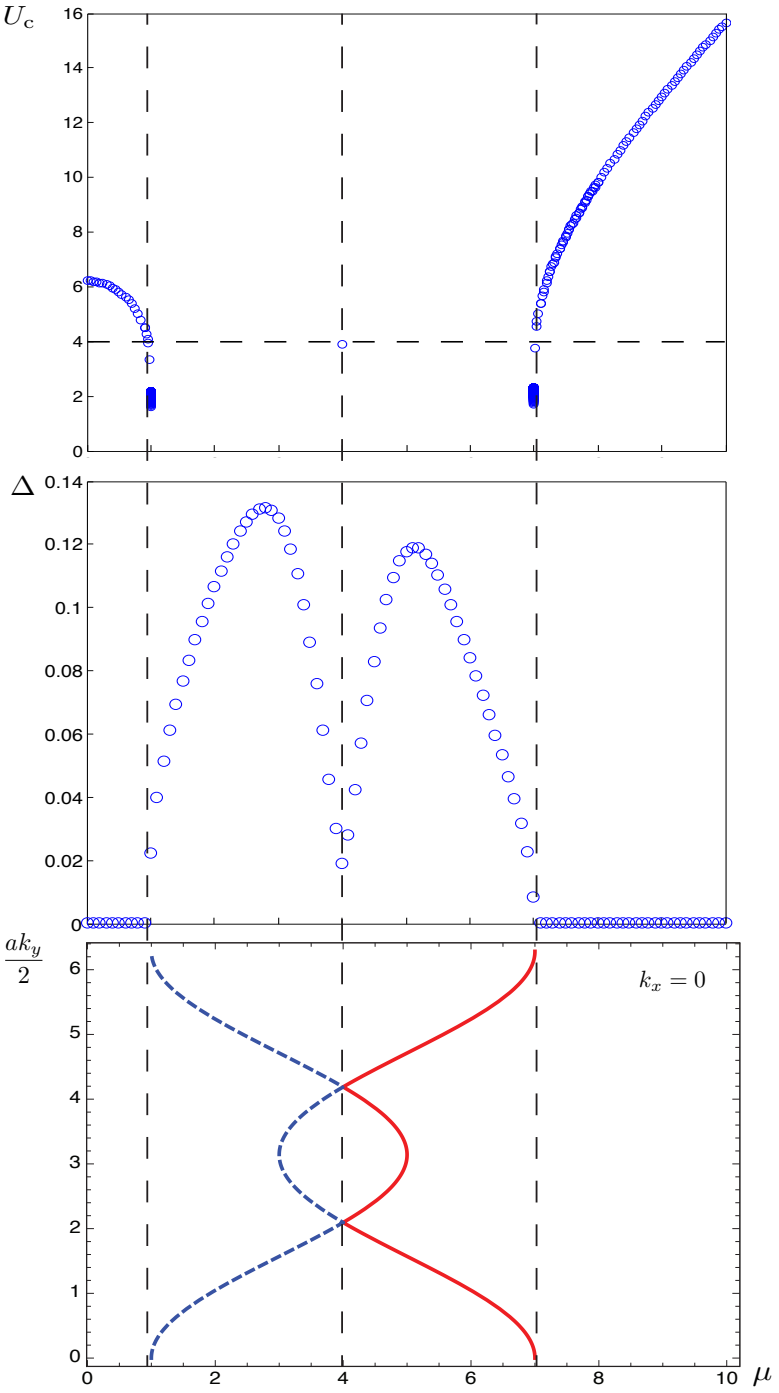

Figure 5.7: Upper panel: the critical U as a function of the chemical potential. Middle panel: the order parameter as a function of the chemical potential for $U = 4t$. Lower panel: the band structure in the rescaled coordinates $\frac{k_y a}{2}$ for $k_x = 0$. All energies are measured in units of t. In all three plots we have $t' = t, t_\perp = 4t$, which corresponds to the horizontal dashed line in Figure 5.4(a). The horizontal dashed line in the upper panel marks the interaction strength $U = 4t$, which is the value used in our previous calculation of Δ in the middle panel. Only the part of the band structure with $\mu > 0$ is plotted in the lower panel. The part with $\mu < 0$ is the mirror image of the lower plot with respect to the y-axis.

In Figure 5.8, we included a series of plots for the case $t' = 3t$ and $t_\perp = 2.5t$, corresponding to the horizontal dashed line in Figure 5.4(b).

For $2.5t < \mu < 3.5t$ and $\mu > 7.5t$, the band structure in the lower panel shows that the system is in the band-insulating phase, for which, due to the band gap, a finite U_c is needed, which can be calculated from Equation (5.19). The results are shown in the upper panel. The horizontal dashed line in the upper panel at $4t$ marks the value of U used in the calculation of Δ in the middle panel. As can be seen from a simple comparison between the upper and the middle panel, the range of μ with finite Δ coincides with that with U_c less than $4t$, as it should be.

For $0 < \mu < 2.5t$ and $3.5t < \mu < 7.5t$, as can be seen in the lower panel in Figure 5.8, the system is in the metallic phase. The finite-size Fermi surface dictates the critical U to be zero, which is shown in the upper panel. The order parameter, which is plotted in the middle panel, is nonzero regardless of the value of U in this phase. The line with $\mu = 1.5t$ marks the transition from the overlapping region between two bands (for $\mu < 1.5t$) to the non-overlapping region (for $\mu > 1.5t$). This same line also corresponds to the van Hove singularity, at which the density of states has a logarithmic divergence. Both of these indicate an abrupt change in the density of states at the Fermi level across the point $\mu = 1.5t$. This is reflected in the change in $d\Delta/d\mu$ at this point on the curve in the middle panel. Otherwise, the change in magnitude of the order parameter can again be traced back to the change in the size of the Fermi surface, as explained in the case of $t' < 2t$ in the previous section.

Notice that the above discussion is based on the uncorrelated band structures shown in the lower panels in Figure 5.7 and 5.8, which, as noted in the discussion following Equation (5.3), remains invariant when the sign of t' or $t_\perp$ are changed. Thus our discussion above applies to the situations with negative t' or $t_\perp$ as well.

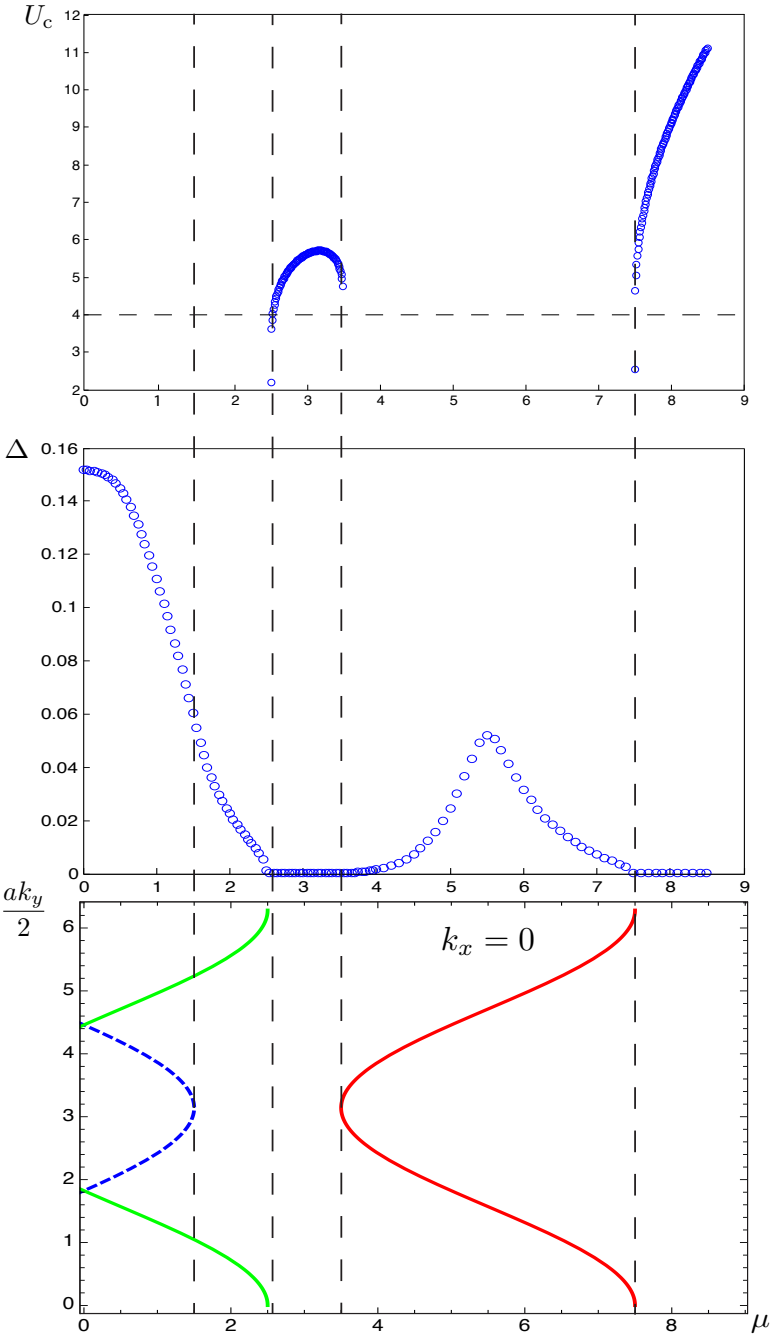

Figure 5.8: Upper panel: the critical U as a function of the chemical potential. Middle panel: the order parameter as a function of the chemical potential for $U = 4t$. Lower panel: the band structure in the rescaled coordinate $\frac{k_y a}{2}$ for $k_x = 0$. All energies are measured in units of t. In all three plots we have $t' = 3t, t_\perp = 2.5t$, which corresponds to the horizontal dashed line in Figure 5.4(b). The horizontal dashed line in the upper plot marks the interaction strength $U = 4t$, which is the value used in our previous calculation of Δ in the middle plot. Only the part of the band structure with $\mu > 0$ is plotted in the lower plot. The part with $\mu < 0$ is the mirror image of the lower plot with respect to the y-axis.

6

Conclusions and Perspectives

6.1 Conclusions

In this thesis, we have presented our results concerning various strongly correlated phases and phase transitions in the honeycomb lattice with in-plane anisotropy. Our studies are based on the Hubbard Model, in which one of the nearest-neighbor hopping amplitudes t' is enhanced with respect to the other two, which remain identical and are denoted as t. The primary interest of us is in the limit of large anisotropy, i.e. $t'/t \to \infty$.

The systems studied in this thesis include the monolayer and the AA-stacked bilayer honeycomb lattice. The main methods used are the mean-field self-consistent and the slave-rotor methods. The results of these methods are then complemented by the Stoner's criterion calculation and the effective Hamiltonian that we derived for the strongly-correlated limit.

Because of the short-range nature of the interaction between ultra-cold atoms [see Chapter 1], the Hubbard Model can be simulated exactly by the system of ultra-cold atoms loaded into a honeycomb optical lattice. This system also offers other major advantages over conventional condensed matter systems in terms of configurability and controllability. In particular, the interaction strength as well as its sign can be engineered via the Feshbach resonance, a feature that is largely missing in graphene and other condensed matter systems. The AA-stacking of bilayer honeycomb lattice can also be easily implemented in an optical lattice system, as discussed in Chapter 5, even more easily than the AB-stacking that is commonly found in natural graphite, due to the subtle mismatch between the two layers in the latter case.

6. CONCLUSIONS AND PERSPECTIVES

We first studied the monolayer honeycomb lattice. The first main result of this thesis is the antiferromagnetic transition line as a function of the anisotropy, which is produced using the mean-field self-consistent method, and then reproduced in the Stoner's criterion calculation. This transition line can be interpreted using simple scaling arguments [see Section 3.1.3].

While there is a consensus in the literature on the antiferromagnetic transition in the honeycomb lattice in the strongly-correlated limit, the existence of the spin-liquid state in this lattice in the region of intermediate interaction strength is subjected to much controversy. The main reason for both the consensus and the later controversy mentioned above is the absence of geometric frustration in the bipartite honeycomb lattice. In this thesis, we study the possible spin-liquid phase transition starting from the (semi-)metallic/band-insulating phase in the anisotropic honeycomb lattice using the slave-rotor treatment. The resulting transition line is partially second order and partially first order as a result of the free energy analysis of the multiple solutions to the problem [see Section 4.3.6]. In the limit of large anisotropy, in which we are primarily interested, we find a gapped spin-liquid phase dominating the phase space. This phase is described by decoupled dimers on the bonds with the stronger hopping amplitude t'.

The transition between the spin-liquid and the antiferromagnetic phases, which presumably is the antiferromagnetic transition line, is not treated within our slave-rotor calculation. However, the effective Hamiltonian that we derived for the strongly-correlated limit [see Section 3.3, and particularly Section 3.3.2.3] shows that this transition mimics that of the two-dimensional quantum Ising model on a square lattice. The disordered phase obtained within the effective Ising model that should presumably be identified with the spin-liquid phase is that which consists of spin-singlets on every dimer (t'-bonds), which closely resembles the gapped spin-liquid phase obtained in the slave-rotor treatment, the latter of which is described by decoupled t'-bonds. The spin-spin-correlation in both phases are expected to decay exponentially. Furthermore, the excitation gaps in the two phases in the vicinity of the antiferromagnetic transition line are t' (band gap in the spinon channel of the gapped slave-rotor spin-liquid) and $2t'$ (singlet-triplet energy gap in the Ising model), both of which depend on t' alone and not on other energy scales, hinting at the same origin of the two gaps. Thus,

although the fate of this spin-liquid phase in the isotropic limit ($t' = t$) as well as the other limit of anisotropy ($t' < t$) cannot be settled within our slave-rotor calculation, we are fairly convinced of the existence of the spin-liquid phase in the limit $t'/t \to \infty$. On the other hand, the effective Hamiltonian suggests that the spin-liquid phase is destabilized by the inter-dimer superexchange interaction terms in favor of the Néel ordered states. This offers a possible mechanism by which the spin-liquid phase in the large-t' limit can be destroyed in the isotropic limit ($t' = t$) as well as the limit $t/t' \to \infty$ of weakly coupled chains. The absence of the spin-liquid phase in the honeycomb lattice has been reported for the isotropic limit in a recent large-scale quantum Monte Carlo simulation [68]. Note that our discussion in this thesis is focused on the limit of zero temperature. For nonzero temperature, the Mermin-Wagner theorem states that, in two spatial dimensions, the the spin-rotational symmetry cannot be spontaneous broken in the Hubbard model with onsite interaction. Thus for finite temperatures, there can be no antiferromagnetic order in the Mott state, and thus the spin-liquid phase dominates the strongly-correlated limit regardless of the value of t'.

In the study of the pairing transition in the AA-stacked bilayer honeycomb lattice, the mean-field self-consistent method is again used. For the system doped to the Dirac points in the limit of large inter-layer hopping, the interaction is found to be half as effective as compared to the monolayer case, due to the effective reduction of number of bands, or, equivalent, of the density of states. In a detailed study of the two typical cases of the $t' < 2t$ and $t' > 2t$, the correlation between the size of the Fermi surface and the magnitude of the order parameter, and that between the vanishing of the Fermi surface and the existence of a finite critical interaction strength are found.

6.2 Perspectives

As discussed in Chapter 1, and quantitatively analyzed in Chapter 2, the lattice parameters can be easily adjusted in an optical lattice. The topological phase transition, as a prominent example, has been realized as reported in Reference [32] within Bloch-oscillation experiments. In addition, there have been various

proposals for the detection of the strongly correlated phases in the optical lattice systems. For example, the localization of particles can be identified in time-of-flight experiments [118], while the antiferromagnetic phase can be measured using optical Bragg scattering [119]. The spin-liquid phase can then be identified in a system which exhibits charge localization in a time-of-flight experiment but no antiferromagnetic ordering in optical Bragg scattering. We are looking forward to the relevant experimental efforts in these directions.

On the theory side, there are many exciting possible directions for future investigations. For example, it is interesting to study the effects of a fluctuating gauge field on our mean-field results. This can be accomplished using the renormalization group technique. Another research direction would be the analysis of the fate of the spin-liquid phase in the isotropic limit, as discussed following the phase diagram (4.3). This can be partially accomplished by using quantum Monte Carlo method to simulate the system of moving dimers on the honeycomb lattice. In the case of AA-stacked bilayer honeycomb lattice, the investigation of the possible spin-liquid state in the repulsive model is clearly another interesting subject.

Bibliography

[1] K. S. Novoselov, A. K. Geim, S. V. Morozov, D. Jiang, Y. Zhang, S. V. Dubonos, I. V. Grigorieva, and A. A. Firsov, *Electric Field Effect in Atomically Thin Carbon Films*, Science **306**, 666-669 (2004). 1

[2] K. S. Novoselov, A. K. Geim, S. V. Morozov, D. Jiang, M. I. Katsnelson, I. V. Grigorieva, S. V. Dubonos, and A. A. Firsov, *Two-dimensional gas of massless Dirac fermions in graphene*, Nature **438**, 197-200 (2005). 1, 2

[3] Claire Berger, Zhimin Song, Tianbo Li, Xuebin Li, Asmerom Y. Ogbazghi, Rui Feng, Zhenting Dai, Alexei N. Marchenkov, Edward H. Conrad, Phillip N. First, and Walt A. de Heer, *Ultrathin Epitaxial Graphite: 2D Electron Gas Properties and a Route toward Graphene-based Nanoelectronics*, J. Phys. Chem. B **108**, 199102-19916 (2004). 1

[4] S. Y. Zhou, G.-H. Gweon, J. Graf, A. V. Fedorov, C. D. Spataru, R. D. Diehl, Y. Kopelevich, D.-H. Lee, Steven G. Louie and A. Lanzara, *First direct observation of Dirac fermions in graphite*, Nat. Phys **2**, 595-599 (2006). 1, 3

[5] "The Nobel Prize in Physics 2010". Nobelprize.org. 22 Oct 2011. 1

[6] Boardman, John. *The Neolithic-Eneolithic Period*. The Cambridge ancient history, Volume **3**, 31-32. 1

[7] K.I. Bolotin, K.J. Sikes, Z. Jiang, M. Klima, G. Fudenberg, J. Hone, P. Kima, H.L. Stormer, *Ultrahigh electron mobility in suspended graphene*, Solid State Commun. **146**, 351-355 (2008). 2

[8] Xu Du, Ivan Skachko, Anthony Barker, Eva Y. Andrei, *Suspended graphene: a bridge to the Dirac point*, Nat. Nanotechnol. **3**, 491-495 (2008). 2

[9] C.R. Dean, A.F. Young, I. Meric, C. Lee, L. Wang, S. Sorgenfrei, K. Watanabe, T. Taniguchi, P. Kim, K.L. Shepard and J. Hone, *Boron nitride substrates for high-quality graphene electronics*, Nat. Nanotechnol. **5**, 722-726 (2010). 2

[10] Yu-Ming Lin, Keith A. Jenkins, Alberto Valdes-Garcia, Joshua P. Small, Damon B. Farmer, and Phaedon Avouris, *Operation of Graphene Transistors at Gigahertz Frequencies*, Nano Lett. **9**, 422-426 (2009). 2

[11] Brian Standley, Wenzhong Bao, Hang Zhang, Jehoshua Bruck, Chun Ning Lau, and Marc Bockrath, *Graphene-Based Atomic-Scale Switches*, Nano Lett. **8**, 3345-3349 (2008). 2

[12] J. Scott Bunch, Scott S. Verbridge, Jonathan S. Alden, Arend M. van der Zande, Jeevak M. Parpia, Harold G. Craighead, and Paul L. McEuen, *Impermeable Atomic Membranes from Graphene Sheets*, Nano Lett. **8**, 2458-2462 (2008). 2

[13] D.S.L. Abergela, V. Apalkovb, J. Berashevicha, K. Zieglerc and Tapash Chakrabortya, *Properties of graphene: a theoretical perspective*, Adv. Phys. **59**, 261-482 (2010). 2, 5, 111

[14] Y. Zhang, Y.-W. Tan, H. L. Stormer, and P. Kim, *Experimental observation of the quantum Hall effect and Berry's phase in graphene*, Nature **438**, 201-204 (2005). 2

[15] P.R. Wallace, *The Band Theory of Graphite*, Phys. Rev. **71**, 622-634 (1947). 2, 27

[16] M.I. Katsnelson, K.S. Novoselov, *Graphene: New bridge between condensed matter physics and quantum electrodynamics*, Solid State Commun. **143**, 3-13 (2007). 3

[17] M.I. Katsnelson, K.S. Novoselov and A.K. GEIM, *Chiral tunnelling and the Klein paradox in graphene*, Nat. Phys. **2**, 620-625 (2006). 3

[18] K.S. Novoselov, A.K. Geim, S.V. Morozov, D. Jiang, M.I. Katsnelson, I.V. Grigorieva, S.V. Dubonos and A.A. Firsov, *Two-dimensional gas of massless Dirac fermions in graphene*, Nature **438**, 197-200 (2005). 3

[19] Guohong Li and Eva Y. Andrei, *Observation of Landau levels of Dirac fermions in graphite*, Nat. Phys. **3**, 623-627 (2007). 3

[20] Mark O. Goerbig, *Electronic properties of graphene in a strong magnetic field*, Rev. Mod. Phys. **83**, 1193-1243 (2011). 3, 17

[21] Mark O. Goerbig, J.-N. Fuchs, G. Montambaux, and F. Piéchon, *Tilted anisotropic Dirac cones in quinoid-type graphene and α-(BEDT-TTF)$_2I_3$*, Phys. Rev. B **78**, 045415 (2008). 5

[22] S. Sorella and E. Tosatti, *Semi-Metal-Insulator Transition of the Hubbard Model in the Honeycomb Lattice*, Europhys. Lett. **19**, 699-704 (1992). 5, 21, 23, 51, 125

[23] Vitor M. Pereira, A. H. Castro Neto and N. M. R. Peres, *Tight-binding approach to uniaxial strain in graphene*, Phys. Rev. B **80**, 045401 (2009). 5

[24] G. Montambaux, F. Piéchon, J.-N. Fuchs, and Mark O. Goerbig, *Merging of Dirac points in a two-dimensional crystal*, Phys. Rev. B **80**, 153412 (2009). 5, 16

[25] K. L. Lee, B. Grémaud, R. Han, B.-G. Englert, and Ch. Miniatura, *Ultracold fermions in a graphene-type optical lattice*, Phys. Rev. A **80**, 043411 (2009). 5, 15, 32

[26] B. Wunsch, F. Guinea and F. Sols, *Dirac-point engineering and topological phase transitions in honeycomb optical lattices*, New J. Phys. **10**, 103027 (2008). 5, 15

[27] F. Liu, P. Ming, and Ju Li, *Ab initio calculation of ideal strength and phonon instability of graphene under tension*, Phys. Rev. B **76**, 064120 (2007). 5

[28] Immanuel Bloch, Jean Dalibard and Wilhelm Zwerger, *Many-body physics with ultracold gases*, Rev. Mod. Phys. **80**, 885-964 (2008). 5

[29] James R. Anglin and Wolfgang Ketterle, *Bose-Einstein condensation of atomic gases*, Nature **416**, 211-218 (2002). 5, 6

[30] Immanuel Bloch, *Ultracold quantum gases in optical lattices*, Nat. Phys. **1**, 23-30 (2005). 5, 6

[31] G. Grynberg and C. Robilliard, *Cold atoms in dissipative optical lattices*, Phys. Rep. **355**, 335-451 (2001). x, 5, 7, 8, 28, 29

[32] Leticia Tarruell, Daniel Greif, Thomas Uehlinger, Gregor Jotzu and Tilman Esslinger, *Creating, moving and merging Dirac points with a Fermi gas in a tunable honeycomb lattice*, Nature **483**, 302-305 (2012). 5, 6, 7, 16, 114, 139

[33] L.-M. Duan, E. Demler, and M. D. Lukin, *Controlling Spin Exchange Interactions of Ultracold Atoms in Optical Lattices*, Phys. Rev. Lett. **91**, 090402-1 (2003). 5, 6

[34] Zhu S., Wang B., Duan L., *Simulation and Detection of Dirac Fermions with Cold Atoms in an Optical Lattice*, Phys. Rev. Lett. **98**, 260402 (2007). 5, 15

[35] A.H. Castro Neto, F. Guinea, N.M.R. Peres and K.S. Novoselov and A.K. Geim, *The electronic properties of graphene*, Rev. Mod. Phys. **81**, 109-162 (2009). 5, 20, 25, 111, 112

[36] Carl E. Wieman, David E. Pritchard, David J. Wineland, *Atom cooling, trapping, and quantum manipulation*, Rev. Mod. Phys. **71**, S253-S262 (1999). 6

[37] W. Ketterle and M.W. Zwierlein, *Making, probing and understanding ultracold Fermi gases*, Riv Nuovo Cimento **31**, 247-422 (2008). 6

[38] M.H. Anderson, J.R. Ensher, M.R. Matthews, C.E. Wieman, E.A. Cornell, *Observation of Bose-Einstein Condensation in a Dilute Atomic Vapor*, Science **269**, 198-201 (1995). 6

[39] C.C. Bradley, C.A. Sackett, J.J. Tollett, and R.G. Hulet, *Evidence of Bose-Einstein Condensation in an Atomic Gas with Attractive Interactions*, Phys. Rev. Lett. **75**, 1687-1690 (1995). 6

[40] K.B. Davis, M.O. Mewes, M.R. Andrews, N.J. van Druten, D.S. Durfee, D.M. Kurn, and W. Ketterle, *Bose-Einstein Condensation in a Gas of Sodium Atoms*, Phys. Rev. Lett. **75**, 3969-3973 (1995). 6

[41] B. De Marco, J.L. Bohn, J.P. Burke, M. Holland, and D.S. Jin, *Measurement of p-Wave Threshold Law Using Evaporatively Cooled Fermionic Atoms*, Phys. Rev. Lett. **82**, 4208-4211 (1999). 6

[42] F. Schreck, L. Khaykovich, K.L. Corwin, G. Ferrari, T. Bourdel, J. Cubizolles, and C. Salomon, *Quasipure Bose-Einstein Condensate Immersed in a Fermi Sea*, Phys. Rev. Lett. **87**, 080403 (2001). 6

[43] A.G. Truscott, K.E. Strecker, W.I. McAlexander, G.B. Partridge, and R.G. Huletdagger, *Observation of Fermi Pressure in a Gas of Trapped Atoms*, Science **291**, 2570-2572 (2001). 6

[44] D. Jaksch, C. Bruder, J. I. Cirac, C. W. Gardiner, and P. Zoller, *Cold Bosonic Atoms in Optical Lattices*, Phys. Rev. Lett. **81**, 3108 (1998). 6

[45] J. Cubizolles, T. Bourdel, S.J.J.M.F. Kokkelmans, G.V. Shlyapnikov, and C. Salomon, *Production of long-lived ultracold Li_2 molecules from a fermi gas*, Phys. Rev. Lett. **91**, 240401 (2003). 6

[46] M.W. Zwierlein, J.R. Abo-Shaeer, A. Schirotzek, C.H. Schunck, and W. Ketterle, *Vortices and superfluidity in a strongly interacting Fermi gas*, Nature **435**, 1047-1051 (2005). 6

[47] J.K. Chin, D.E. Miller, Y. Liu, C. Stan, W. Setiawan, C. Sanner, K. Xu, and W. Ketterle, *Evidence for superfluidity of ultracold fermions in an optical lattice*, Nature **443**, 961-964 (2006). 6

[48] M.W. Zwierlein, A. Schirotzek, C.H. Schunck, and W. Ketterle, *Fermionic Superfluidity with Imbalanced Spin Populations*, Science **311**, 492- 496 (2006). 6

[49] Guthrie B. Partridge, Wenhui Li, Ramsey I. Kamar, Yean-an Liao, Randall G. Hulet, *Pairing and Phase Separation in a Polarized Fermi Gas*, Science **311**, 503-505 (2006). 6

[50] Y. Shin, M.W. Zwierlein, C.H. Schunck, A. Schirotzek, and W. Ketterle, *Observation of phase separation in a strongly interacting imbalanced Fermi gas*, Phys. Rev. Lett. **97**, 030401 (2006). 6

[51] G.B. Partridge, Wenhui Li, Y.A. Liao, R.G. Hulet, M. Haque and H.T.C. Stoof, *Deformation of a trapped fermi gas with unequal spin populations*, Phys. Rev. Lett. **97**, 190407 (2006). 6

[52] Yong-il Shin, Christian H. Schunck, André Schirotzek and Wolfgang Ketterle, *Phase diagram of a two-component Fermi gas with resonant interactions*, Nature **451**, 689-693 (2007). 6

[53] E. Timmermans, P. Tommasini, M. Hussein, and A. Kerman, *Feshbach resonances in atomic Bose-Einstein condensates*, Phys. Rep. **315**, 199 (1999). 6

[54] C. Cheng, P. Julienne, E. Tiesinga, *Feshbach resonances in ultracold gases*, Rev. Mod. Phys. **82**, 1225-1286 (2010). 6

[55] P. Soltan-Panahi, J. Struck, P. Hauke, A. Bick, W. Plenkers, G. Meineke, C. Becker, P. Windpassinger, M. Lewenstein and K. Sengstock, *Multi-component quantum gases in spin-dependent hexagonal lattices*, Nat. Phys. **7**, 434-440 (2011). 7, 114

[56] D. Jaksch, and P. Zoller, *Creation of effective magnetic fields in optical lattices: the Hofstadter butterfly for cold neutral atoms*, New J. Phys. **5**, 56.1-56.11 (2003). 7

[57] Y.-J. Lin, R. L. Compton, K. Jiménez-García, J.V. Porto and I.B. Spielman, *Synthetic magnetic fields for ultracold neutral atoms*, Nature **462**, 628-632 (2009). 7

[58] Fabrice Gerbier and Jean Dalibard, *Gauge fields for ultracold atoms in optical superlattices*, New J. Phys. **12**, 033007 (2010). 7

[59] Agnieszka Górecka, Benoît Grémaud, and Christian Miniatura, *Synthetic magnetic fluxes on the honeycomb lattice*, arXiv:1105.3535v1 [cond-mat.quant-gas]. 7

[60] Y.-J. Lin, R. L. Compton, K. Jiménez-García, W.D. Phillips, J.V. Porto and I.B. Spielman, *A synthetic electric force acting on neutral atoms*, Nat. Phys. **7**, 531-534 (2011). 7

[61] Jean Dalibard and Fabrice Gerbier, *Colloquium: Artifcial gauge potentials for neutral atoms*, Rev. Mod. Phys. **83**, 1523-1543 (2011). 7

[62] D.C. Elias, R.V. Gorbachev, A.S. Mayorov, S.V. Morozov, A.A. Zhukov, P. Blake, L.A. Ponomarenko, I.V. Grigorieva, K.S. Novoselov, F. Guinea and A.K. Geim, *Dirac cones reshaped by interaction effects in suspended graphene*, Nat. Phys. **7**, 701704 (2011). 20

[63] Andrew L. Walter, Aaron Bostwick, Ki-Joon Jeon, Florian Speck, Markus Ostler, Thomas Seyller, Luca Moreschini, Young Jun Chang, Marco Polini, Reza Asgari, Allan H. MacDonald, Karsten Horn, and Eli Rotenberg, *Effective screening and the plasmaron bands in graphene*, Phys. Rev. B **84**, 085410 (2011). 20

[64] Valeri N. Kotov, Bruno Uchoa, Vitor M. Pereira, F. Guinea, and A.H. Castro Neto, *Electron-Electron Interactions in Graphene: Current Status and Perspectives*, Rev. Mod. Phys. **84**, 10671125 (2012). 20

[65] Xiao-Gang Wen, *Quantum orders and symmetric spin liquids*, Phys. Rev. B **65**, 165113 (2002). 21, 45, 86

[66] L.M. Martelo, M. Dzierzawa, L. Siffert, D. Baeriswyl, *Mott-Hubbard transition and antiferromagnetism on the honeycomb lattice*, Z. Phys. B **103**, 335-338 (1997). 21

[67] Thereza Paiva, R.T. Scalettar, W. Zheng, R.R.R. Singh and J. Oitmaa, *Ground-state and finite-temperature signatures of quantum phase transitions in the half-filled Hubbard model on a honeycomb lattice*, Phys. Rev. B **72**, 085123 (2005). 21

[68] Sandro Sorella, Yuichi Otsuka, and Seiji Yunoki, *Absence of a Spin Liquid Phase in the Hubbard Model on the Honeycomb Lattice*, arXiv:1207.1783v1 [cond-mat.str-el]. 21, 22, 139

[69] Sung-Sik Lee and Patrick A. Lee, *U(1) Gauge Theory of the Hubbard Model: Spin Liquid States and Possible Application to κ-(BEDT-TTF)$_2$Cu$_2$(CN)$_3$*, Phys. Rev. Lett. **95**, 036403 (2005). 21, 22, 86, 89, 106

[70] Michael Hermele, *SU(2) gauge theory of the Hubbard model and application to the honeycomb lattice*, Phys. Rev. B **76**, 035125 (2007). 21, 22

[71] Stephan Rachel and Karyn Le Hur, *Topological insulators and Mott physics from the Hubbard interaction*, Phys. Rev. B **82**, 075106 (2010). 21, 22, 89, 106

[72] S. Florens and A. Georges, *Quantum impurity solvers using a slave rotor representation*, Phys. Rev. B **66**, 165111 (2002), and *Slave-rotor mean-field theories of strongly correlated systems and the Mott transitionin finite dimensions* **70**, 035114 (2004). 22, 86, 150

[73] Z.Y. Meng, T.C. Lang, S. Wessel, F.F. Assaad and A. Muramatsu, *Quantum spin liquid emerging in two-dimensional correlated Dirac fermions*, Nature **464**, 847-851 (2010). 22, 45, 85, 107

[74] P.W. Anderson, *Resonating valence bonds: a new kind of insulator?*, Mat. Res. Bull. **8**, 153-160 (1973). 23, 109

[75] Steven A. Kivelson, Daniel S. Rokhsar and James P. Sethna, *Topology of the resonating valence-bond state: Solitons and high-T_c superconductivity*, Phys. Rev. B **35**, 8865-8868 (1987). 23, 109

[76] R. Moessner and S.L. Sondhi, *Resonating Valence Bond Phase in the Triangular Lattice Quantum Dimer Model*, Phys. Rev. Lett. **86**, 1881-1884 (2001). 23, 109

[77] Gennady V. Mil'nikov and Hiroki Nakamura, *Practical implementation of the instanton theory for the ground-state tunneling splitting* , J. Chem. Phys. **115**, 6881 (2001). 32

[78] Jing-Rong Wang, Guo-Zhu Liu, and Stefan Kirchner, *Nature of the antiferromagnetic quantum phase transition on the honeycomb lattice*, arXiv:1110.0093v1 [cond-mat.str-el]. 41

[79] Masatoshi Imada, Atsushi Fujimori, Yoshinori Tokura, *Metal-insulator transitions*, Rev. Mod. Phys. **70**, 1039-1263 (1998). 41

[80] Shi-Min Cui, *Self-consistent mean-field approximation for the square-lattice frustrated Heisenberg model*, J. Phys.: Condens. Matter **4**, L389-L394 (1992). 41

[81] Daping Chu and Jue-lian Shen, *Self-consistent approximation for spin-$\frac{1}{2}$ quantum Heisenberg antiferromagnets*, Phys. Rev. B **44**, 4689 (1991). 41

[82] Tung-Lam Dao, Antoine Georges, Jean Dalibard, Christophe Salomon, and Iacopo Carusotto, *Measuring the One-Particle Excitations of Ultracold Fermionic Atoms by Stimulated Raman Spectroscopy*, Phys. Rev. Lett. **98**, 240402 (2007). 53

[83] Tung-Lam Dao, Iacopo Carusotto and Antoine Georges, *Probing quasiparticle states in strongly interacting atomic gases by momentum-resolved Raman photoemission spectroscopy*, Phys. Rev. A **80**, 023627 (2009). 53

[84] Liang Chen, C. Bourbonnais, T. Li, and A.-M. S. Tremblay, *Magnetic Properties of the Two-Dimensional Hubbard Model*, Phys. Rev. Lett. **66**, 369-372 (1991). 53

[85] S. Doniach and E.H. Sondheimer, *Green's Functions for Solid State Physicists*. 56

[86] Jozef Spałek, *t-J model then and now: A personal perspective from the pioneering times*, Acta Physica Polonica A **111**, 409-24 (2007). 61

[87] Daijiro Yoshioka, *Mean Field Theory of the Square Lattice Antiferromagnetic Heisenberg Model*, Journal of the Physical Society of Japan **58**, 32-35 (1989). 61

[88] Subir Sachdev, *Quantum Phase Transitions*, 2nd Edition, Cambridge University Press. 83, 109

[89] R.J. Elliott, P. Pfeuty, and C. Wood, *Ising model with a transverse field*, Phys. Rev. Lett. **25**, 443-446 (1970). 83, 109

[90] Yuan-Ming Lu, Ying Ran, *Spin liquids on a honeycomb lattice: Projective Symmetry Group study of Schwinger fermion mean-field theory*, arXiv:1005.4229v1 [cond-mat.str-el]. 86

[91] E. Zhao and A. Paramekanti, *Self-consistent slave rotor mean-field theory for strongly correlated systems*, Phys. Rev. B **76**, 195101 (2007). 88, 106

[92] Ki-Seok Kim and Jung Hoon Han, *Slave-rotor theory of antiferromagnetic Hubbard model*, arXiv:cond-mat/0605266v1 [cond-mat.str-el]. 89

[93] John W. Negele and Henri Orland, *Quantum many-particle systems*. 94

[94] In $G_X(\boldsymbol{k}, i\nu_n)$, a renormalization of $U \to \frac{U}{2}$ has been performed in order to preserve the exact atomic limit. For details see Reference [72]. 96

[95] See, e.g., James F. Annett, *Superconductivity, Superfluids and Condensates*, Oxford University Press (2004). 96, 99

[96] Fa Wang, *Schwinger boson mean field theories of spin liquid states on a honeycomb lattice: Projective symmetry group analysis and critical field theory*, Phys. Rev. B **82**, 024419 (2010). 107

[97] R. Moessner, S. Sondhi, and P. Chandra, *Phase diagram of the hexagonal lattice quantum dimer model*, Phys. Rev. B **64**, 144416 (2001). 107

[98] For a review, see I. Affleck, *Quantum spin chains and the Haldane gap*, J. Phys.:Condens. Matt. **1**, 3047-3072 (1989). 108

[99] E. McCann and V.I. Falko, *Landau-Level Degeneracy and Quantum Hall Effect in a Graphite Bilayer*, Phys. Rev. Lett. **96**, 086805 (2006). 111

[100] T. Ohta, A. Bostwick, T. Seyller, K. Horn, and E. Rotenberg, *Controlling the Electronic Structure of Bilayer Graphene*, Science **313**, 951-954 (2006). 111

[101] K.S. Novoselov, E. McCann, S.V. Morozov, V.I. Falko, M.I. Katsnelson, U. Zeitler, D. Jiang, F. Schedin, and A.K. Geim, *Unconventional quantum Hall effect and Berry's phase of 2π in bilayer graphene*, Nat. Phys. **2**, 177-180 (2006). 111

[102] Edward McCann and Mikito Koshino, *The electronic properties of bilayer graphene*, arXiv:1205.6953v1 [cond-mat.mes-hall]. 111

[103] Edward McCann, David S.L. Abergel, Vladimir I. Fal'ko, *Electrons in bilayer graphene*, Solid State Commun. **143**, 110-115 (2007). 111

[104] M. Titov and C.W.J. Beenakker, *Josephson effect in ballistic graphene*, Phy. Rev. B 74, 041401R (2006); M. Titov, A. Ossipov, and C.W.J. Beenakker, *Excitation gap of a graphene channel with superconducting boundaries*, Phy. Rev. B **75**, 045417 (2007). 112

[105] Gianni Profeta, Matteo Calandra, and Francesco Mauri, *How to make graphene superconducting*, arXiv:1105.3736v1 [cond-mat.supr-con]. 112

[106] Edward McCann and Vladimir I. Falko, *Landau-Level Degeneracy and Quantum Hall Effect in a Graphite Bilayer*, Phys. Rev. Lett. **96**, 086805 (2006). 112

[107] R. de Gail, M.O. Goerbig, F. Guinea, G. Montambaux, and A.H. Castro Neto, *Topologically protected zero modes in twisted bilayer graphene*, Phys. Rev. B **84**, 045436 (2011). 112

[108] P.L. de Andres, R. Ramírez, and J.A. Vergés, *Strong covalent bonding between two graphene layers*, Phys. Rev. B **77**, 045403 (2008). 112

[109] Yen-Hung Ho, Jhao-Ying Wu, Rong-Bin Chen, Yu-Huang Chiu, and Ming-Fa Lin, *Optical transitions between Landau levels: AA-stacked bilayer graphene*, Appl. Phys. Lett. **97**, 101905 (2010). 112

[110] I. Lobato and B. Partoens, *Multiple Dirac particles in AA-stacked graphite and multilayers of graphene*, Phys. Rev. B **83**, 165429 (2011). 112

[111] A.L. Rakhmanov, A.V. Rozhkov, A.O. Sboychakov, and Franco Nori, *Instabilities of the AA-stacked graphene bilayer*, arXiv:1111.5093v1 [cond-mat.mes-hall]. 112, 125

[112] E. Prada, P. San-Jose, L. Brey, H.A. Fertig, *Band topology and the quantum spin Hall effect in bilayer graphene*, Solid State Commun. **151**, 1075-1083 (2011). 112

[113] C.W. Chiu, S.H. Lee, S.C. Chen, F.L. Shyu and M.F. Lin, *Absorption spectra of AA-stacked graphite*, New J. Phys. **12**, 083060 (2010). 112

[114] J. Borysiuk, J. Sołys and J. Piechota, *Stacking sequence dependence of graphene layers on SiC(0001)-Experimental and theoretical investigation*, J. Appl. Phys. **109**, 093523 (2011). 112

[115] Ming-Fa Lin, Ying-Chih Chuang, and Jhao-Ying Wu, *Electrically tunable plasma excitations in AA-stacked multilayer graphene*, Phys. Rev. B **86**, 125434 (2012). 112

[116] J.K. Lee, S.C. Lee, J.P. Ahn, S.C. Kim, J.I.B. Wilson, and P. John, *The growth of AA graphite on (111) diamond*, J. Chem. Phys. **129**, 234709 (2008). 112

[117] Zheng Liu, Kazu Suenaga, Peter J.F. Harris and Sumio Iijima, *Open and Closed Edges of Graphene Layers*, Phys. Rev. Lett. **102**, 015501 (2009). 112

[118] Markus Greiner, Olaf Mandel, Tilman Esslinger, Theodor W. Hänsch and Immuanuel Bloch, *Quantum phase transition from a superfluid to a Mott insulator in a gas of ultracold atoms*, Nature **415**, 39-44 (2002). 140

[119] T.A. Corcovilos, S.K. Baur, J.M. Hitchcock, E.J. Mueller and R.G. Hulet, *Detecting antiferromagnetism of atoms in an optical lattice via optical Bragg scattering*, Phys. Rev. A **81**, 013415 (2010). 140